Chapter 1: Introduction

The use of P-S converted waves associated with multicomponent data acquisition has increased over the last few years, after various studies have demonstrated their tremendous potential as a tool for fracture and lithology characterization (Ata and Michelena, 1995; Miller *et al*., 1995), imaging sediments in gas saturated rocks (Granli *et al*., 1995), imaging shallow sediments with higher resolution than conventional P-P data, and improved imaging of complex structure compared to P-P waves. While multicomponent acquisition and converted wave binning processing have evolved rapidly, corresponding migration techniques are still in their research stage. Recently, considerable attention has been devoted to converted wave DMO (Harrison, 1992; Alfaraj, 1993) and prestack time migration approaches. In the prestack time or depth domain, 2-D and 3-D scalar migration are generally applied to the in-line component. Although this aproach may be sufficient for gently dipping structures, elastic Kirchhoff migration promises to provide a more complete vector friendly solution that accounts for azimuthal anisotropy in the media. Nicoletis *et al*. (1998) proposed a 3D3C true amplitude Kirchhoff imaging formula for P-S waves. Nicoletis *et al*. (2000) continued this effort with a more throrough treatment of 3C polarization of P-S converted waves for the 3D geometry. Additionally, Hou and Marfurt (2001) presented a new multicomponent prestack migration methodology based on successives application of a conventional scalar wave equation migration algorithm.

Fracture characterization is an important part of reservoir development, in particular for carbonate reservoirs. Different techniques have been used to estimate fracture orientation with just P-waves. These include azimuthal P-wave amplitude versus offset (AVO) (Lefeuvre, 1994; Lynn *et al*.; 1996, Perez *et al*., 1999, Neves, 2003), azimuthal variations in P-wave NMO velocity (Sena, 1991; Tsvankin, 1997), and azimuthal variations in P-wave moveout (Li, 1997; Sayers and Ebrom, 1997). Fracture characterisation using converted waves not only estimates fracture orientation but also fracture density (Gaiser *et al*. , 2002). It is this estimation that is the ultimate objective of this thesis.

1.1 Objective

The geologic objective of this research is to identify and image fractures in a carbonate reservoir using 3D3C land seismic data. Several problems need to be addressed before reaching this goal, including: vector fidelity and coupling in acquisition; statics, binning, velocity analysis and seismic migration of converted waves, and correlation of PP-seismic events and PS-seismic events in data interpretation.

Considerable effort has been expanded in seismic processing of the horizontal component to remove the ground roll. A model driven filter is used to enhance the imaging of the deep reflectors without altering their amplitudes, therefore facilitating velocity analysis and improving the stacking results.

As the study area is structurally simple and pre-stack migration has an image quality similar to post-stack time migration, we followed a post-stack migration approach in this study to perform the anisotropy analysis, because of time and disk space. The geophysical objectives of this work are:

- To calibrate this vector migration algorithm as a fracture prediction tool using 3D synthetics, and

- To apply this algorithm to a high quality 3D3C data set from the Barinas Basin, Venezuela.

1.2 Content

In Chapter 2 of this thesis we present basic definitions and basic theoretical aspects required to discuss the characteristics of seismic compressional waves (P-waves and shear waves (S-waves).

In Chapter 3, we give an overview of the geology, starting with a general overview of the geology of Venezuela, and then focusing on the Borburata Field, reviewing fractures, and finally the Escandalosa Formation.

In Chapters 4 and 5 we address seismic processing applied to the vertical and horizontal components respectively. In Chapter 5, we cover in detail the correction for polarization, asymptotic binning, removing the ground roll using a modeling based technique, and statics correction.

In Chapter 6 we generate attribute maps that can bring information about the different fault systems in the area. The basic attributes discussed in this chapter are principal component coherence, semblance coherence and the derivative of the principal component in the X and Y direction.

Finally, in Chapter 7 we show how to choose a subset of azimuths and offsets that will allow us to perform the rotation analysis to measure anisotropic effects. We will also show how to remove the anisotropic overprint in the shallow section in order to map fractures at the reservoir of interest.

Chapter 2: General theory

In this chapter, we review the basic definitions and theoretical aspects required to discuss the characteristics of seismic compressional waves (P-waves), shear waves (S-waves), and converted wave (PS) reflections.

2.1 Converted waves overview

In an elastic medium, when a wave front from a seismic source generating P-waves strikes an interface, the reflected energy is partitioned into P (compressional) and S (shear) waves. Figure 2.1 shows an incoming P-wave P_{inc} traveling at velocity V_1 striking the interface between the upper (yellow) material and the lower (blue) material. Two reflected waves and two transmitted body waves are produced as a result.

From Figure 2.1, it is possible to observe some characteristics of PS-converted wave reflections that make them different and of particular interest compared to PP wave reflections traditionally used in seismic exploration. Due to different *P* and *S* velocities, the ray path geometry of the two types of reflections is different. When dealing with converted waves, the reflection point is known as the *conversion point*, since this is where the P energy is converted into shear energy. This specular reflection point is no longer at the midpoint between the source and receiver (x/2) that we use in binning PP reflections. Furthermore, the specular reflection point for PS reflections is depth dependent even for horizontally layered media, such that, traditional processing techniques must be modified for this new geometry. In converted wave acquisition, the source is usually a conventional seismic energy source, designed to generate downgoing P-waves, either explosive or vibroseis.

2.2 Anisotropy

Anisotropy is related to the variation of a physical property respect to the direction in which it is measured. Anisotropy is related to the directional variation of a property at a point; on the other hand heterogeneity implies property variation from point

to point. Seismic anisotropy is the variation of seismic velocity with respect to a direction.

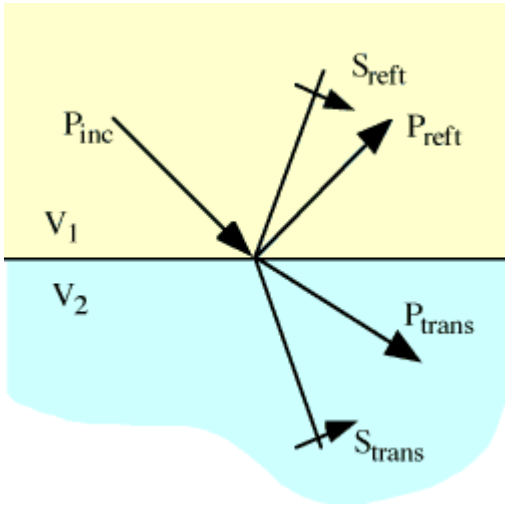

FIG. 2.1 Reflected and refracted waves when a P-wave strikes an interface (After www.crewes.com)

Induced anisotropy can occur when stress produces cracks that have a preferential orientation in the rock. These cracks can be dry or filled with a liquid such that the macroscopic properties of the composite system are anisotropic. Inherent anisotropy is observed in those solids that are homogeneous and anisotropic at the particles or grain level in a rock. Sources of inherent anisotropy include:

- Crystal anisotropy, related to the shape of the crystals of a rock,
- Induced anisotropy which occurs when stress realign crystals or grains in an initially isotropic body, and Lithologic anisotropy, which occurs in sedimentary rock is composed of flat or elongated isotropic or anisotropic grains, that are preferentially aligned in the rock, such as commonly occurs with clays as they change to shales.

Transverse isotropic media has the same elastic properties in any direction perpendicular to a unique symmetry axis. This type of anisotropy can be produced from clay crystal

alignment during sedimentation, from parallel thin stratified layers or from fractures oriented perpendicular to the symmetry axis.

The two most common occurences of transverse isotropy for sedimentary rocks are called Horzizontal Transverse Isotropy (HTI) and Vertical Transverse Isotropy (VTI). HTI occurs in the subsurface when there are thin parallel horizontal layers (such as shale-sand-shale) that act effectively as a composite or 'effective' medium. Since the wave length of the seismic wave is much larger than the thickness of the layers, the composite layered system will vibrate at a lower speed in the vertical direction because the material is less rigid and at a high speed on the horizontal direction, because the material is effectively more rigid in the vertical direction (Figure 2.2).

When the media has a simple set of vertical fractures (the case of interest in this work) or has a preferential direction of stress, the velocity will vary with azimuth, giving rise to the name horizontal transverse isotropic (HTI) or 'azimuthal' anisotropy. When an upcoming shear wave, generated from a P-wave that was reflected from an underlying interface, goes through a vertically fractured layer it will split into fast and slow shear waves which are polarized parallel and perpendicular to the fracture orientation respectively, This splitting phenomenon is called *birefringence*. The fast shear wave is polarized in the more rigid in the direction parallel to the fractures. Conversely, the slow shear wave is polarized in the less rigid direction perpendicular to the fractures in this direction (Figure 2.3).

The measurement of seismic anisotropy can be used to detect and delineate fractured reservoirs. Using birefringence, it is possible to estimate fracture density and orientation, wich can be important for well locations, injection and horizontal drilling.

It has been shown that shear-splitting from PS converted waves provides information on subsurface azimutal anisotropy (Garota and Granger, 1988; Ata and Michelena, 1995; Gaiser *et al.* 2002);, it is also possible to map anisotropy attributes such as the polarization directions and the degree of anisotropy.

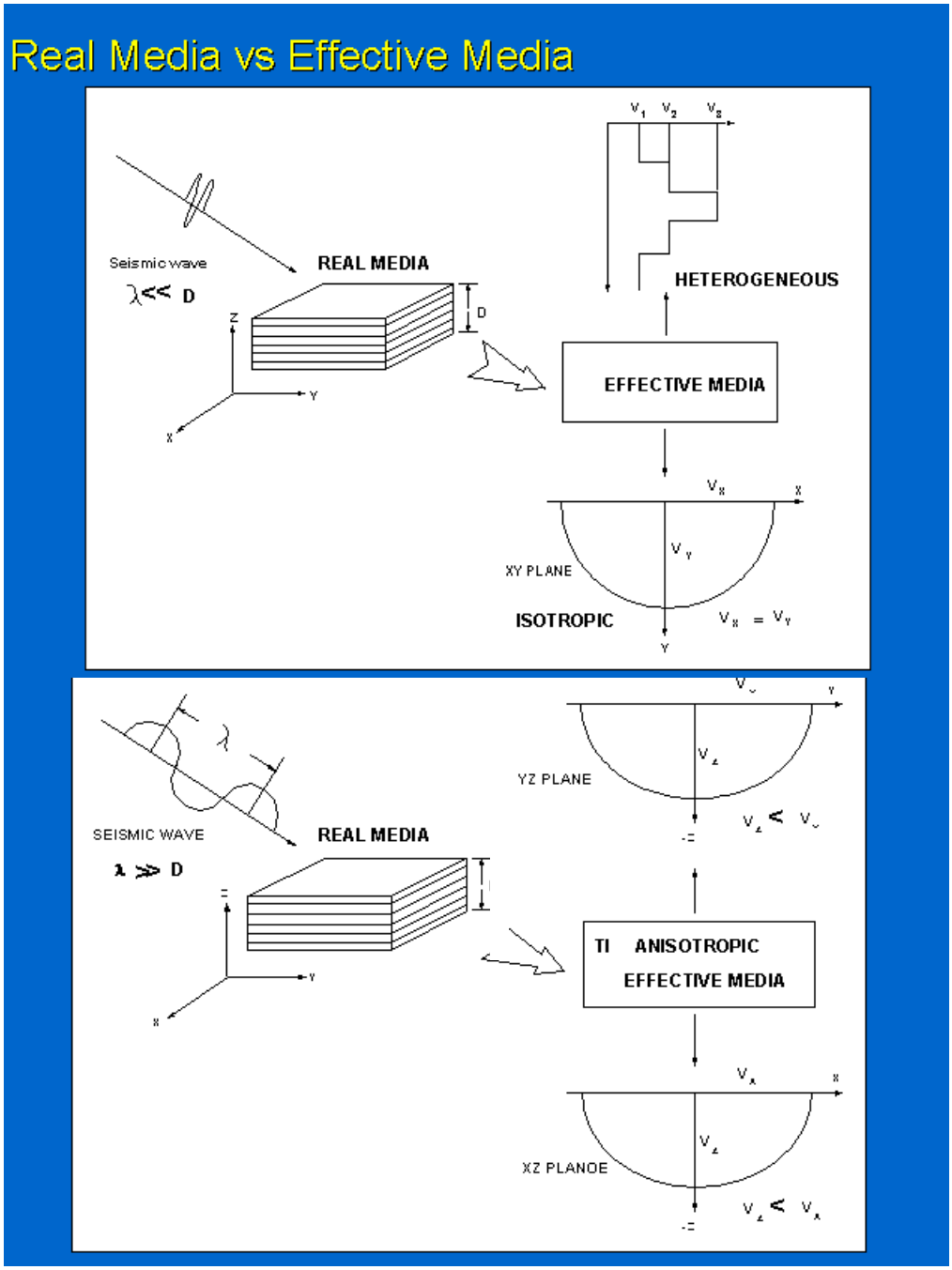

FIG. 2.2 Thin layered isotropic media act as a single, homogeneous, but anisotropic 'effective' media when the wavelength is much larger than the layer thicknesses.

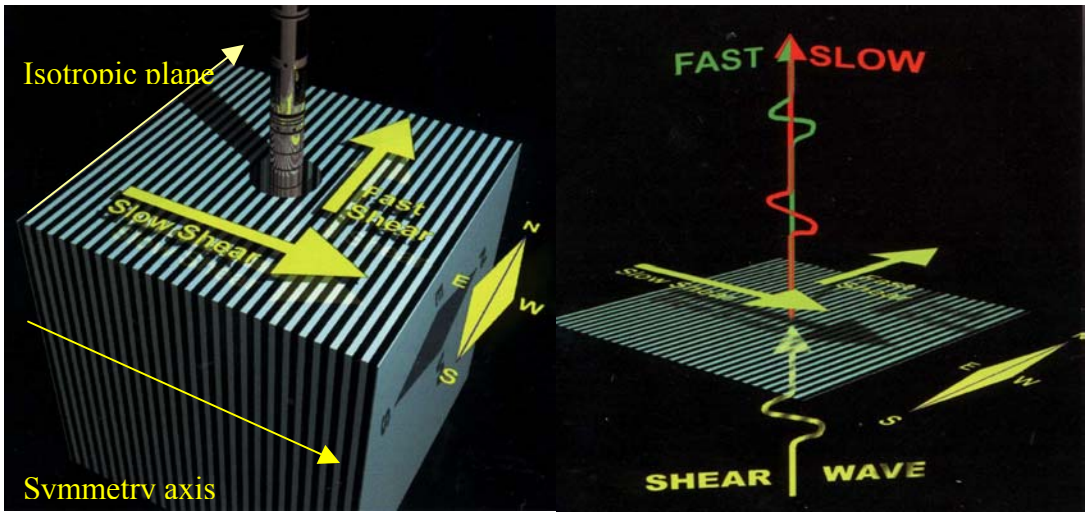

FIG. 2.3 When a shear wave goes through a vertical fractured media it splits into a fast shear wave polarized parallel to the direction of fractures and a slow shear wave polarized perpendicular to the direction of fractures. (After Chenin & Joyce, 1998)

2.2 Wave propagation in isotropic media

The purpose of this section is to show the mathematical formulation of wave equation that gives rise to two modes of propagation in isotropic media, P-wave propagation and S-wave propagation.

A medium is considered elastic when it returns to its original non-deformed state after external forces are removed from the medium. According to Hook's Law, when deformations are small they are proportional to the stress applied over the body. If the stress increases the relationship becomes non-linear, trespassing the elastic boundary where the deformations turn to be plastic and the medium does not turn to its original state when the forces are removed from the media. Seismic waves produce small deformations far away from the source, such that the linear approximation holds. It is assumed that the stress tensor components σ_{ij} are proportional to the tensor strain components e_{kl}. In this way Hook's Law can be expressed as:

$$\sigma_{ij} = C_{ijkl} e_{kl}, \tag{2.1}$$

where the proportionality coefficients are the 81 independent components of the elasticity (or stiffness) tensor C_{ijkl}. C_{ijkl} possesses several symmetries that reduce the number of independent elements. First, due to the symmetry of the stress and strain tensors, it is possible to interchange the indices *i* and *j*, *k* and *l*. In this way the most general anisotropic triclinic model will have only 21 independent stiffness. Since four-dimensional matrices are difficult to write, engineers and geoscientists reformat the 3x3 stress and strain tensor into 6x1 vectors. This reformatting reduces the 3x3x3x3 stiffness tensor into a 6x6 stiffness matrix, for which 21 of the 36 elements are independent. Using this new, more compact notation, we note that if the medium is isotropic (all directions of wave propagation are equivalent), we obtain:

$$C^{(iso)} = \begin{pmatrix} \lambda+2\mu & \lambda & \lambda & 0 & 0 & 0 \\ \lambda & \lambda+2\mu & \lambda & 0 & 0 & 0 \\ \lambda & \lambda & \lambda+2\mu & 0 & 0 & 0 \\ 0 & 0 & 0 & \mu & 0 & 0 \\ 0 & 0 & 0 & 0 & \mu & 0 \\ 0 & 0 & 0 & 0 & 0 & \mu \end{pmatrix}, \tag{2.2}$$

where λ and μ are Lamé's constants.

Using Hooke's law and Newton's second law, we can derive the equation of motion in terms of displacement and stress. The vector form of this equation may be written as:

$$\rho\ddot{\vec{u}} = (\lambda+2\mu)\nabla(\nabla \bullet \vec{u}) - (\mu(\nabla \times \nabla \times \vec{u}), \tag{2.3}$$

which is the general equation of motion in vector notation, where $\vec{u}$ is the displacement vector and ρ is the density.

From the equation of motion (2.3) is it possible to derive the wave equation for both P-wave and S-wave propagation. Taking the divergence of the equation of motion 2.3, and applying some vector identities, we obtain:

$$\nabla^2(\nabla \bullet \vec{u}) = \left(\frac{\rho}{\lambda + 2\mu}\right)\frac{\partial^2}{\partial t^2}(\nabla \bullet \vec{u}), \tag{2.4}$$

which is the wave equation for P-wave propagation. Note that the physical quantity that propagates is the divergence of the vector displacement or dilatation. Physically this is the change in volume per unit volume, or volumetric strain. The P-wave propagation velocity may be described by $v_p^2 = \left(\frac{\rho}{\lambda + 2\mu}\right)^{-1}$.

On the other hand, taking the curl of the equation of motion (2.3) and applying some vector identities, we obtain:

$$\frac{\rho}{\mu}\frac{\partial^2(\nabla \times \vec{u})}{\partial t^2} = \nabla^2(\nabla \times \vec{u}), \tag{2.5}$$

which is the S-wave equation for S-waves. Note that $v_s^2 = \left(\frac{\rho}{\mu}\right)^{-1}$. Also note that the physical property propagated as a S-wave is the vector curl, or rotation, of the displacement. Since their propagation involves only distortion, and no volume changes, they are sometimes referred as distortional waves. The shear wave velocity depends only on one elastic constant, the rigidity (μ).

2.3 Wave propagation in anisotropic media

In the previous discussion, the assumptions of isotropy were made very early in the development prior to the definition of the equation of motion. If an anisotropic medium is to be considered, the problem becomes much more complex. To keep the problem manageable, some assumptions about the symmetry and geometry of anisotropy are commonly made. Since in this study we are going to be focusing on vertical fractures we are going to consider wave propagation in HTI medium. In most cases, HTI media are

caused by a system of parallel vertical cracks embedded in an isotropic background. Hence, horizontal transverse isotropy is the simplest possible model of a formation with vertical fractures. Description of seismic fractured characterization methods for HTI media can be found in Bakulin *et al*. (2000). Deviation from the misalignment of the crack planes, the addition of a second crack system, and vertical fracturing of an originally VTI medium lower the symmetry of the effective medium to orthorhombic or less (Tsvankin, 2001).

The HTI model has two mutually orthogonal vertical planes of symmetry, the symmetry axis plane and the isotropy plane (Figure 2.3). The corresponding stiffness matrix has the form (Bakulin *et al*., 2000):

$$C^{(iso)} = \begin{pmatrix} (\lambda+2\mu)\Delta N & \lambda\Delta N & \lambda\Delta N & 0 & 0 & 0 \\ \lambda\Delta N & \dfrac{\lambda^2}{\lambda+2\mu}\Delta N & \dfrac{\lambda^2}{\lambda+2\mu}\Delta N & 0 & 0 & 0 \\ \lambda\Delta N & \dfrac{\lambda^2}{\lambda+2\mu}\Delta N & \dfrac{\lambda^2}{\lambda+2\mu}\Delta N & 0 & 0 & 0 \\ 0 & 0 & 0 & \mu\Delta T & 0 & 0 \\ 0 & 0 & 0 & 0 & \mu\Delta T & 0 \\ 0 & 0 & 0 & 0 & 0 & \mu\Delta T \end{pmatrix}, \qquad (2.6)$$

where:

$$\Delta N = \frac{(\lambda+2\mu)K_N}{1+(\lambda+2\mu)K_N}, \quad \Delta T = \frac{\mu K_T}{1+\mu K_T},$$

the values K_N and K_T are non-negative and have the physical meaning of the normal and tangential compliances (the compliance is the inverse of the stiffness of the solid rock C_{ijkl}).

Although general HTI models are described by 5 independent parameters ($C_{11}, C_{33}, C_{13}, C_{44}$ and C_{55}), the stiffness matrix given by equation 2.6 depends on just four quantities: λ and μ of the host rock and the dimensionless weaknesses ΔN and ΔT.

The equation of motion can be derived following the same procedure followed for isotropic media. One of the most important characteristics of wave propagation in HTI media is the birefringence phenomenon. For a seismic survey, this phenomenon can produce substantial complexities. If the survey generates P-wave energy into the Earth whose particle motion is polarized parallel to the ray path direction converts into S-wave at each reflector. In the presence of anisotropy, this upcoming shear energy is split and recorded at the surface. Such shear wave splitting can considerably degrade the interpretability of S-wave images. Fortunately, we can compensate for this splitting and largely restore the image by recording both the horizontal and vertical receiver components in the field, and then rotating the source and the receiver coordinate frames into alignment with the data back into the natural polarization directions in processing. In this manner we not only obtain cleaner, easier to interpret reflections, but we also obtain direct information on the orientation and intensity of the anisotropy causing fractures. More discussion on the role of anisotropy in data processing is presented in Chapter 7.

Chapter 3: Geologic Framework

3.1 General overview of venezuelan geology

Venezuela forms part of an important hydrocarbon province, defined by the presence of prolific Cretaceous source rocks that extend across northern South America. By early 1997, the country produced a cumulative 53 billion barrels of oil (James, 2000). Reserves are estimated to total 73 billion barrels of oil and 146 trillion cubic feet (TCF) of gas with an additional 250 billion barrels of recoverable heavy oil. Most reserves are located within the intermountain Maracaibo, Barinas-Apure and Eastern Venezuela basins.

The province hydrocarbon history began with a broad passive margin over which the sea transgressed throughout much of the Cretaceous. Limestones and shales followed basal sands and included rich source rocks. Convergence between the distal part of the area and the Caribbean plate occurred along an active margin that migrated southwards, so that flysch (a graded, thinly-bedded, poorly fossiliferous sequence of marls, sandy to calcareous shales interbedded with coarser sandstones, conglomerates and greywackes) and wildflysch followed the transgressive facies. The process culminated in the late Cretaceous to middle Eocene contractional deformation characterized by emplacement of southward-vergent nappes and the development of northward deepening foredeeps. Major phases of hydrocarbon generation from Jurassic-Cretaceous source rocks occurred across the entire margin of northern South America prior to the orogeny. They are recorded by Jurassic-Middle Cretaceous graphitic marbles, schists and quartzites (methamorphosed, organic limestones and shales and oil-bearing sandstones) in the Coastal and Northern Ranges of Venezuela and Trinidad.

From Late Eocene to recent times, a transpressional plate boundary (the simultaneous occurrence of strike-slip faulting and compression, or convergence, of the Earth's crust) existed between northern South America and the neighboring parts of the Caribbean and the Pacific plates. This resulted in inversion of Mesozoic extensional systems below the remaining passive margin. The area was subdivided into a series of

intermontane, foreland and pull-apart basins bounded by transpressional related uplifts, the latter suffering considerable shortening and strike slip displacement. Sedimentation progressed from deep marine to deltaic and molassic facies, providing reservoir sands and local source rocks.

Reactivated faults, and foreland flexuring and related sedimentation produced abundant structural and stratigraphic traps. Hydrocarbons from earlier accumulations suffered further maturation locally, remigrated to younger traps or escaped to the surface. Further hydrocarbon generation, involving upper Cretaceous source rocks, occurred in local foredeep kitchens. Minor hydrocarbon generation also occurred within tertiary strata.

3.2 Borburata Field

Our study area is located in the Borburata Field within the Barinas-Apure Basin, which lies to the south east of the Andean Mountain Range, southwest Venezuela (Figure 3.1). The majority of Venezuelan fields produce from sandstones. Nevertheless, some produce from carbonates. The main clastic reservoirs include the Escandalosa and Burguita (Cretaceous) formations, the Orocué Group (Paleocene), and the Mirador-Guafita (Arauca member) (Eocene-Oligocene), (Figure 3.2). The most relevant carbonate reservoirs are the limestones with secondary porosity in the Guayacán member, and in the Escandalosa Formation. Regional scale seals are shale intervals of the Burgüita (Late Cretaceous), the Pagüey (Eocene) and the Guafita (Guardulio Member) Formations, (Figure 3.3). Both carbonate reservoirs and shale seals are found in the Escandalosa Formation, which forms the focus of this study. The main source rock is the Navay Formation, shown in the stratigraphic column (Figure 3.2), is of Late Cretaceous age. The main reservoir is in the “O” Member of the Escandalosa Formation (Figure 3.2) which is a fractured limestone, and is our target for fracture characterization. The Escandalosa thickness varies from 150 to 450 m, and is located at an approximated depth of 3 000 m.

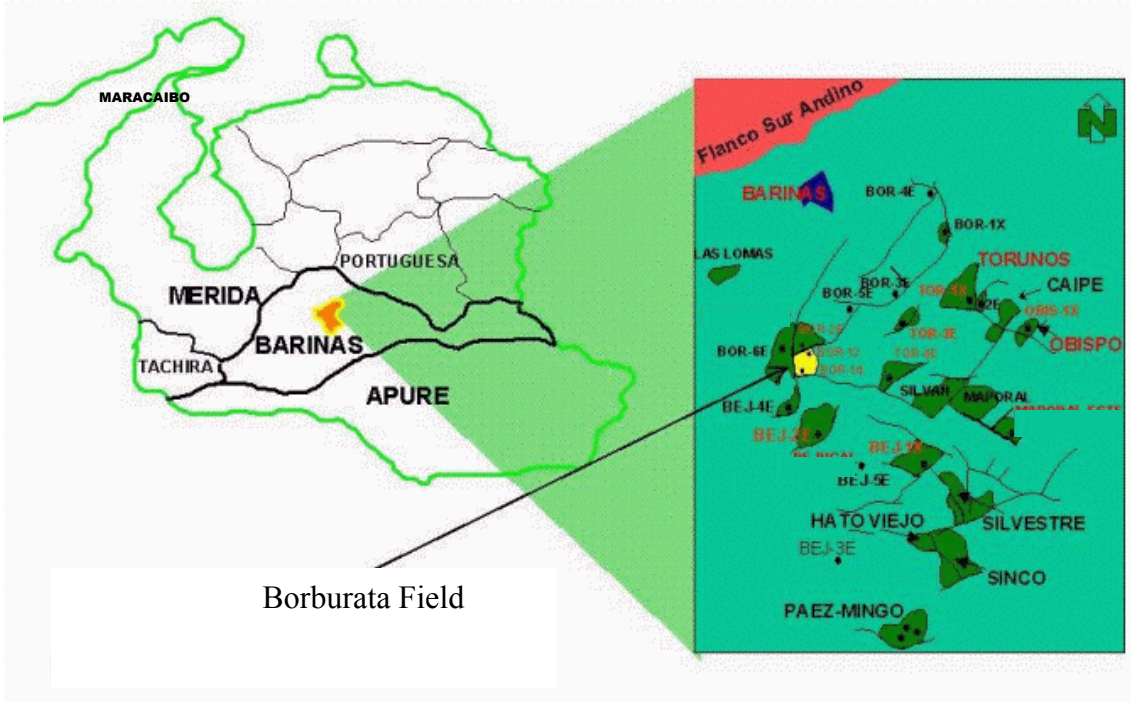

Borburata Field

FIG. 3.1 Borburata Field location in the Barinas Basin (After www.pdv.com/lexico)

In the Early Cretaceous, a marine transgression caused innundation of the Guayana Shield. This transgression is correlated to eustatic sea level rise that lasted till Cenomanian – Campanian time (Parnaud *et al*, 1995). Sporadic volcanic material within the La Luna and Navay Formations suggests the presence of a volcanic arc to the west. The apparent reduction of fault-controlled subsidence, the deepening of the basin, and the stratigraphy suggests that the Early Cretaceous stratigraphic section was deposited as a passive margin terrace wedge behind a volcanic arc. The passive margin phase ended with the collision of the Pacific Arc and the South American plate and flexural subsidence of the foreland basins.

During this period of passive margin development, several sequences were deposited. The structural style is characterized by steeply dipping reverse faults of post-Cretaceous age.

Foreland downwarping following deposition of Early Cretaceous sequences resulted in episodic late Cenomian early Campanian transgression and three depositional sequences. These sequences are represented in the Barinas Basin as the Escandalosa (P and O Members) and Navay Formations.

Uplift of the Merida Andes initiated in the late Oligocene, and by the middle Miocene they separated the Maracaibo and the Barinas-Apure Basin (James, 2000). Adjacent depocenters known as the North and South Andean fordeep, received coarse clastic deposits assigned to the Parangula Formation (Figure 3.2). Thereafter, the relative stable Barinas-Apure Basin continued to accumulate continental sediments of the Parangula Formation.

3.3 Geological occurrence and migration of oil

There is considerable debate regarding the definition of kitchen areas and the timing of oil generation (James, 2000). Structural analysis based upon aeromagnetic data calibrated by seismic and well data (Young 1998) has defined numerous structural elements parallel to the adjacent Merida Andes. NE-SW faults (parallel to the Andes) are common. They extend for 40-80 km and show reverse right-slip displacements. In addition, there are east-west trending structures in the north-central part of the area, which according to James (2000) are related to deformation along the plate boundary to the north. The structures are either pre-Oligocene or Mio-Pleistocene. Only the former constitute important traps for oil. According to Talukdar (1992) the fault and fold structure in Barinas Field formed in the Late Cretaceous-Paleocene and were reactivated in the late Eocene.

The Barinas Field lies on the northern portion of the Merida arch (Figure 3.1) and is traditionally ascribed to anticline and fault trapping, the latter being more important. The structures have low structural relief. Basal Tertiary and highly porous and permeable sandstone belonging to the upper Cretaceous Escandalosa Formation have reservoirs with an oil gravity of 22-25° API . Porosities range from 20 – 28 % and permeabilities are in the range of 200-2000 mD.

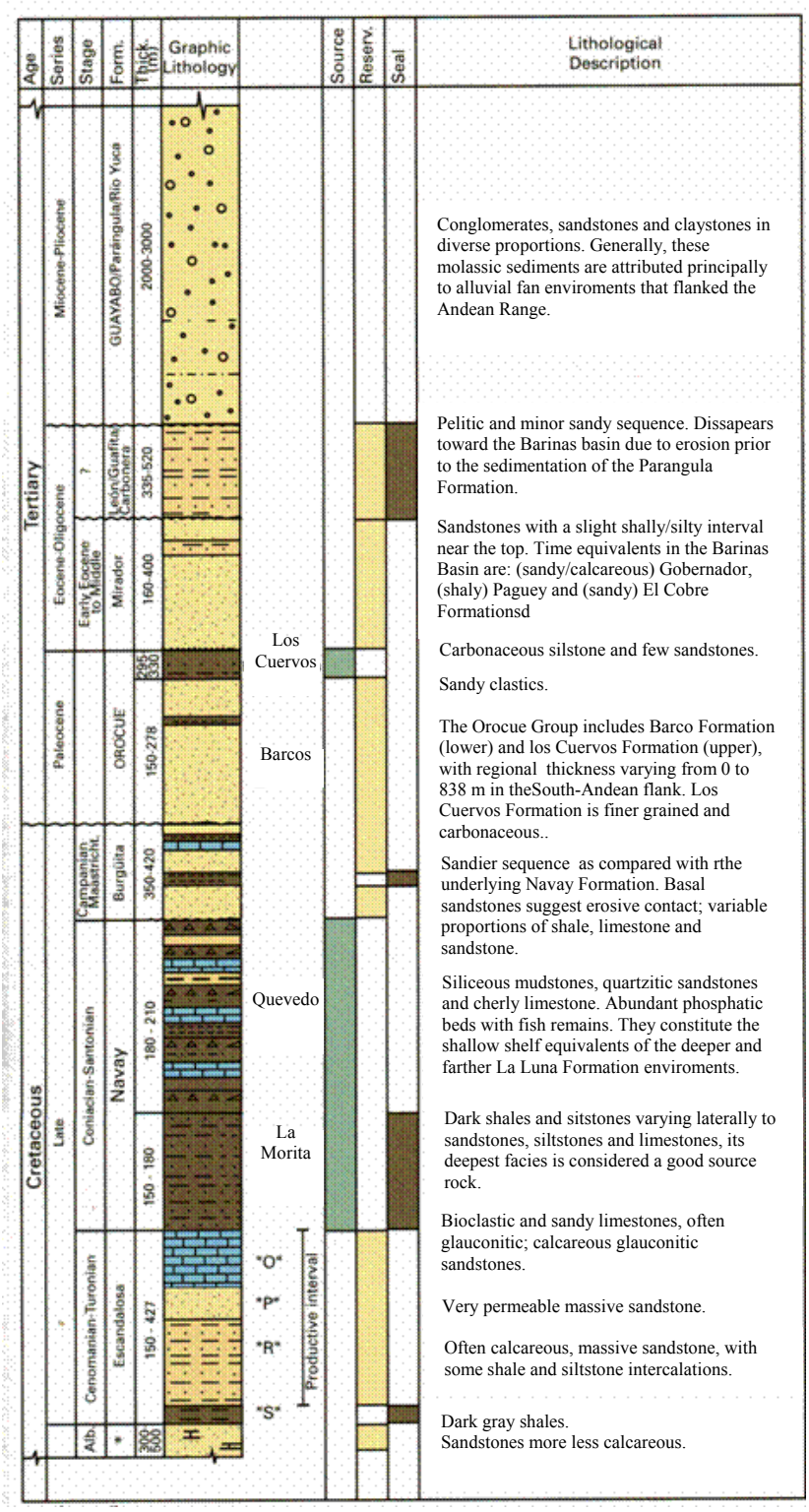

FIG. 3.2 Composite stratigraphic column of the South Andean flank, Barinas-Apure basin. (Schlumberger well evaluation conference, 1997)

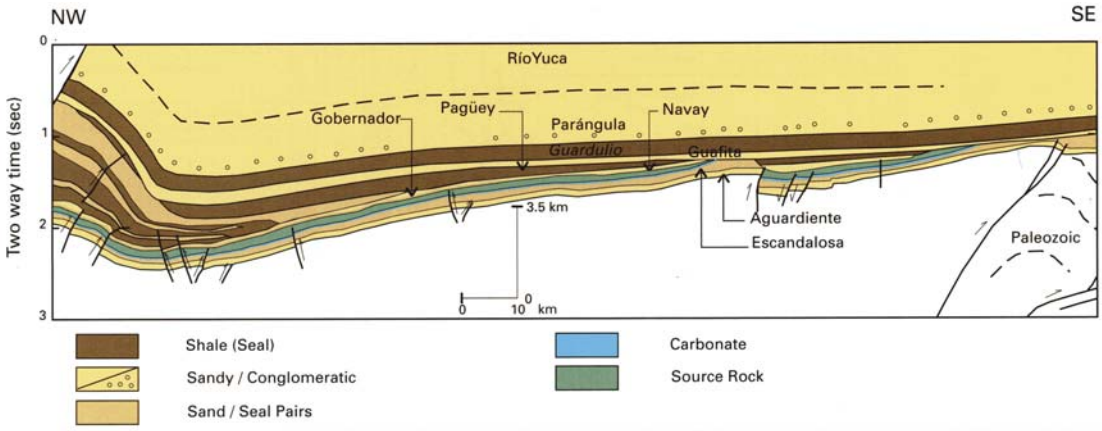

FIG. 3.3 NW-SE cross section of the Barinas-Apure Basin. (Schlumberger well evaluation conference, 1997)

Migration has occurred laterally over long distances to structural and stratigraphic traps on the foreland ramp, and vertically to fold and thrust related structural and stratigraphic traps in the sub Andean-zones.

3.4 Fractures, a general overview

Different types of fractures form in different orientations relative to the stress field that prevailed at the time of fracturing. Correctly identifying fracture type is essential for predicting the orientations of fracture populations as a whole, and therefore for planning optimum drilling direction and for building reservoir models. Certain types of fractures form only in specific rock types or in specific geologic environments. This study focuses on fractures in carbonates. Certain types of fractures have particular shape/size distributions and obey particular density (spacing) laws that can be used to build 3D reservoir models.

Lacazette (2001) defines fracture as "a general term for any non-sedimentary mechanical discontinuity thought to represent a surface or zone of mechanical failure. Chemical processes such as solution and stress corrosion may have played an important role in the failure process. The term is used to describe a natural feature either when

available evidence is inadequate for exact classification or when distinction between fracture types is unimportant".

Fractures can be classified by the movement sense: In Mode 1, the walls move perpendicular away from the fracture plane when the fracture forms. In Mode 2, the walls slide parallel to the fracture as a shear. In Mode 3 the walls tear apart and slide at one end of the fracture but remained locked at the other end (Figure 3.4). A natural rock fracture formed predominantly by mode 1 movement is called joint (Engelder, 1987) and a type of natural rock formed predominantly by mode 2 and/or mode 3 movements typically evolve into a fault (Lacazzete, 2001).

Stress is defined as the force per unit area acting on a plane. Any stress state at a point in a solid body can be described completely by the orientations and magnitudes of the three orthogonal principal stresses (Figure 3.5). The principal stresses are defined as $\sigma_1 > \sigma_2 > \sigma_3$ with the compressive stress (and corresponding shortening strain) considered positive in rock mechanics and structural geology because (except around underground voids such as caves or very near to the earth's surface) in the earth all three principal stresses are always compressive. Joints (extensional fractures) seem paradoxical because they are one of the most common types of natural rock fracture even though they require an effectively tensile driving stress. Pore-fluid pressure drives most joints by producing effective tensile stress through poroelastic loading of flaws that are orders of magnitude larger than typical pores.

In Figure 3.5, we can see a joint, colored in green, is always perpendicular to σ_3 at the joint tip during propagation. Curved joints are indicative of variations in the orientation of σ_3 during joint growth. Faults, colored in red, are shown in Figure 3.5. New faults form with an approximately constant acute angle between σ_1 and the two conjugate fault orientations. Pre-existing discontinuities with a wide range of orientations can be activated as faults, provided they are not oriented perpendicular to a principal stress.

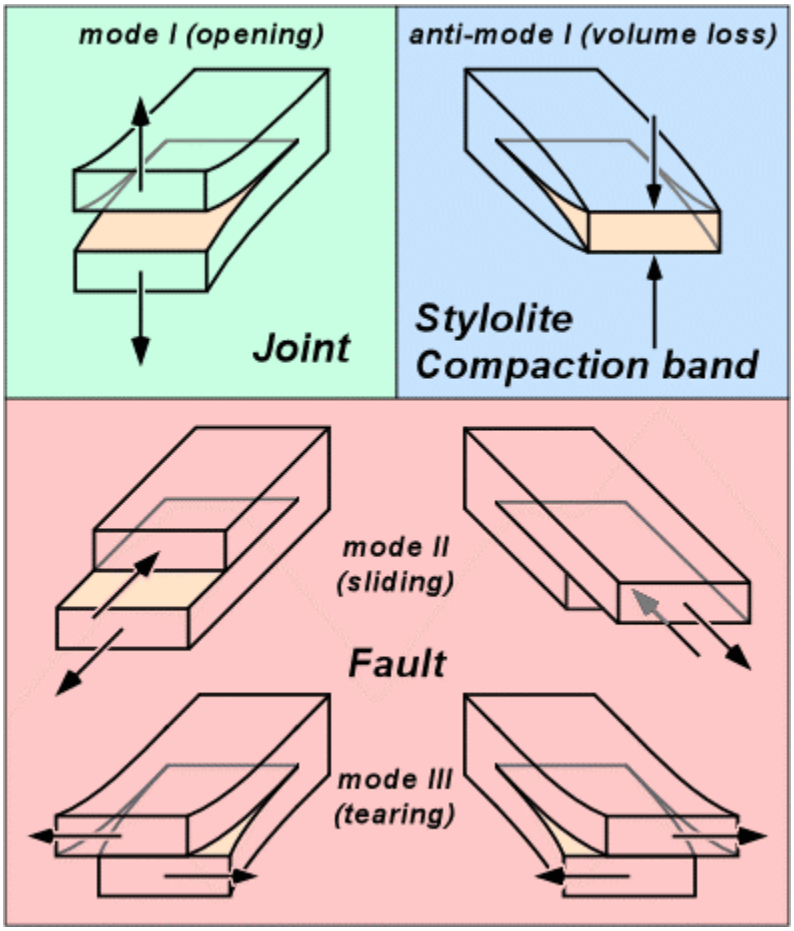

FIG. 3.4 Fracture mode and geologic fracture names (After Lacazette, 2001)

In Figure 3.5, shown in blue is a stylolite, which forms perpendicular to σ_1. A stylolite is a zone of insoluble residue produced by stress-enhanced dissolution and are more common in carbonates than in clastics). Stylolites typically have a cone-in-cone structure that produces a characteristic zigzag appearance in cross section. Stylolites may serve as flow barriers because the insoluble residue is very fine-grained and clay-rich. However, stylolites are very weak and are easily reactivated as joints by later tectonic events.

Tectonic fractures are those whose origin can, on the basis of orientation, distribution, and morphology, be attributed to, or associated with a local tectonic event. They form in networks with specific spatial relationships to folds and fault.

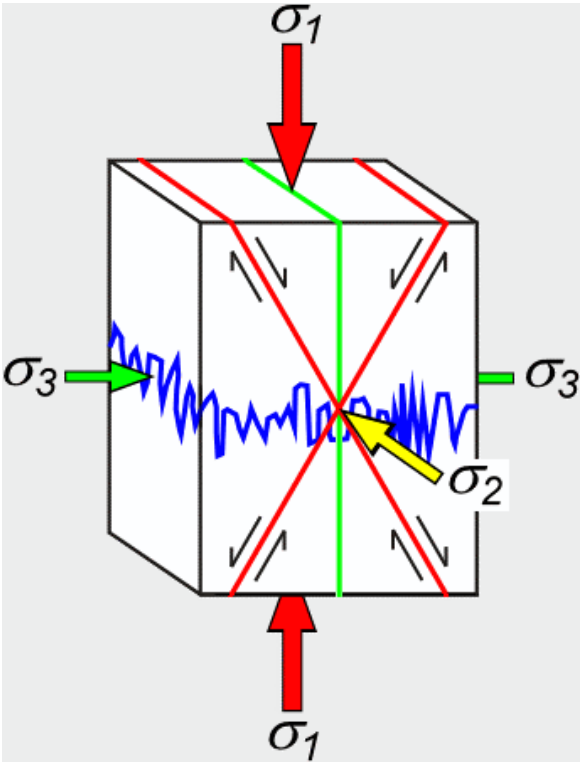

FIG. 3.5 Orientation of stress and fractures (After Lacazette, 2001)

3.5 Tectonic fractures

Fault planes are, by definition, planes of shear motion. The majority of fractures developed in the vicinity of faults are shear fractures parallel to the fault, shear fractures conjugate to the fault, or extension fractures, which have a sense of displacement perpendicular to and away from the fracture plane, bisecting the acute angle between these two shear directions (Figure 3.6). The stress and strain history of a fold in rock is very complex. Therefore, the fracture patterns that develop within the fold are also complex. While the position and intensity of these fractures sets varies with fold shape and origin, most sets are observed on all folds that are studied in detail. In Figure 3.7 you can see all the geometric elements of the fracture systems displayed on an idealized

bedding surface; the fractures are unequally developed in terms of their position and intensity (Ronald, 2001).

An important factor that indicates fracture porosity and permeability is the morphology of the fracture planes. This morphology can be observed in core and outcrop. There are four basic types of natural fracture plane morphology (Ronald, 2001):

1. Open fractures, that possess no deformation or diagenetic material filling the width of the fracture. Such fractures are potentially open conduits to fluid flow. This morphology creates strong anisotropy within the reservoir.

2. Deformed fractures, that either formed as a relative ductile shear zone or were initially open and subsequently physically altered by later tectonic shear motions.

3. Mineral filled fractures, that have been filled by secondary or diagenetic minirealization. Quite often, this secondary cementing material is quartz, carbonate or both. Its effect on permeability depends on the completeness of filling and digenetic history of the material, and

4. Vuggy fractures that are characterized by matrix alteration around the fracture. Vuggy fractures form when the fluids enter a low permeability rock along fracture planes. If the fluid is in disequilibrium with the rock, dissolution may occur.

3.6 Characteristics of natural fractures in carbonate strata

Natural fractures can provide important permeability pathways in carbonate reservoirs. However, adequate prediction of fracture character and spacing in a potential carbonate reservoir is notoriously difficult, in large part due to the variety of potential geologic factors that could influence fracture distribution. These factors include, but are not limited to bed thickness, degree of folding, lithology and structural position.

Since the Escandalosa Formation is a fractured limestone, we are going to focus on fractures in carbonate strata. Carbonates, especially dolomites, are commonly considered to be more highly fractured than clastic sedimentary rocks. Although no

definitive database has been published to support this, carbonate reservoirs are usually recognized to be fractured-enhanced plays, whereas many clastic reservoirs have only recently been widely recognized as such (Lorenz, *et al*. 1997).

Fracture characteristics in carbonates are as variable as the range of carbonate lithologies, fabrics and structural settings (Lorenz, *et al*. 1997). Many fractures in carbonate strata originate in extension, although evidence for fracture origins in shear is not uncommon in tectonized regions. Later shear on extensional fractures can also occur. Regional fractures are widely distributed in most beds, and more localized sets of structure-related fractures occur in association with faults and fold hinges. Fracture distributions vary, with some fractures occurring in swarms interspersed with relatively unfractured rock, while other fractures are pervasively distributed within the strata. Multiple unrelated fracture sets may be superimposed on each other in some places, whereas in other places, later stresses may only reactivate a preexisting set. Fractures are common even in carbonates beds that have not been folded. Fractures in such relatively flat-lying strata can usually be attributed to combinations of basin maturation and far field stresses derived from basin subsidence, uplift, or distant tectonics events. Such fractures are called regional fractures and form parallel or sub parallel to the regional maximum horizontal compressive stress. They are extensive in area and are commonly oriented normal to bedding. They probably form under differential stresses significantly less than those required to fold and fault most strata because they often appear to have formed before the strata were significantly bent or broken.

Different lithologies behave differently to regional fracturing. Regional fracture spacing is usually not related directly to mechanical bed thickness, as it can be when strata are folded. Regional fracture spacing is also a function of (1) the intensity and duration of stresses that caused fracturing and (2) the mechanical properties of the strata; thus, the spacing of regional fractures is difficult to predict.

Fractures are typically filled by calcite, but other mineral precipitates are common. Fractures in carbonates may also have been widened and lengthened by post fracturing dissolution. Most fractures, except in highly deformed strata, are oriented

normal to bedding regardless of the current bedding orientation. Alternately, “conjugate” sets of high angle fractures may have a common strike but opposite senses of dip.

3.7 Escandalosa Formation

The "O" Member of the Cenomanian Turonian Escandalosa Formation (Barinas-Apure Basin, Venezuela) is considered to be a triple-porosity system for dynamic reservoir simulation, with intercrystalline porosity (± connected vugs); non-connected vuggy porosity in a tight matrix; and fractures (Kupecz *et al*., 2000). Figure 3.8a shows the connection of vugs and fractures and Figure 3.8b shows fracture intersection in a core at Borburata field. Figure 3.9 shows evidence of fractures and vugs within the Escandalosa Formation.

The "O" member can be subdivided into nine 4-5th order parasequences, from 1-5 m thick. Due to the depositional and diagenetic complexity, there is a wide range of pore types. However, by integrating petrographic and mercury injection capillary pressure data, these pore types can be grouped into three families having similar flow characteristics, allowing "flow units" to be interpreted and correlated.

Because of the lithological and diagenetic complexity of these thin parasequences, matrix permeability can vary up to five orders of magnitude, thus having significant implications in well completion and well design. Extreme variation of permeability for a given value of porosity makes prediction of permeability in non-cored wells difficult. However, cross-plots of porosity and permeability by pore type 'family' yield significantly improved correlations. Two benefits arise from the improved correlation: 1) equations from regression analysis for each 'family' allows more accurate prediction of permeability, and 2) appropriate porosity-permeability cutoffs for each pore type 'family' allow for more realistic reserves calculations.

3.8 Expected fracture distribution at Escandalosa Formation

The area covered by the seismic acquisition is about 25 km^2. Seismic data shows a reverse fault within flat-lying Early Cretaceous and the middle Eocene-Oligocene strata. The Escandalosa Formation within the study area is folded and cut by a reverse fault, which we will detail in the seismic processing result of this study. The reverse fault is on the west side of the study area and has a west transport direction. Fold axes trend east-west suggesting that the orientation of the maximum principal stress is horizontal and east-west.

The folding situation described above can be visualized in Figure 3.7; as a Mode 1 stress field regime generating joints, which are parallel to the principal stress direction, such that we would expect fractures in the east-west direction. Additionally we anticipate the presence of conjugate shear fractures formed approximately at 30-45 degrees (Lacazette, 2001) to the principal (east) stress direction. Near the reverse fault, the fracture orientation changes. As shown in Figure 3.6, close to the fault plane we expect fractures parallel to the fault as a result of the shear displacement. On the other hand, previous to the faulting we envision some bending of the fold and related conjugate fractures. We therefore expect that the main anisotropic effect is due to the fractures parallel to the fault.

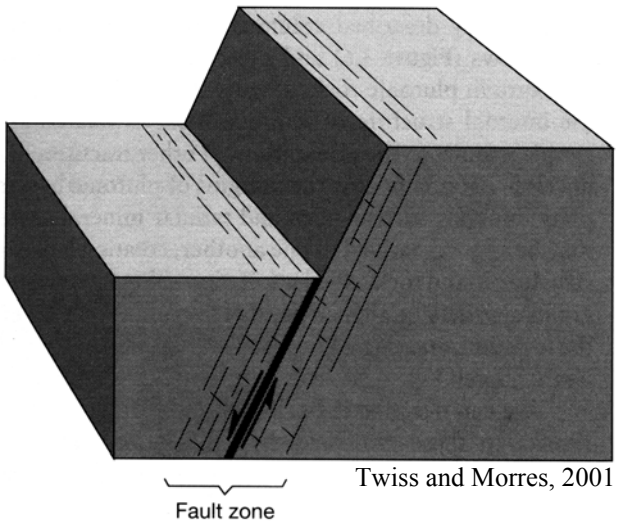

FIG. 3.6 Fractures associated with faults (After Twiss and Morres, 2001)

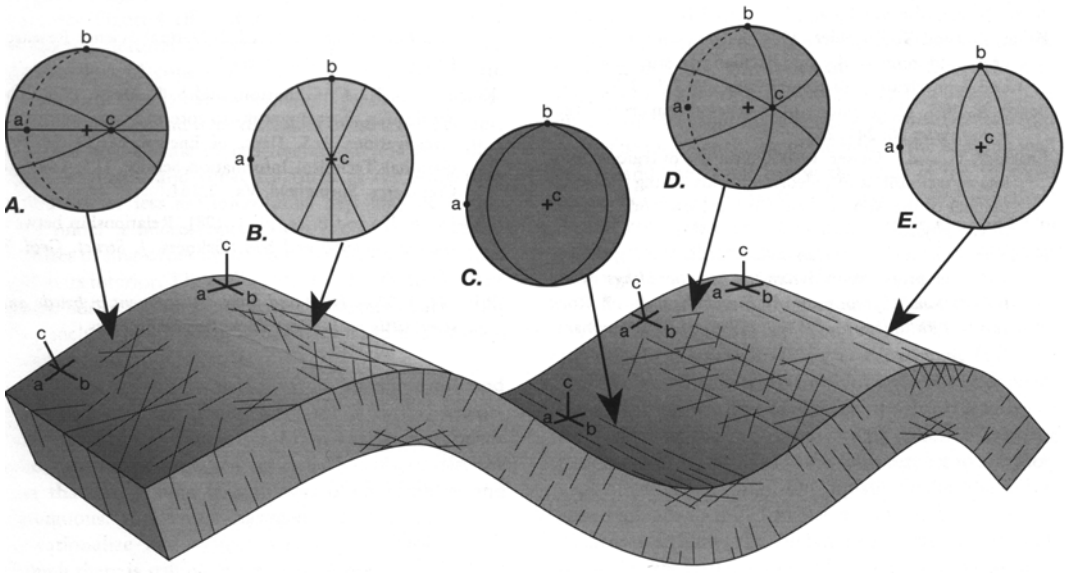

FIG. 3.7 Fractures associated with folds. The stereographic projections show the orientation of the coordinate system, the bedding where it is not horizontal (dotted great circles) and the fractures (solid great circles). (after Twiss and Morres, 2001)

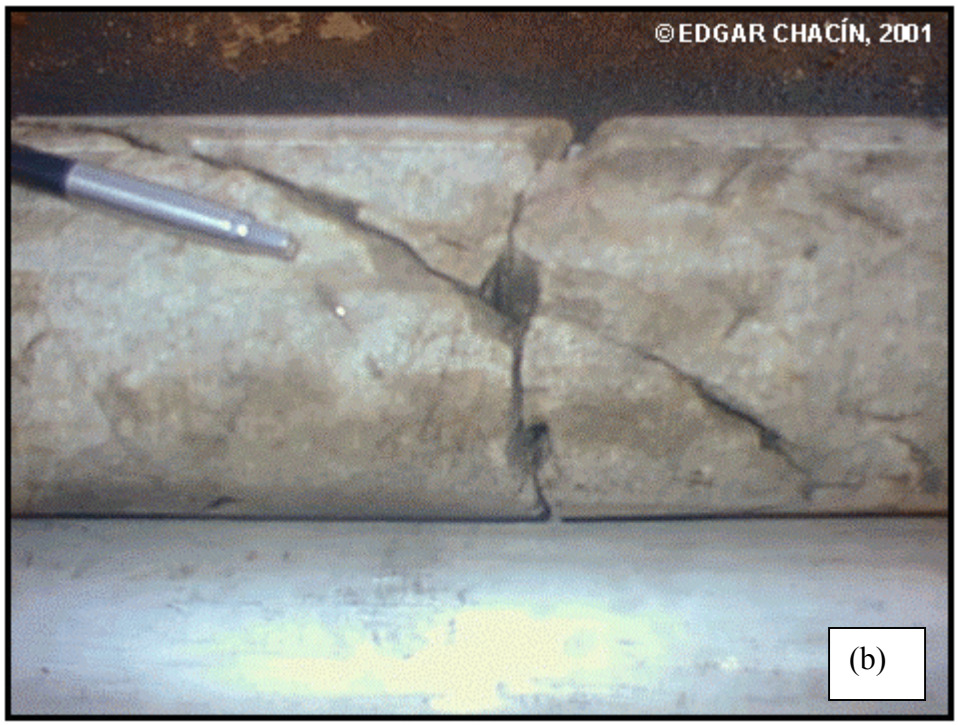

FIG. 3.8 (a) Connection between vugs and fractures in a core sampled at Borburata Field. (b) Intersection of fractures in a core sample at Borburata Field (After www.pdv.com/lexico)

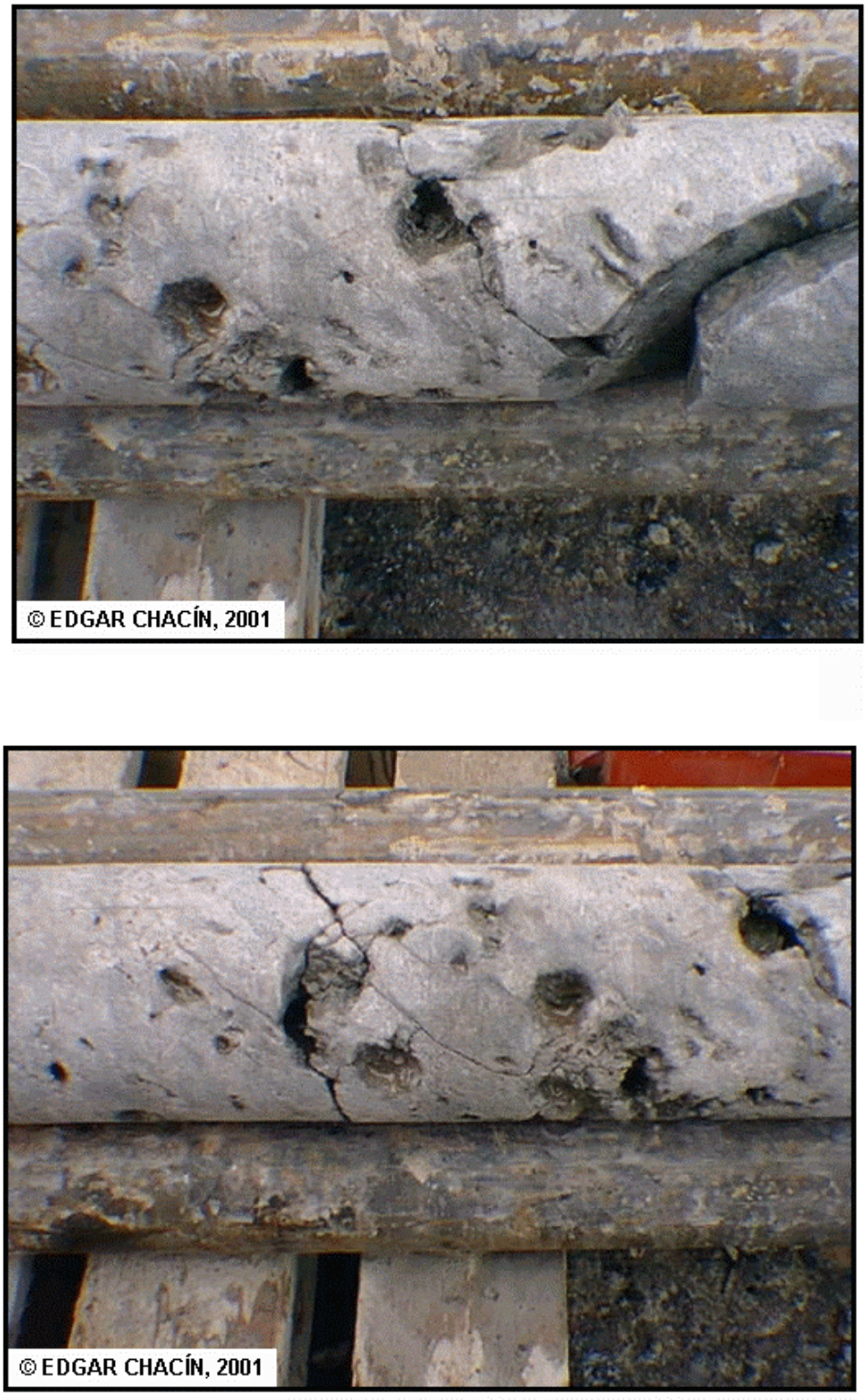

FIG. 3.9. Evidence of fractures and vugs in the Escandalosa Formation (After www.pdv.com/lexico)

Chapter 4: Processing of the seismic data (Vertical Component)

The Borburata survey is conducted over a structurally simple area with the objective being the estimation of fracture orientation and density in a 100 m thick, 3000 m/s, carbonate at approximately 3000 m depth. The area covered by the seismic acquisition is about 25 km^2, and in general, the data have a very good signal to noise ratio.

The processing of the vertical component was performed in Seisup, a commercial seismic processing software marketed by Geocenter.

4.1 Acquisition geometry

In Figure 4.1, we display the acquisition geometry and indicate the source locations by blue triangles and the receiver locations by red squares. The acquisition consists of:

- 720 fixed geophones with three components making a total of 2160 channels, with all channels live for each shot,
- 90 geophones per receiver line,
- 13 shot lines,
- 8 receiver lines,
- 54 m distance between shots,
- 40 m distance between receivers,
- 400 m distance between receiver lines,
- 400 m distance between shot lines,
- a 20 m by 27 m natural bin size ,
- explosive sources,

- 2 ms sampling interval, and
- 8 s record length,

resulting in three data volumes corresponding to the vertical (Z), inline (H1) and crossline (H2) components.

The fold distribution for the P-waves for a bin size of 54 m by 40 m is shown in Figure 4.2a. Its distribution is homogeneous and the area of maximum fold covers a square in the center of the area, mapped in red having a maximum fold of 75-79.

4.2 Seismic processing of the vertical component for PP reflections

Figure 4.3 shows a common shot gather containing receiver lines 1, 2 and part of a receiver line 3. The shot is located in the center of the survey and is indicated by the green triangle in Figure 4.1. The data have good signal to noise ratio with the reflectors well defined and continuous in the data, even though part of the reflector signal is masked by ground roll. We recognize two components of the ground roll noise cone in Figure 4.3: a faster component with a velocity of approximately 500m/s, and a slower component with a velocity of approximately 300 m/s. We interpret this slower component to be an air-coupled event due to its velocity. Both noise trains are aliased at points and flat on receiver lines broadside to shots, making attenuation problematic. The aliased ground roll wraps around in the FK domain (Figure 4.4), making it difficult to apply conventional FK filtering without damaging the signal.

The dominant frequency of the ground roll is at 8 Hz and is many times stronger than the reflected signal. The reflected signal has a dominant frequency at 18 Hz (Figure 4.5).

Before attempting to remove the ground roll we edited the traces, killing some traces were particularly noisy. We then applied datum statics and spherical divergence to compensate for elevation changes, geometric spreading and attenuation in depth. A shot gather with these processes applied can be seen in Figure 4.6.

In order to reduce the ground roll aliasing, we applied a linear moveout followed by an FK filter and inverse linear moveout to restore the original record times. Figure 4.7 shows the shot gather shown in Figure 4.6 with a linear moveout applied of 500 m/s; the flat events that are observed correspond to the 500 m/s component of the ground roll. We note that the 500 m/s component is no longer aliased and is now localized in FK space, allowing us to remove it with a simple mute (Figure 4.8). Such a slow moveout with alias the previously unaliased signals, such that some components will be removed in the FK filter. After linear moveout is restored, we repeat this procedure for the slower 300 m/s event. The 300 m/s is both much stronger and less well organized than the 500 m/s event, and is not easily attenuated. We therefore apply an interior mute to lessen its effect on the final images data. The result is shown in Figure 4.9.

To remove the low frequency component we apply a band pass filter (10,15,40,60) that preserves the frequency content of the reflectors and attenuates the residual low frequency component of the ground roll (Figure 4.10).

Next, we performed velocity analysis to obtain staking velocities used to build a brute stack. These staking velocities were used for residual statics estimation and as the velocity model for pre-stack time. The stacking velocities (Figure 4.11) have very small lateral variations. Figure 4.12 shows the results of 3-D pre-stack Kirchhoff migration. We believe the loss of energy on the reflectors at the edges is due to normalization problems related to the fold (Figure 4.2).

Figure 4.13 shows a 3D view of the area of interest. Event A indicates the strongest regional reflector, which is the top of the (Paguey) shale block indicated in Figure 3.2 and Figure 3.3. Event B is the Escandalosa Formation, the last largest amplitude event. In addition, we are able to clearly identify a reverse fault, C.

Since we know from well control that fractures exist in this field, we analyzed velocity variation with azimuth on the vertical component of the seismic data to see if there was an influence of azimuthal anisotropy on PP reflections. We sorted the data into

six different azimuth and applied the same NMO correction to all 6 volumes. This single velocity cube was able to perfectly flatten the reflectors for each azimuths, thereby implying that the effect of azimuthal anisotropy on PP reflections can be neglected.

We also ran post-stack migration and obtained images having the same resolution as the pre-stack migration. Since there is no azimuthal variation of velocity and no structural complexity, this result is as expected. In the next two chapters we will show that while the PS reflections do exhibit azimuthal anisotropy, each azimuth is able to be imaged with a simple post stack migration.

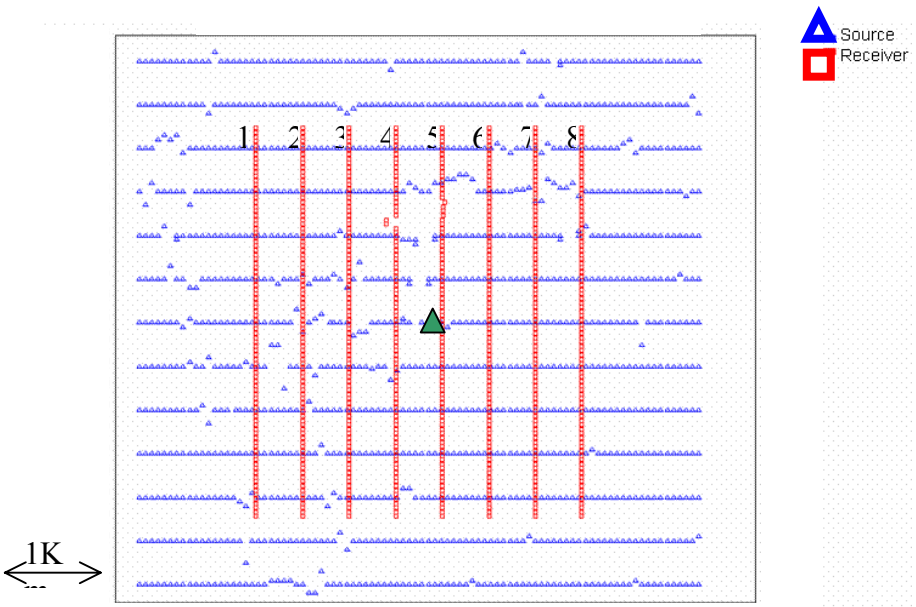

FIG. 4.1 Acquisition geometry over Borburata Field Red squares indicate the receiver positions and blue triangles indicate the shot positions.

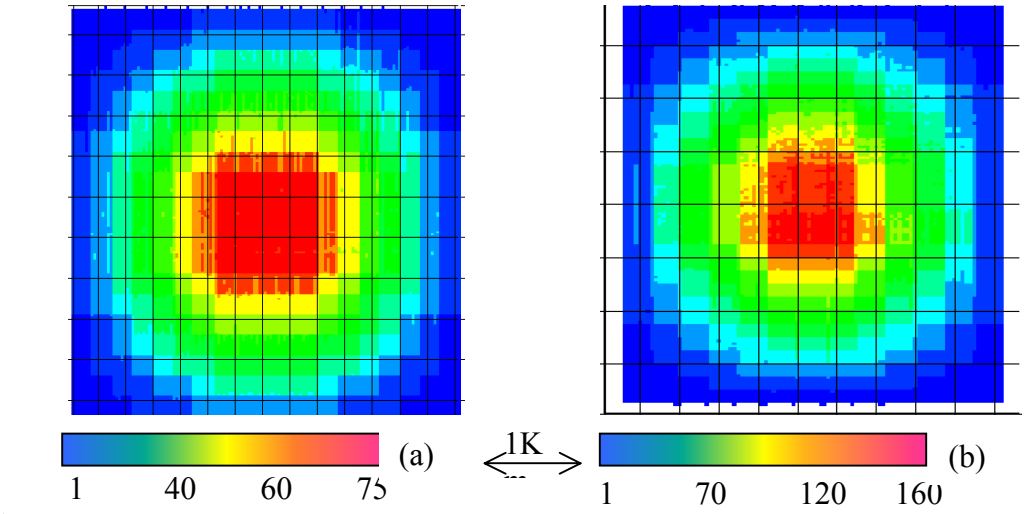

FIG. 4.2 Fold distribution map for (a) PP reflections and (b) PS reflections. Bin size for PP waves is 54 m by 40 m. Bin size for PS data is 36 m by 27 m.

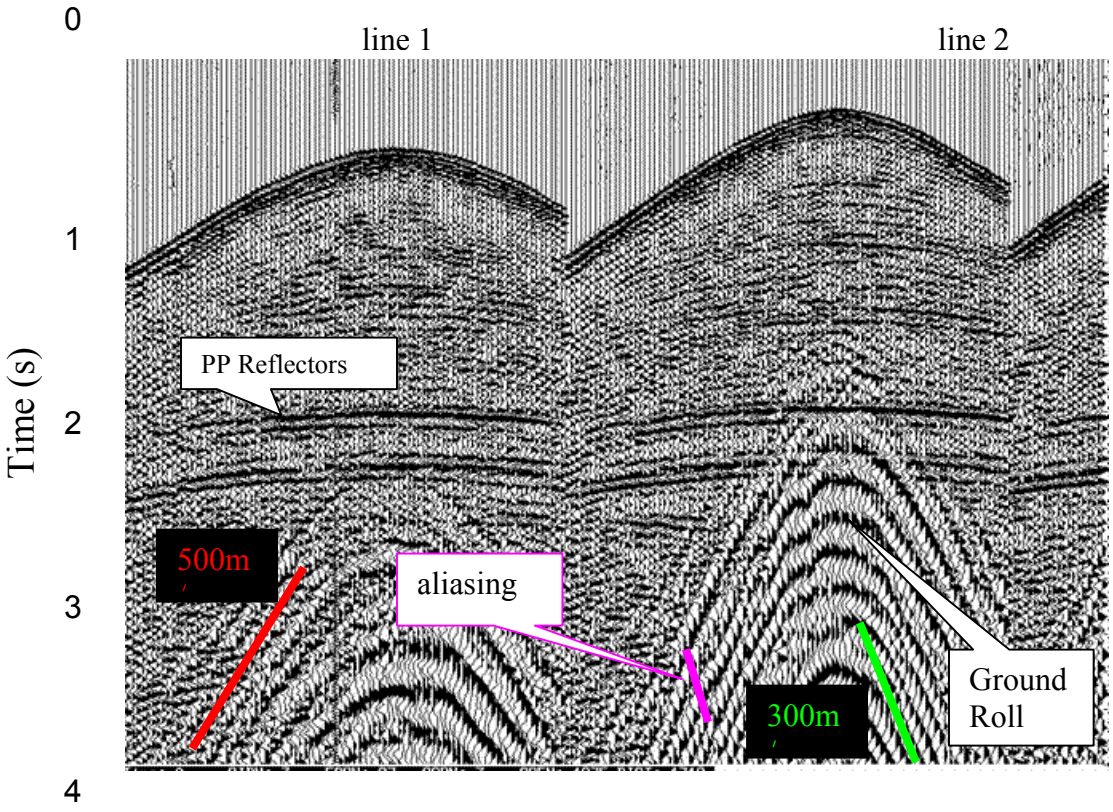
0
1
2
3
4
Time (s)
line 1
line 2
PP Reflectors
500m
aliasing
300m
Ground
Roll

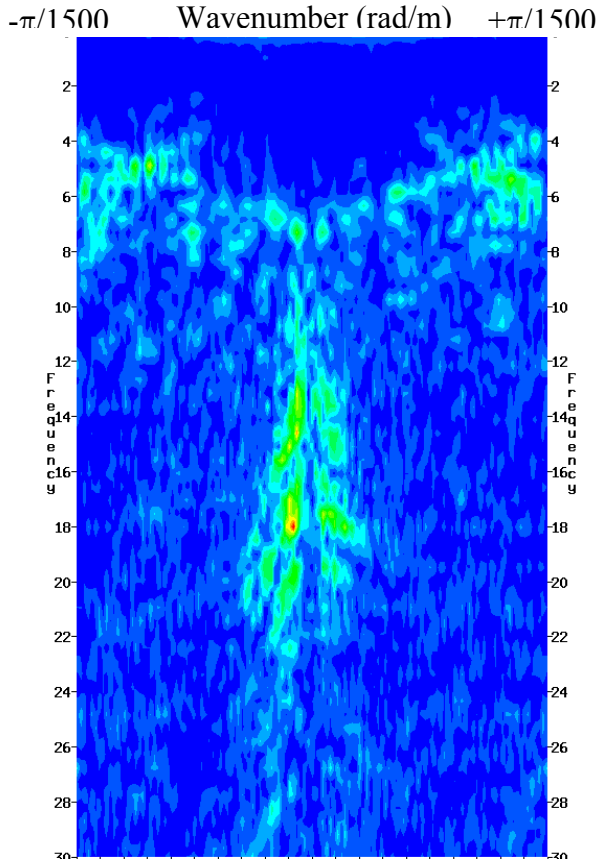

FIG. 4.4 FK spectrum of the vertical component of receiver line 4 shown in Figure 4.3 .

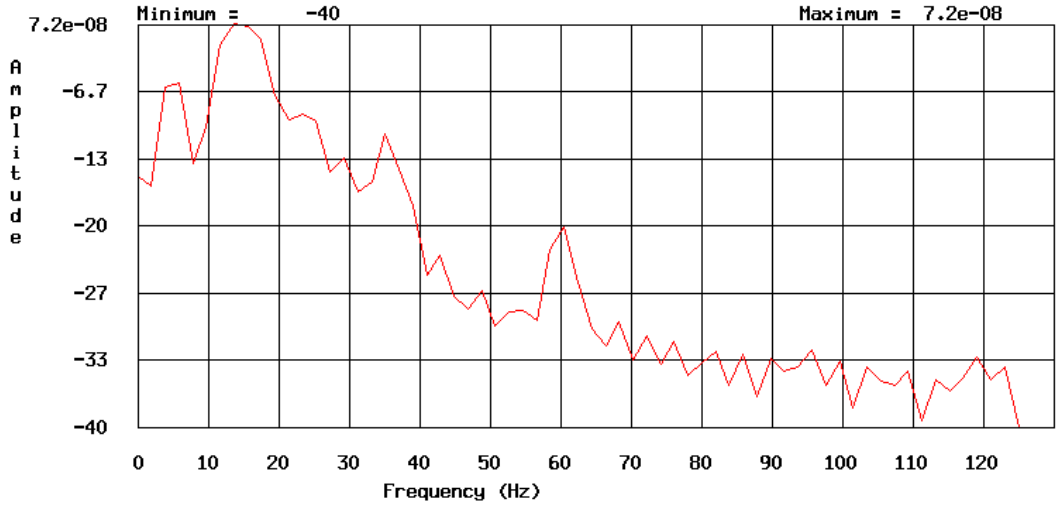

FIG. 4.5 Average amplitude spectrum of the vertical component of receiver line 4 shown in Figure 4.3.

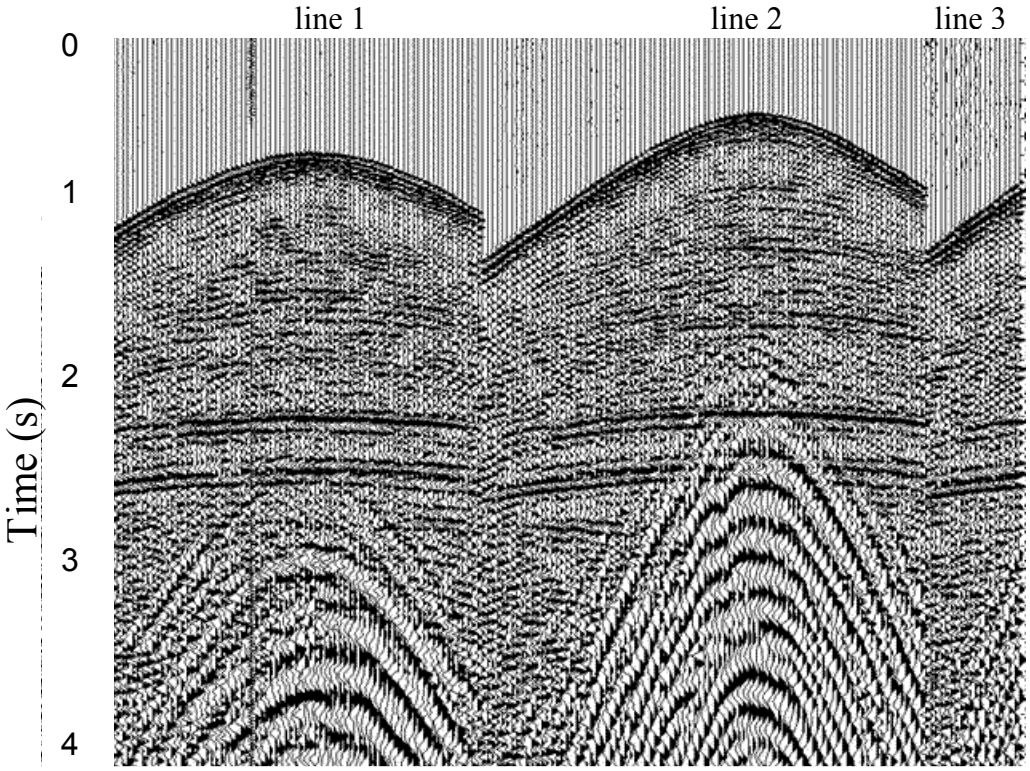

FIG. 4.6 Common shot gather of the vertical component after datum statics, resampling to 4 ms, spherical divergence, and trace editing.

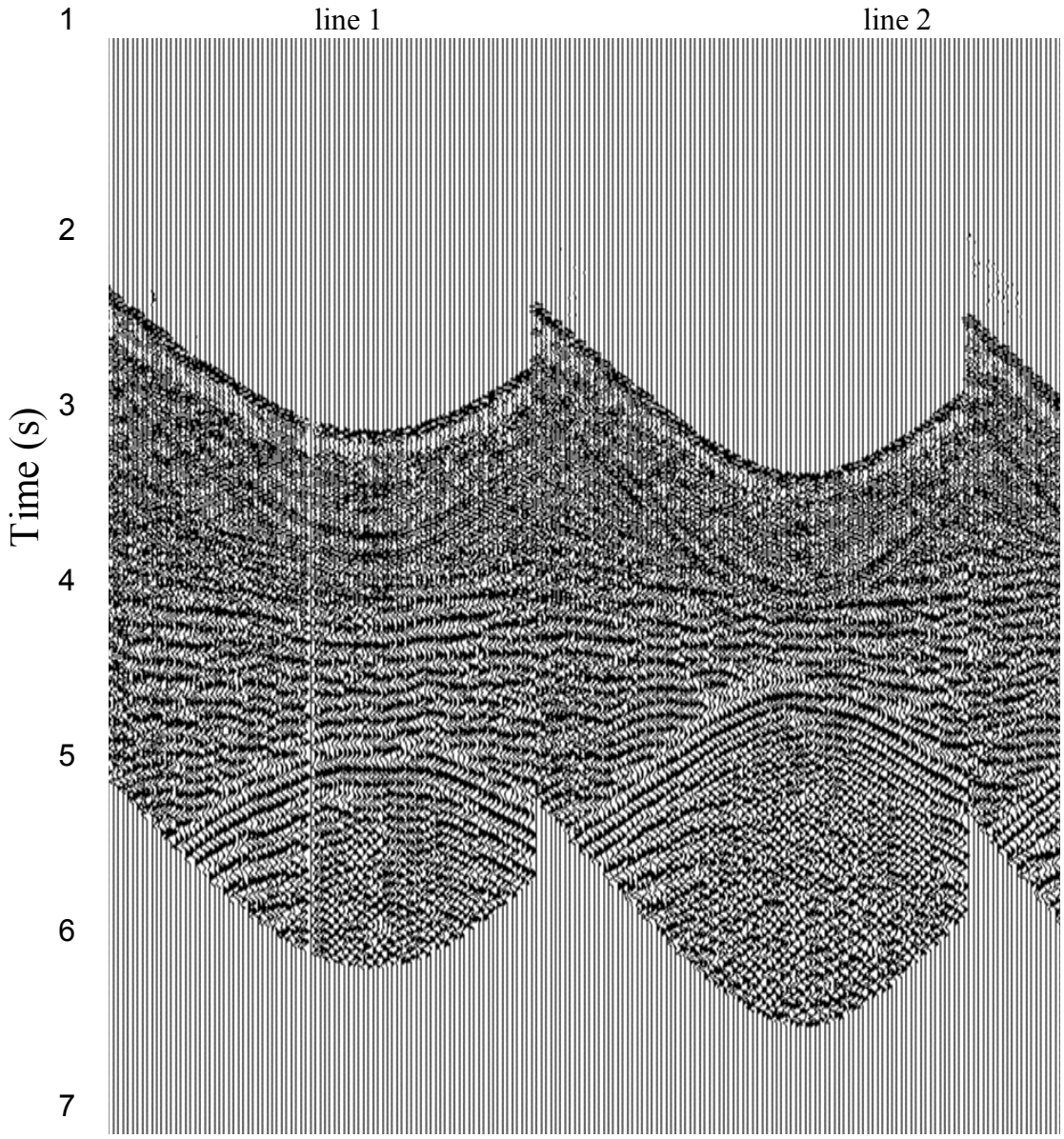
line 1
line 2
Time (s)
1
2
3
4
5
6
7

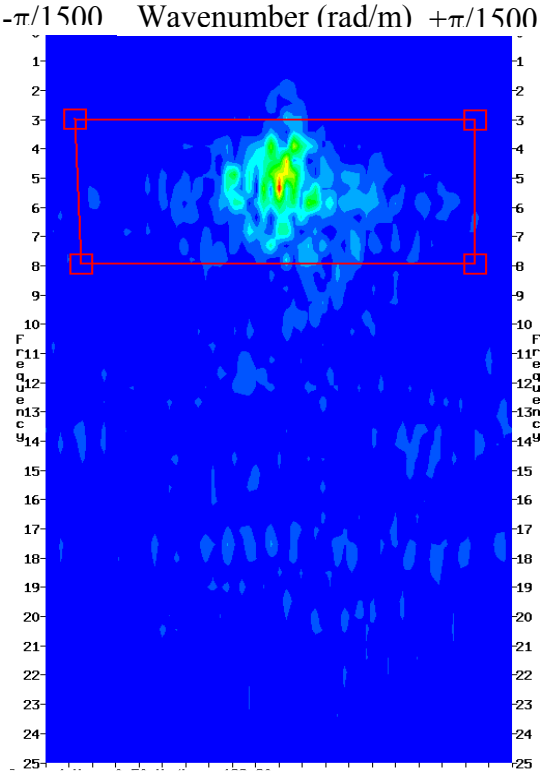

FIG. 4.8 FK spectrum of the flattened data shown in Figure 4.7.

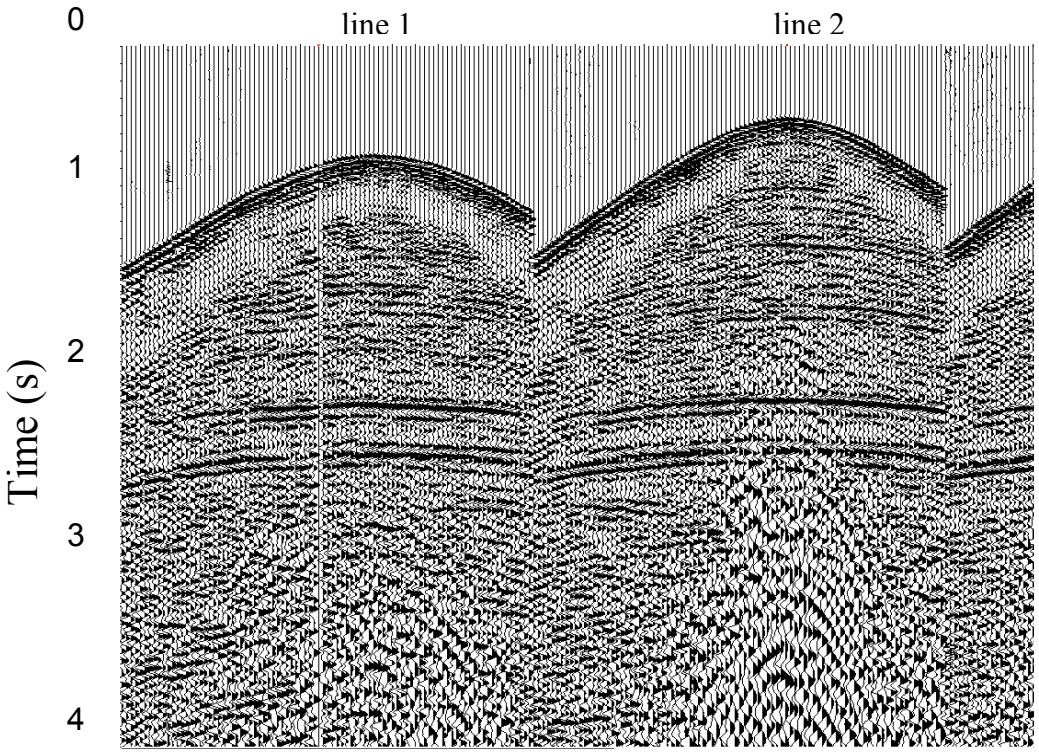

FIG. 4.9. Common shot gather of the vertical component shown in Figure 4.6 after removing both the 500 m/s and 300 m/s component of the ground roll.

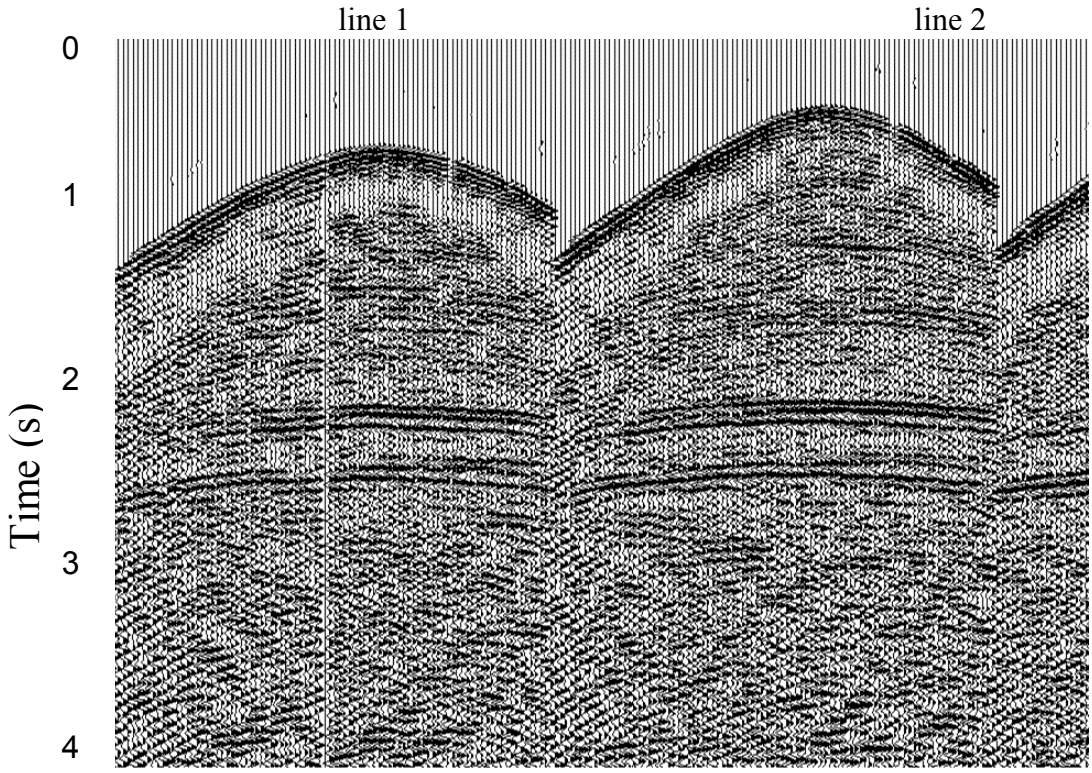

FIG. 4.10 Common l Shot gather of the vertical component after removing the 500m/s and 300m/s component of the ground roll and applying a (10,15,40,60) Hz band pass filter. These data will subsequently be input to subsequent statics and velocity analysis.

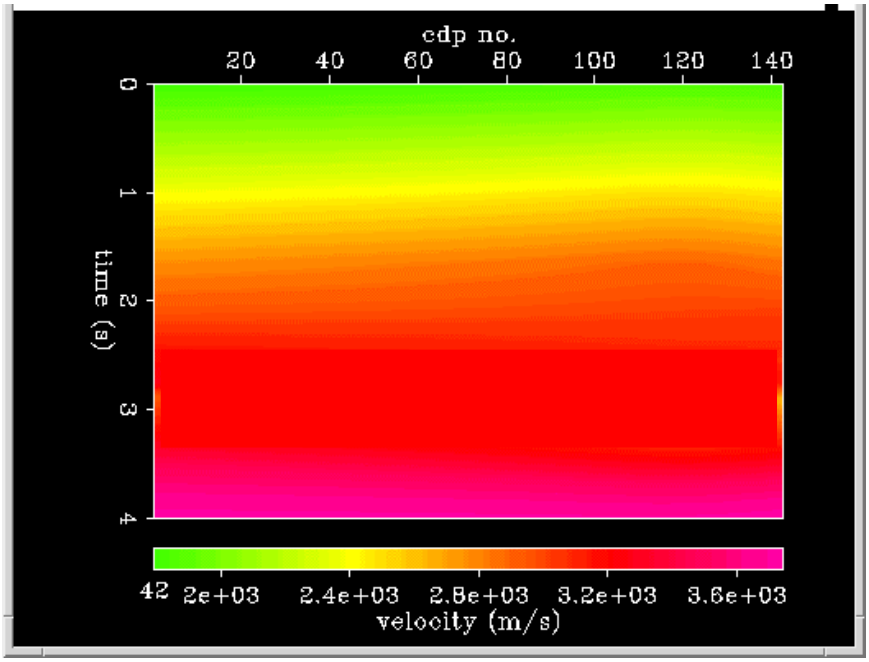

FIG. 4.12 Line number 59 of the pre-stack time migrated PP volume. Arrows indicate the reverse fault

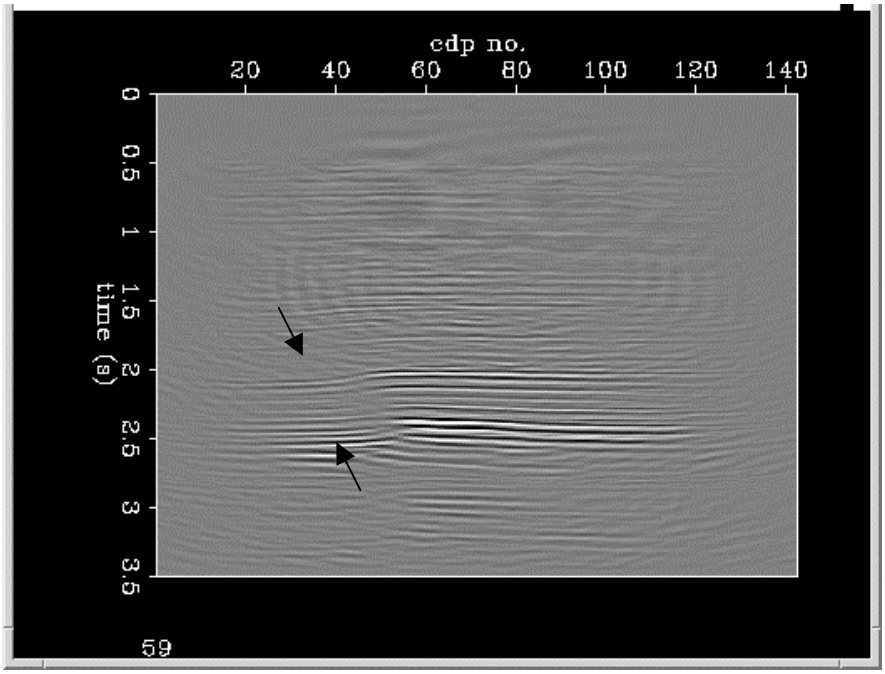

FIG. 4.11 Line 59 of the stacking velocity cube.

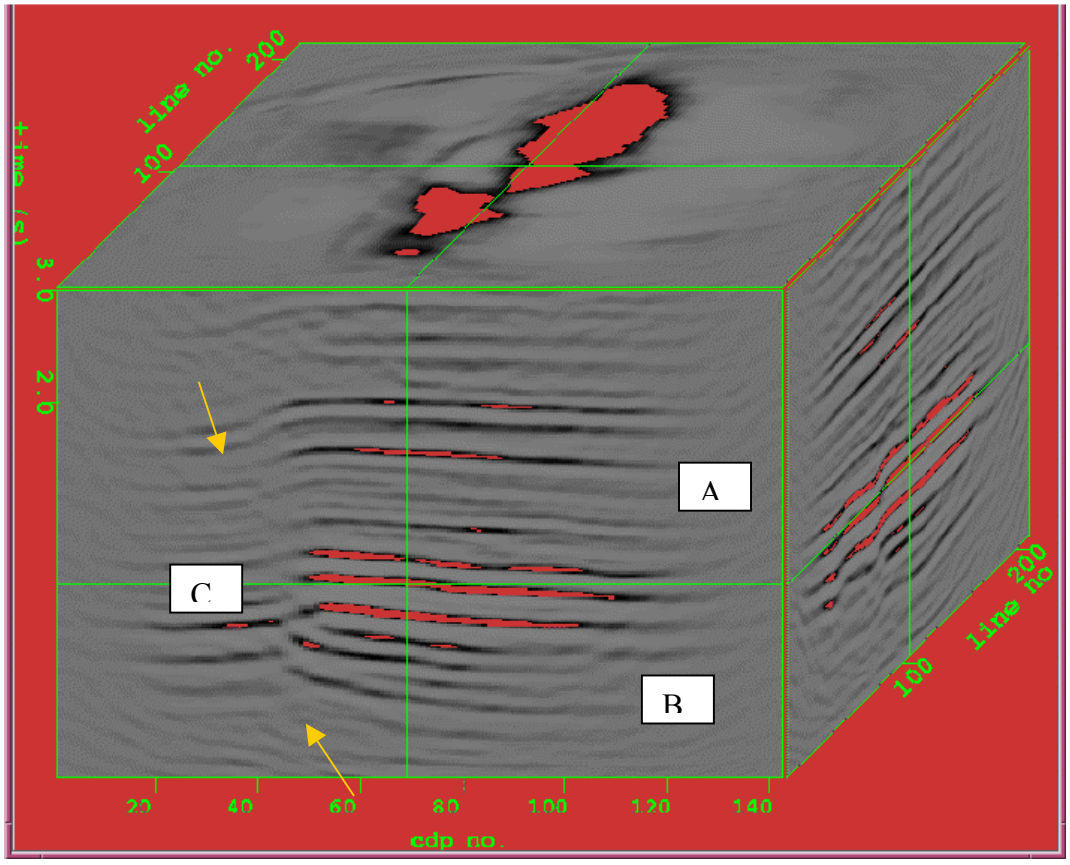

FIG. 4.13. 3D visualization of the pre-stack migrated cube zoomed at the area of interest. (A) corresponds to the strongest regional reflector which is the top of a shale formation Paguey, see Figure 3.2. (B) Corresponds to the location of bottom of the unit of the Escandalosa Formation. (C) Arrows indicate the location of the reverse fault.

Chapter 5: Processing of the seismic data (Horizontal Components)

In this chapter, we will develop a processing sequence for the horizontal components of the 3D3C data set. We will correct for polarization, apply asymptotic CCP binning, remove ground roll using modeling techniques, apply surface consistent gain, surface consistent deconvolution, residual statics, perform velocity analysis, generate a brute stack and run a post-stack time migration.

5.1 Rotation into transverse and radial component.

Since the area is structurally simple, the change in reflection polarity associated with source/receiver azimuths can be approximately handled by rotating the data into radial (defined to be within the source-receiver plane) and transverse (defined to be perpendicular to the source-receiver plane) components. For a 3-D geometry the horizontal channels of the geophone, H1 and H2, measure the north and east components of the shear waves over a range of source and receiver azimuths (Figure 5.1 and Figure 5.2). To separate the data into radial and transverse components, we apply a coordinate transformation to correct for polarity changes (Figure 5.3 and Figure 5.4). It is important to mention that the concept of radial and transverse component lose their sense in the presence of structure. If the reflection point is out of the source-receiver plane, working in the image point domain is more accurate. Since our data are structurally simple, we can safely use the concept of radial and transverse components.

We built a module in Seisup to perform this operation. Care must be taken in mapping the H1 and H2 axes, typically defined to be aligned with the receiver lines, and true North. This rotation produces a radial data set with most of the energy and a transverse data set with significantly coherent energy. The presence of first arrivals on the radial component and the absence of it on the transverse component serve to quality control our rotation. We will discuss separation into fast and slow components (S1 and S2) in Chapter 7.

5.2 Common conversion point gathers

Sorting PS reflection data into common conversion point (CCP) gathers for binning and stacking differs from sorting PP reflection data into common mid point gathers, due to the asymmetry of the up going and down going portions of the ray path. Because the area is structurally simple and the target of interest is deep, we are able to use the asymptotic binning. This approximation is valid for depths close to the maximum offset.

If we define a 27 m by 20 m bin size consistent with the 1/2 the inline (54 m) shot and (40 m) receiver separation used for the vertical component of the PP data, the CCP binning process produces an image with every fourth line on the stack having very low fold. However, if we assume a Vp/Vs ratio of 2.0, we can redefine our CCP bin size to be 2/3 of the 54 m by 40 m acquisition distances to obtain a 36 m by 27 m bin size, that results in the fold map shown in Figure 4.2b. While the new grid has fewer, more coarsely spaced lines than the vertical component grid, the fold is very even. This grid will be used to compute residual surface consistent statics.

5.3 Ground roll suppression

Ground roll suppression is often a challenge in conventional 3-D P-wave acquisition, and becomes even more difficult in 3-D converted wave (C-wave) acquisition. In addition to using single sensors arrays, converted wave frequencies and moveout are much closer than P-waves to those of the low frequency low velocity ground roll. Equally challenging, converted waves arrive significantly later than PP reflections, such that the ground roll noise cone masks reflections of greater offsets.

Conventional ground roll removal techniques are unable to remove the coherent noise without altering the amplitude of the reflectors on the horizontal components of C-waves. Rather, for our Borburata data, we have found that modeling the ground roll and then subtracting it from the data leads to the best preservation of C-waves signal. Model-driven filtering enhances the imaging of the deep reflectors without significantly altering

their amplitudes, therefore facilitating velocity analysis and improving the stacked results.

Ground roll, which consists of Rayleigh waves, air-coupled waves, and others guided waves propagating within the low velocity surface layers, contribute strong coherent noise in land seismic surveys (Al Husseini *et al*., 1981). Ground roll is characterized by low velocity, low frequency, dispersion and high amplitudes relative to the P-wave events of interest in land seismic surveys. Conventional PP data filtering techniques discriminate between ground roll and reflections of interest based on frequency, even though some methods have exploited wave train shape (Liu, 1999) depth of propagation (McMechan and Sun, 1991) and wavelet frame denoising (Abdul-Jauwad *et al*., 2000). Unfortunately, shear waves attenuate faster than P-waves of the same frequency such that the frequency content of deep reflections of C-waves is comparable to that of the ground roll.

As seen in Figure 5.3 and Figure 5.4, the data quality of the horizontal components is not as high as for the vertical component data set. These three lines from a common shot gather show very strong ground roll that masks almost all the later arriving reflectors. As in the vertical component data, the ground roll has two velocity components one at 500 m/s and another at 300 m/s. Continuity of the reflectors is good between 3.0 sec and 4.0 sec. The dominant frequency in this window is about 15 Hz (Figure 5.5). The frequency of the ground roll is very close to the frequency of the signal (Figure 5.6). Thus, when looking at the FK spectrum (Figure 5.5), it is difficult to design a filter to remove the noise without damaging the signal.

Since FK filtering was not appropriate; we evaluated median filters and other model-driven approaches to the data. Examining the ground roll has moveout, we flattened the ground roll at each of the two velocity components, applied the median filter, unflatened and then subtracted the result from the original data. This procedure is commonly used in VSP processing to separate the down- going events from up-going events. While the median filter improved the signal to noise ratio, we found the following correlation-based workflow to be particularly effective to suppress the ground roll

1. Design and apply outer and inner mutes that constrain the coherent noise ground roll. (The inner mute is applied because there is no coherent noise in the inner part of the ground roll cone).

2. Flatten the ground roll applying a linear moveout correction at a certain velocity, based on the 3-D source receiver offset (Figure 5.7). After moveout correction, the radially traveling component of the ground roll is no longer aliased, while the C-wave signal is aliased and may appear incoherent.

3. Perform time variant signal enhancement by extracting the coherent signal along the dominant dip direction and then summing the signal with the original trace. The dominant dip direction is measured by finding the maximum coherency along a range of dips from neighboring traces at each sample. If the maximum coherency is less than a user specified threshold level, no signal will be extracted. After signal extraction, the coherency is measured between the signal and the original trace at each sample. The coherency is then used to calculate a weight to apply to the signal trace before summing with the original trace. In this manner the signal is modeled and the moveout correction removed. (See Figure 5.8).

4. Subtract the modeled coherent noise from the data.

We applied this method to the raw data shown in Figure 5.3, and obtain the result shown in Figure 5.9. The large amplitude and highly coherent ground roll is reduced, making it possible to observe more continuous reflectors that were previously masked. With the coherent noise suppressed, we next apply surface consistent gain and surface consistent deconvolution, in order to increase the frequency content of the reflector (Figure 5.10). The reflector signal is enhanced compared to the residual ground roll.

Finally, to remove the low frequency of the ground roll and the very high frequencies introduced by the deconvolution we apply a band pass filter 5-10-30-40 Hz (Figure 5.11). At this point almost all the coherent noise is eliminated. We interpret the remaining component of incoherent noise to be backscattered ground roll that did not fit

our radial propagation model. Figure 5.12 shows a zoom of an area from Figure 5.11 comparing the final result with the initial data.

Since the remaining component of the ground roll is incoherent noise, it will not significantly impact the velocity analysis or stacking resolution. Furthermore, since PS reflections have low amplitudes at nearly vertical incidence angles, we will apply an inner mute prior to the time migration in order to avoid the remaining coherent noise in the inner part of the ground roll cone.

5.4 Residual statics

The static solution for converted waves is partially solved because the source static solution from the vertical component PP reflections will be the same for PS reflections. The challenge lies in solving the receiver statics. When applying the residual statics obtained from the vertical component to the radial component, we identify pull-ups on the reflectors due to the receiver statics (Figure 5.13). To address this problem we:

1. Compute the relative static shift by cross correlating the current trace with a number of traces within a coordinate and offset range on the radial component with the P statics applied. The peak of the crosscorrelation function defines the relative static shift.

2. Apply statics using the source statics obtained from the vertical component and the receiver statics obtained from the method mentioned above. The result of this strategy is shown on Figure 5.14.

We now perform velocity analysis on this data and generate a brute stack (Figure 5.15). This image is very similar to the result of the vertical component. We note the presence of a reverse fault (indicated by arrows), as well as strong reflectors A and B correlated with those observed in the vertical component stack shown in Figure 4.13. We apply the same processing flow to the transverse component with the brute stack shown in Figure 5.16. The first strong reflector corresponds to the top of a thick shale formation while the following reflectors correspond to the carbonate reservoirs of interest. We can

observe strong energy on both the radial and transverse components, that when interpreted in the context of nearly flat reflectors, suggests the presence of anisotropy in the area.

5.5 Post-stack time migration

Herrenschmidt *et al*. (2001) present a wide range of techniques dedicated to processing converted waves Post stack time processing can be used for PS data in a conventional manner to provide interpretable results when lateral velocities are not too important. This technique can be improved with a pre-stack time approach in which velocity models are estimated iteratively after flattening the common image gathers for both PP and PS events.

The horizontal components do not show a strong lateral velocity variation due to the simple structure and geology of the area. Additionally, as observed in the vertical component, pre-stack migration provides an image of comparable quality image to that obtained by post time migration for our Borburata Field data. We therefore follow Harrison (1992), and migrate the data using post-stack time migration where we estimate the PS migration velocity from of zero offset of PS ray path geometry. Harrison's (1992) PS migration velocity is given by:

$$V_{mig} = 2\sqrt{\frac{\left(\sum_{i=1}^{n}\frac{\alpha_i^2\beta_i}{\alpha_i+\beta_i}\tau_i\right)\left(\sum_{i=1}^{n}\frac{\alpha_i\beta_i^2}{\alpha_i+\beta_i}\tau_i\right)}{t_o\sum_{i=1}^{n}\alpha_i\beta_i\tau_i}}, \qquad (5.1)$$

where α_i and β_i are the P-velocity and the S-velocity for the layer *i*, *n* is the number of layers, τ_i is the two way vertical travel time through the i^{th} layer and t_0 is the total two vertical travel time. The derivation of equation (5.1) is shown in Appendix 1.

Equation (5.1) is used to estimate the migration velocity using the interval compressional velocity, estimated from the vertical component data set, and the shear

interval velocity calculated from the radial component using Dix's formula for converted waves:

$$\beta_{i+1} = \frac{V_{i+1}^2 T_{i+1} - V_i^2 T_i}{\alpha_{i+1}(T_{i+1} - T_i)}, \tag{5.2}$$

where V_i is the PS RMS velocity obtained from the stacking velocities of the radial component, and T_i is the summation of τ_i up to the i^{th} layer. The migration velocity can be then used in a conventional post-stack migration code for P-waves, providing good images with conventional software.

We display an example of the post-stack migration on the radial component in Figure 5.17. It is important to mention that here we used all offset and full azimuths. In Chapter 7, where we address rotation analysis we will limit the azimuth and offsets before post-stack migration to generate separate data volumes. Nevertheless, we can observe in Figure 5.17 good continuity of the reflectors of interest, the presence of the reverse fault, and the appropriate location of the reflectors in PS time.

We follow the same procedure for the transverse component. Both these results will then be used for the birefringence analysis discussed in Chapter 7.

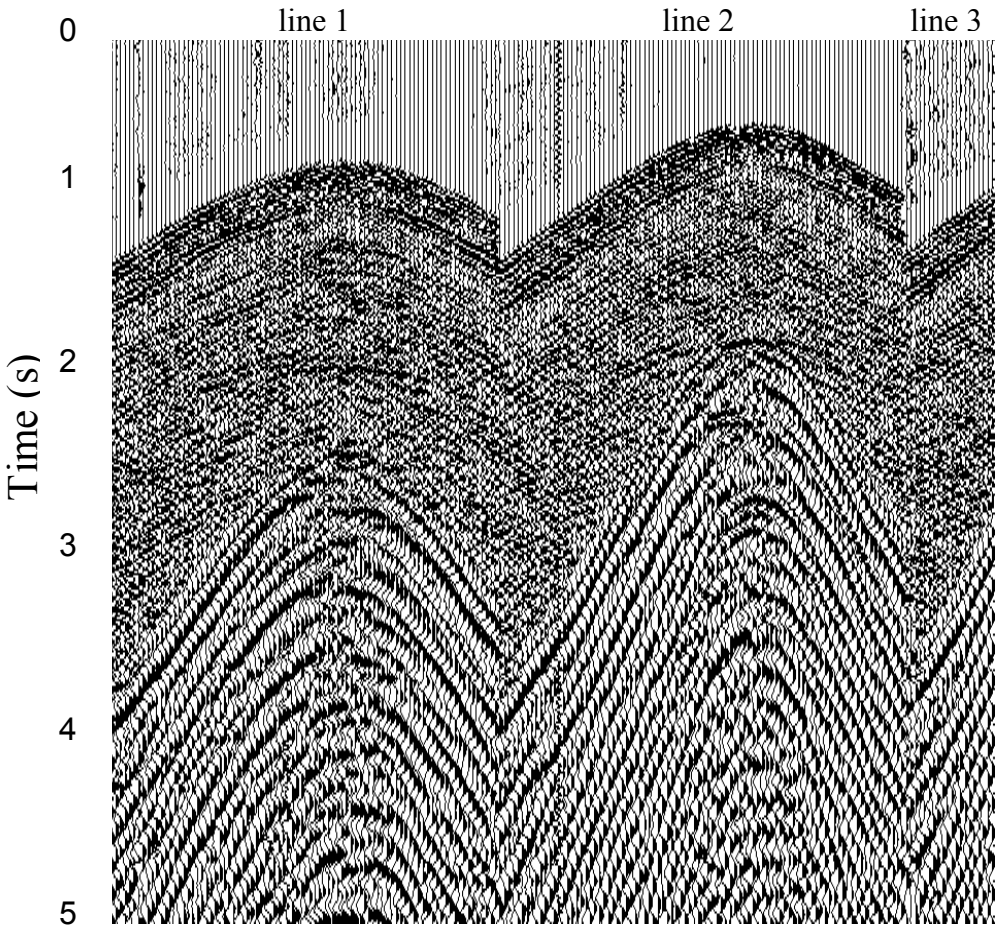

FIG. 5.1 Raw data of the H1 components, corresponding to the green shot location on Figure 4.2 and corresponding to the vertical component shown in Figure 4.6.

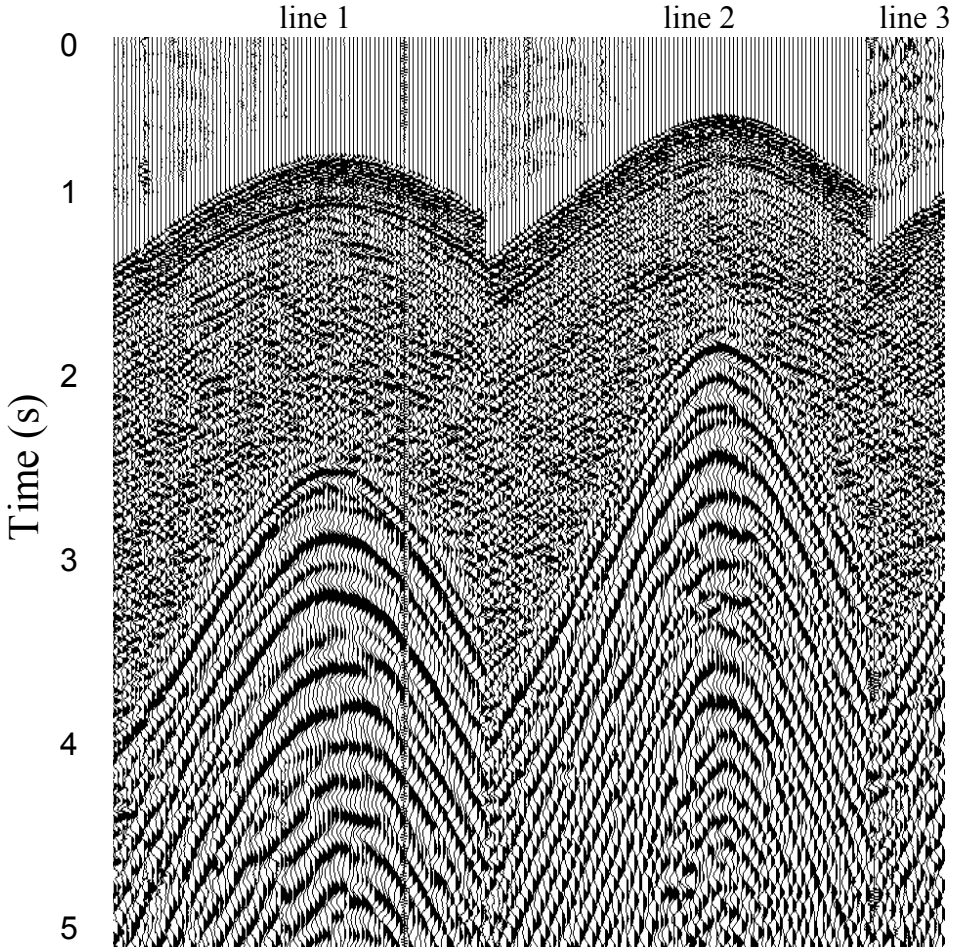

FIG. 5.2 Raw data of the H2 components, corresponding to the green shot location on Figure 4.2 and corresponding to the vertical component shown in Figure 4.6.

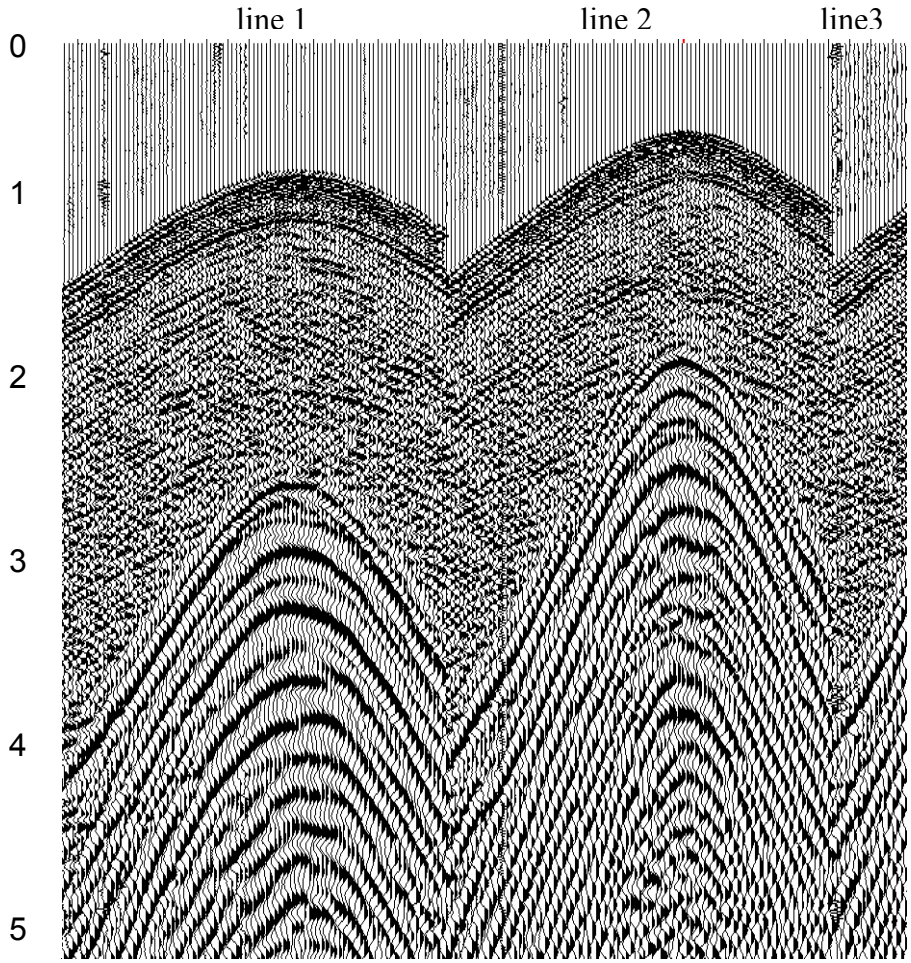

FIG. 5.3 Radial components shown in Figure 5.1 after correcting for polarization. Note that the ground roll noise cone has increased coherence.

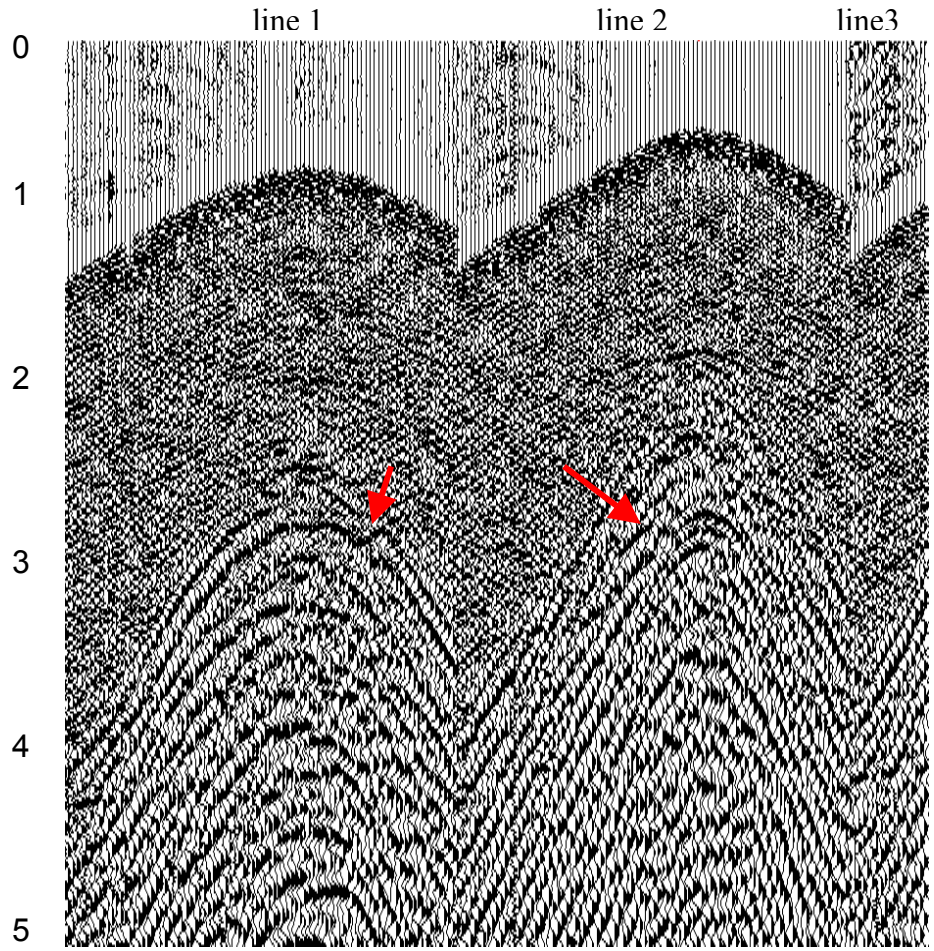

FIG. 5.4 Transverse components shown in Figure 5.2 after correcting for polarization. Note that the ground roll noise cone has less coherence, with indications of backscattering indicated by arrows. This backscattered energy will not be correctly modeled by the simple radial-moveout model.

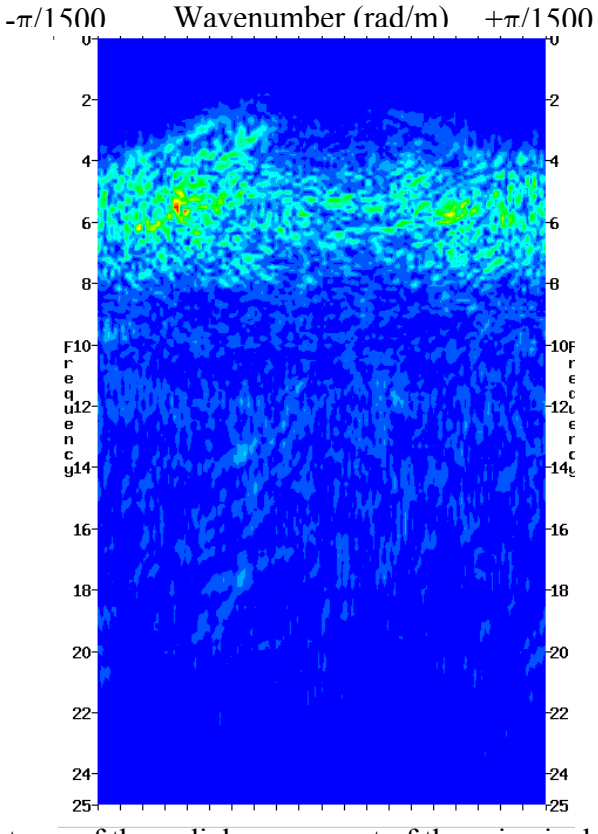

FIG. 5.5 FK spectrum of the radial component of the seismic data measured on receiver line 4 shown in Figure 5.3.

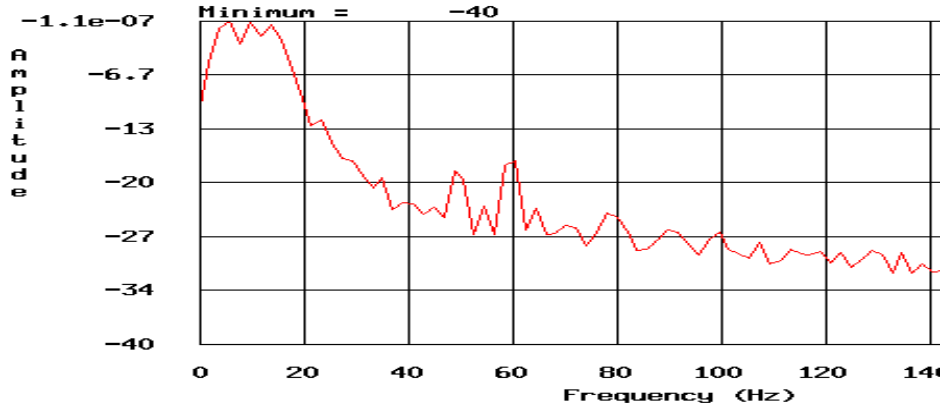

FIG. 5.6 Amplitude spectrum, from the radial component of the seismic data.

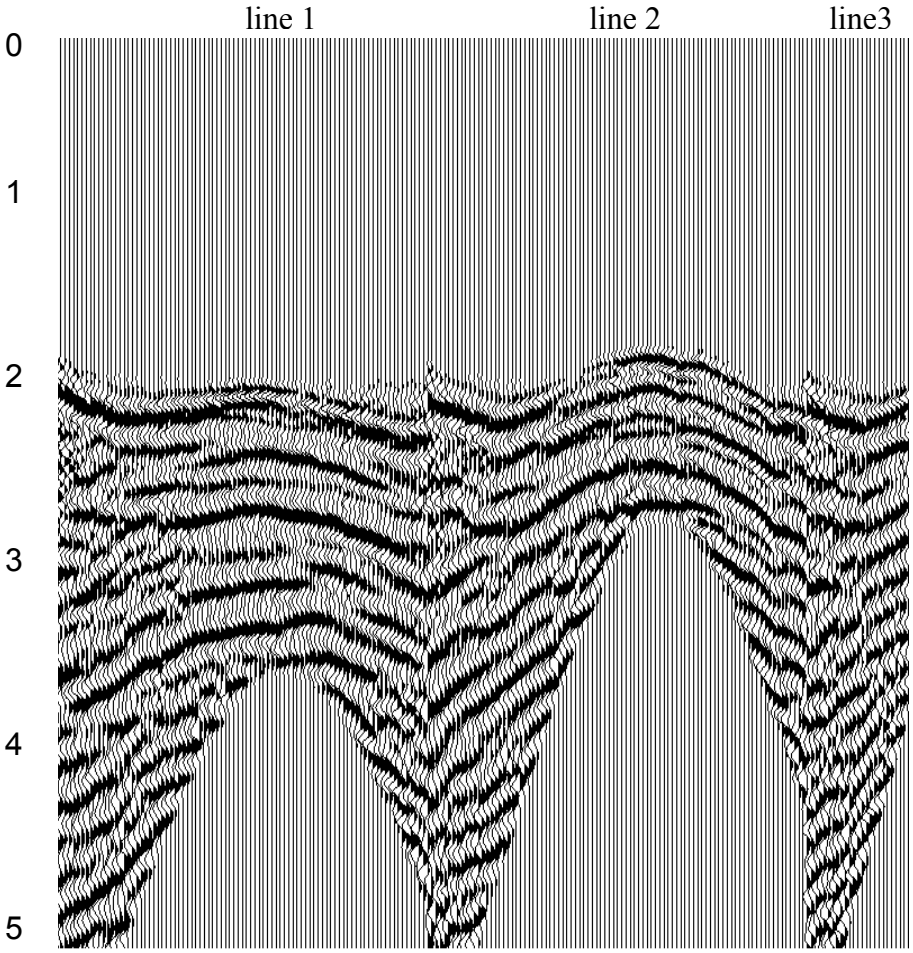

FIG. 5.7 Windowed ground roll from Figure 5.3 flattened at 800 m/s.

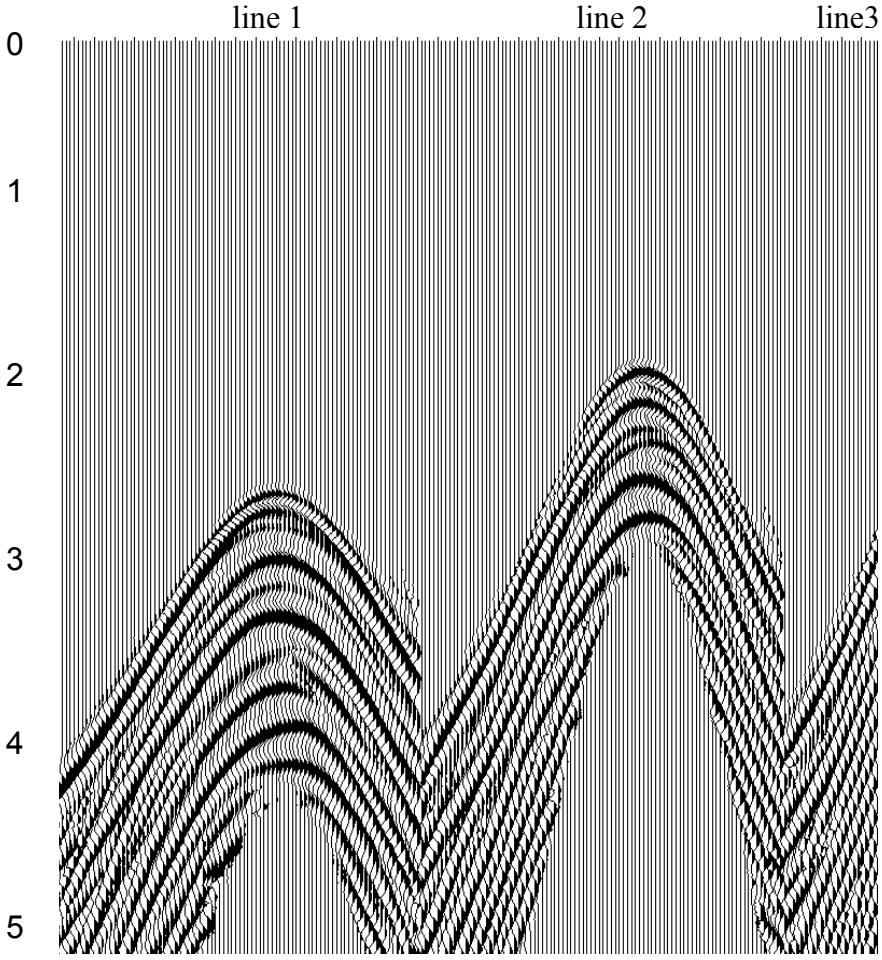

FIG. 5.8 Modeled ground roll corresponding to Figure 5.7 after unflattening. Note that backscattered ground roll has not been modeled.

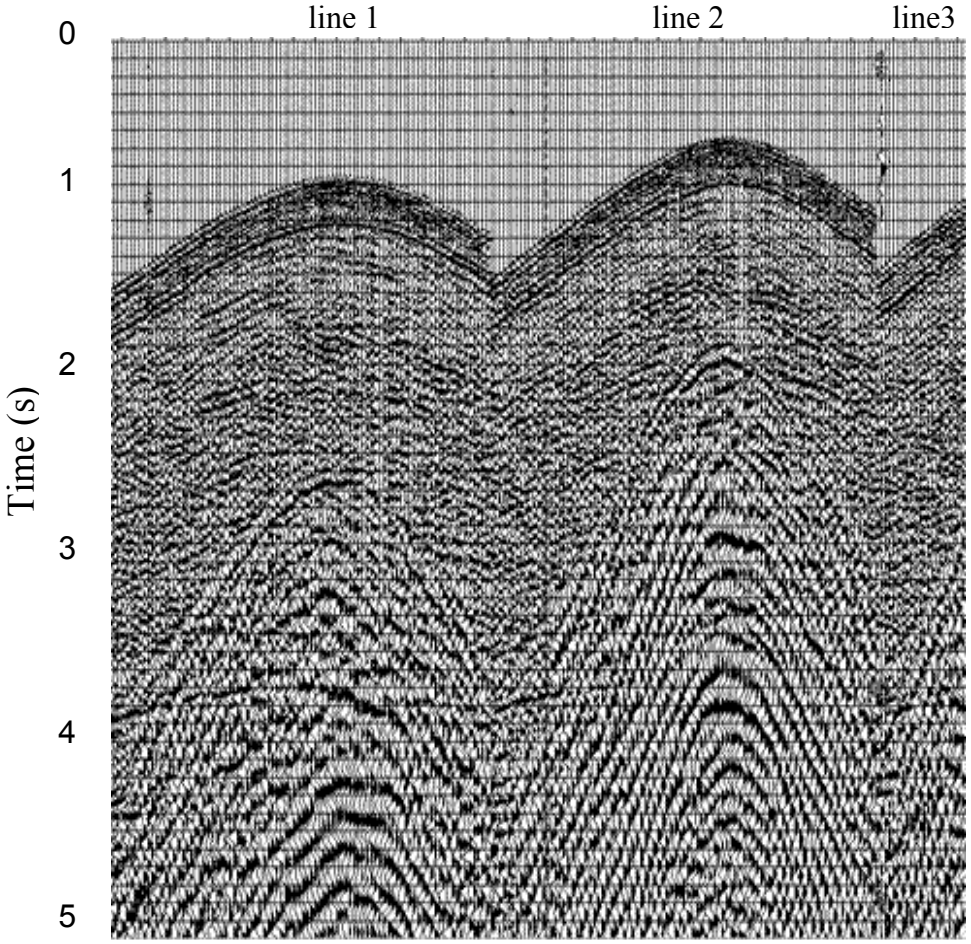

FIG. 5.9 Radial component of the shot gather shown in Figure 5.3 after subtracting the modeled ground roll shown in Figure 5.8.

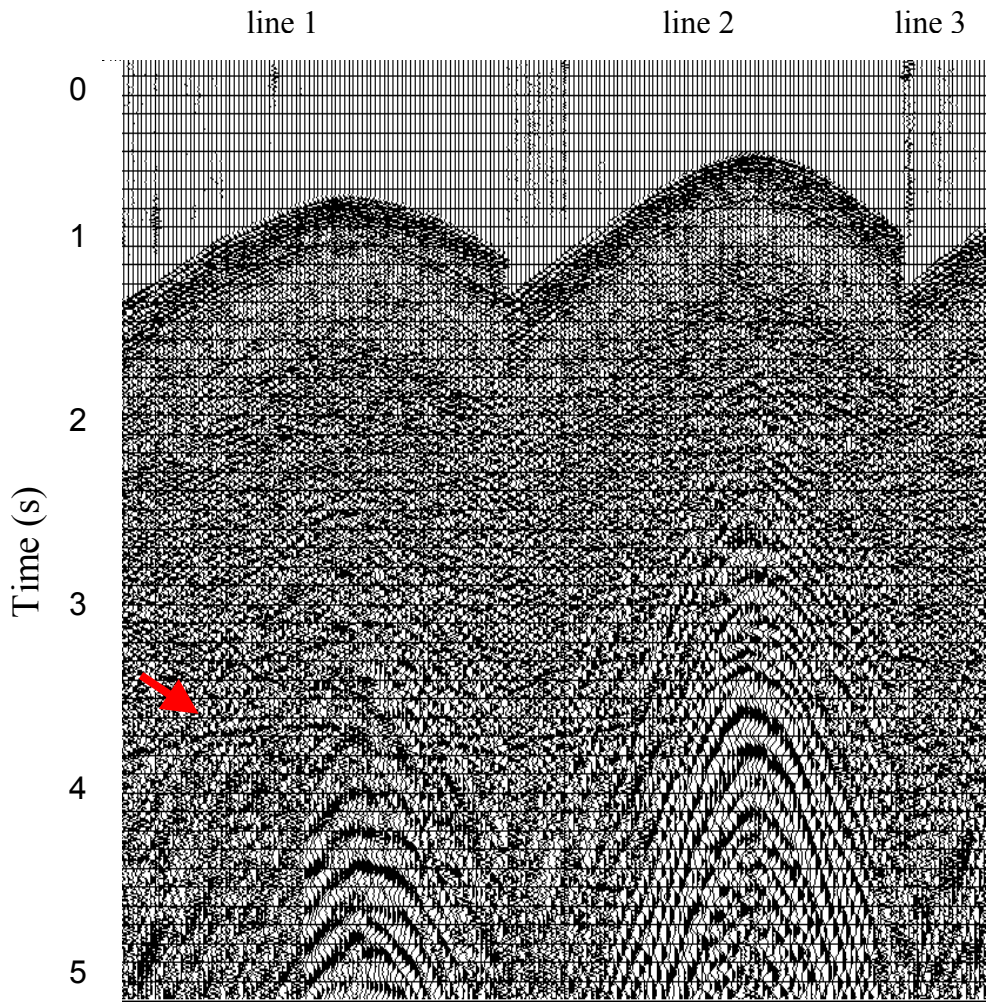

FIG. 5.10 Shot gather shown in Figure 5.9 after applying surface consistent gain, surface consistent deconvolution and datum statics. The red arrow indicates the presence of the reflectors.

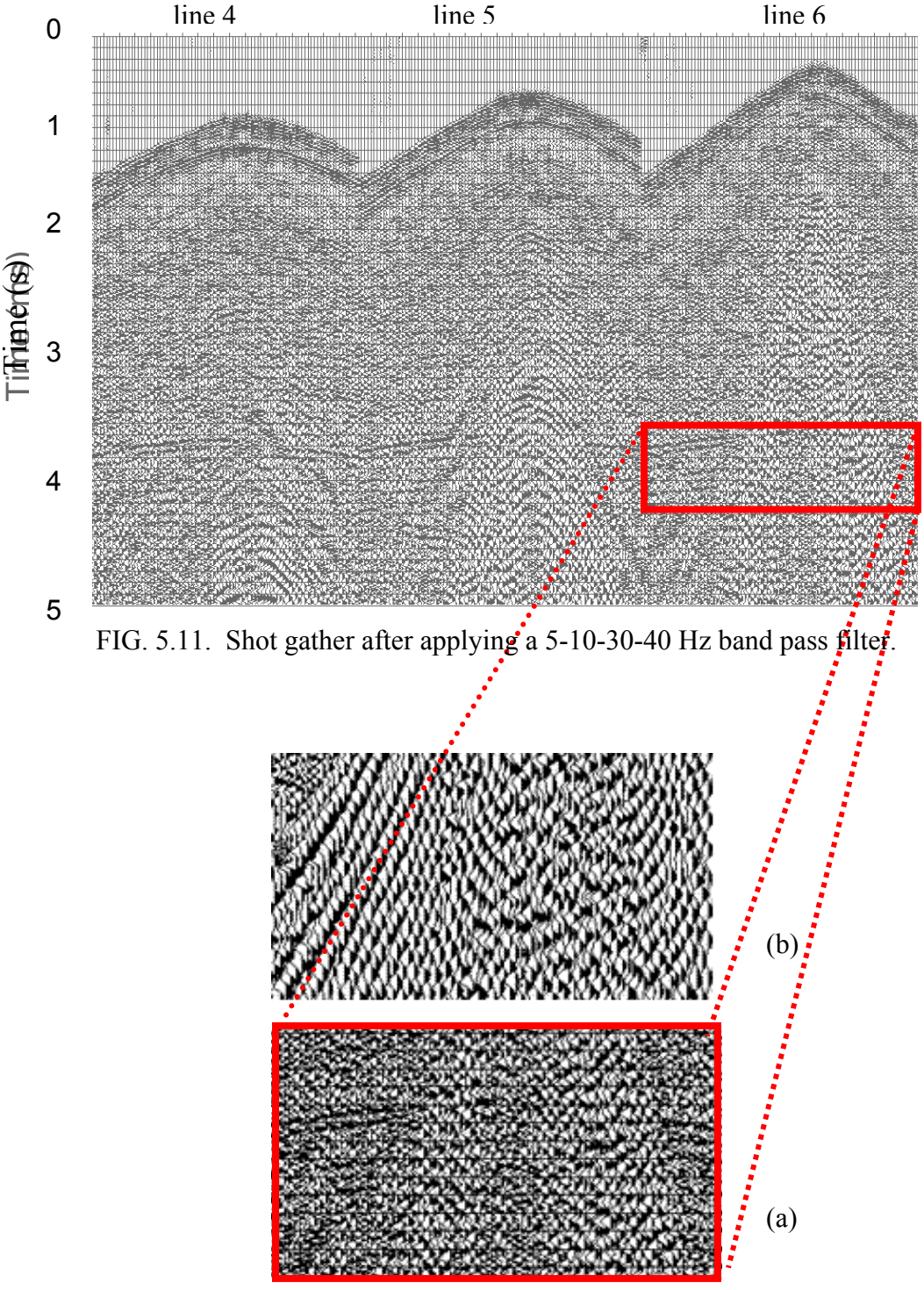

FIG. 5.11. Shot gather after applying a 5-10-30-40 Hz band pass filter.

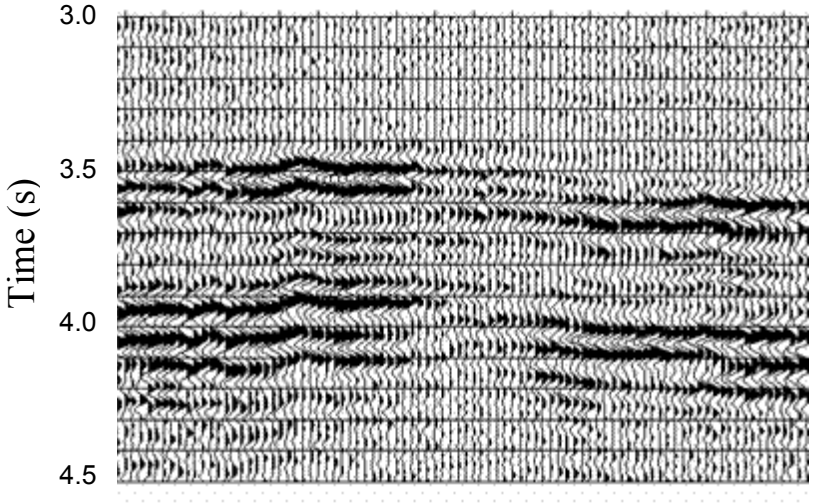

FIG. 5.13 Receiver stack after applying the residual statics estimated for PP reflector imaging using the vertical component.

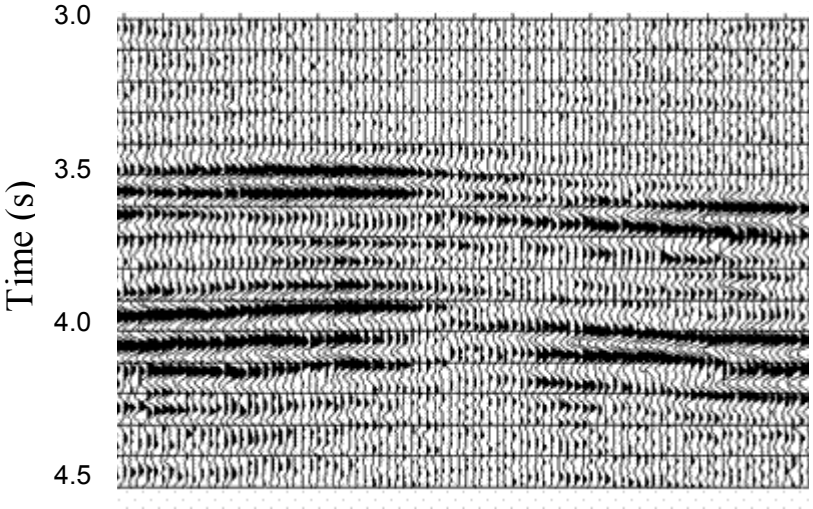

FIG. 5.14. Receiver stack after applying the receiver statics correction of the horizontal component to the data in Figure 5.13.

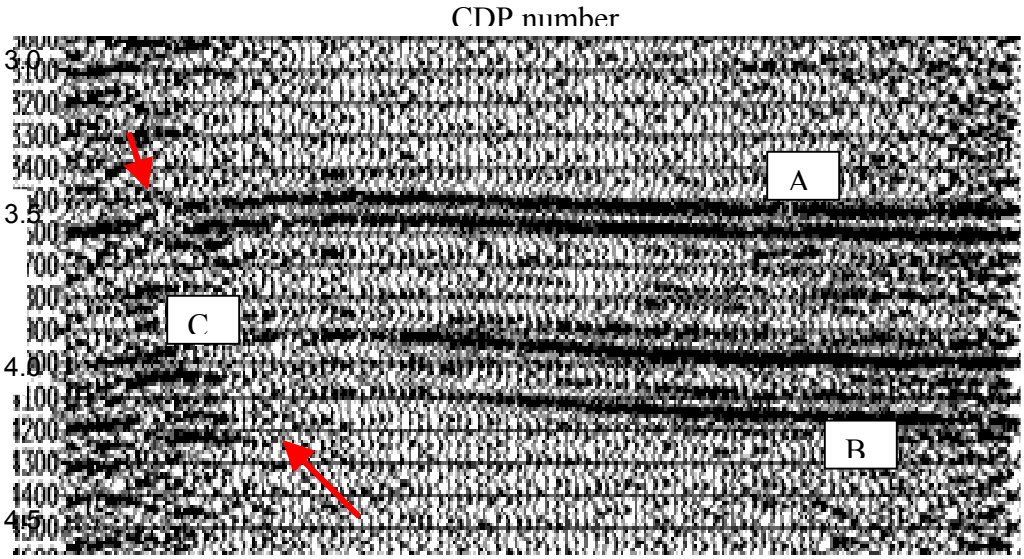

FIG. 5.15 Brute stack of the radial component. Arrows indicate the same reverse fault C, while A and B, indicate the same reflectors seen in the PP stack shown in Figure 4.13

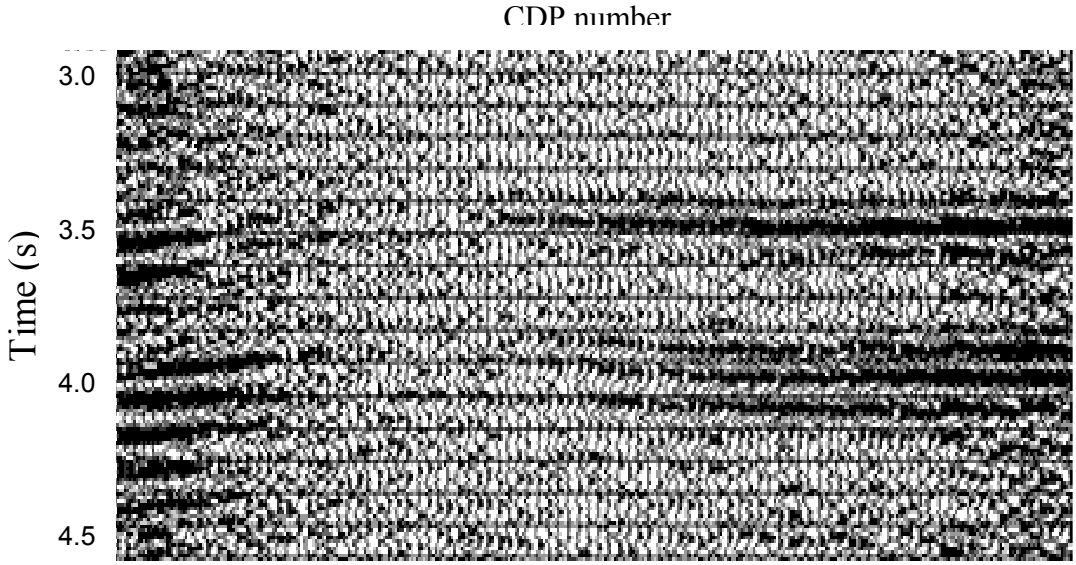

FIG. 5.16 Brute stack of the transverse component.

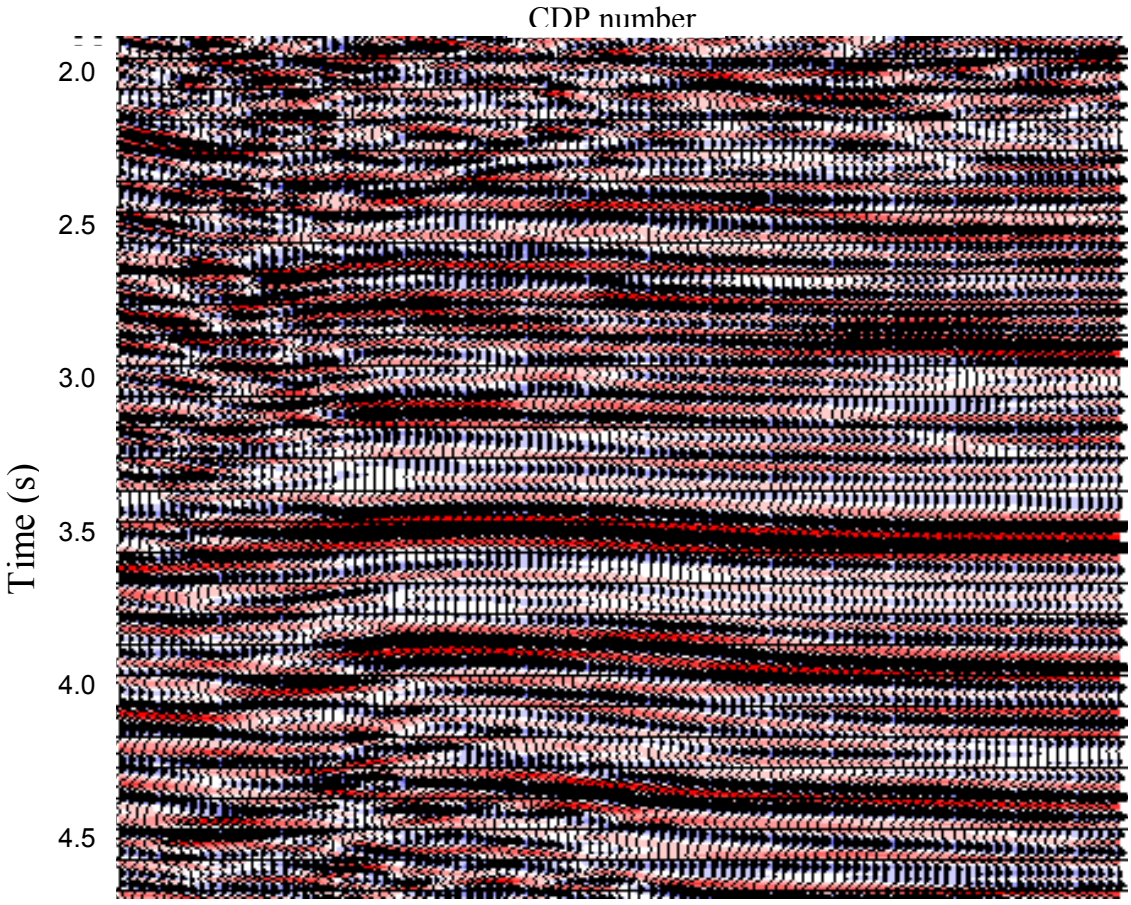

FIG. 5.17 Sample of post stack migration of the radial component containing all offsets and azimuth.

Chapter 6: Attribute analysis

In this chapter we will analyze our images in term of seismic geometric attributes, including principle component and semblance estimates of coherence and the derivatives of the principle component eigenvector in the North and East directions. We have generated these attributes for the vertical component (PP) data volume and radial and transverse (PS) data volumes. Since the two-way travel times for PP and PS reflections are significantly different, we present our results in terms of horizon slices along the Escandalosa event of interest. We will show that the PS volumes have greater lateral resolution than the corresponding PP volume.

6.1 Introduction

Taner (2000) defines "seismic attributes as all the information obtained from seismic data, either by direct measurements or by logical or experience based reasoning" Seismic attributes typically provide information relating to the amplitude, shape, and/or position of the seismic waveform. Taner (2000), Brown (2001) and others classify seismic attributes into five categories:

1. **Complex Trace Attributes,** derived from the analytic trace, containing both real and imaginary parts are broken into two subcategories:

- **Instantaneous Attributes**, associated with a point in time, including: envelope, instantaneous phase, instantaneous frequency, weighted average frequency, and apparent polarity, and

- **Response Attributes**, related to a lobe of the energy envelope e(t); and more closely corresponds to an event, rather than to a single time sample, including: response amplitude, response phase, response frequency, response length, skewness, and rise time.

2. **Fourier Attributes**, frequency domain attributes obtained through Fourier analysis (including amplitude variation with bandwidth in frequency (AVBF), and spectral decomposition).

3. **Time Attributes**, related to the vertical position of the waveform in the seismic section (including horizon time picks and isochrons).

4. **Windowed Attributes**, attributes which summarize information from a vertical window of data, including: maximum absolute amplitude, time of maximum absolute amplitude, average absolute amplitude, sum of absolute amplitudes, average instantaneous frequency, number of zero crossings, largest peak/trough amplitude difference, largest peak/trough time difference.

5. **Multi-trace (also called geometric) Attributes**, attributes calculated using more than one input seismic trace, which provide quantitative information about lateral variations in the seismic data (including coherence, dip/azimuth, and amplitude gradients).

In this chapter we will focus on multitrace (or geometric) attributes. Seismic coherence is a measure of the trace-to-trace similarity of the seismic waveform within a small analysis window, allowing us to map faults, fractures and lateral stratigraphic discontinuities (Bahorich and Farmer, 1995). The coherence results shown in this work are obtained from semblance and principle component estimates.

Semblance (Marfurt *et al*., 1998) is a measure of the coherence of seismic data from multiple channels, that is equal to the energy of the stacked trace divided by the energy of all the traces that make up the stack. If data from all channels have the exact same amplitude and waveform, the semblance has a value of unity.

Principle component analysis (Gersztenkorn and Marfurt, 1999) involves a mathematical procedure that transforms a number of (possibly) correlated vectors into a (smaller) number of uncorrelated eigenvectors (also called *principle components)*. The first principle component accounts for as much of the variability in the data as possible,

with each succeeding component accounting for as much of the remaining variability as possible. Principle components are obtained by projecting the data vectors on the space spanned by the eigenvectors. To obtain these principle components, we first form a square, Hermitian symmetric, covariance matrix by cross correlating each data vector with itself and with all other data vectors within the analysis window. We then use standard mathematical algorithms to decompose the matrix into a system of eigenvectors and eigenvalues. The eigenvector associated with the largest eigenvalue has the same direction as the first principle component. The eigenvector associated with the second largest eigenvalue determines the direction of the second principle component. The maximum number of eigenvectors equals the number traces used to generate the covariance matrix. The sum of all the eigenvalues equals the mathematical trace (sum of the diagonal) of the covariance matrix.

We define the principle component estimate of coherence to be the ratio between the first eigenvalues and the sum of all eigenvalues. If data from all channels have the exact same waveform (but possibly different amplitude) the principle component estimate of coherence has a value of unity.

6.2 Geometric attributes applied to the PP volume

We now calculate geometric attributes and extract them along the top of the Escandalosa formation. Figure 6.1a shows a horizon slice of the principle component coherence cube estimated on the PP volume. The main NS fault indicated by the blue arrows, and shown previously in Figure 4.13 is easily identified and appears to splay into a set of parallel faults to the North. We also identify another fault system that is NE-SW indicated by the green arrows. Figure 6.1b shows the semblance coherence at the same time slice. The patterns are similar, but of lower resolution than those shown in Figure 6.1a. Since we used a nine traces analysis window, the eigenvector is directly related to the spatial variation of the most coherent part of the seismic amplitudes. In Figures 6.1c and d, we plot the north and east gradient of the principle component eigenvector, and observe that the east gradient of the eigenvectors enhances the NS features and shows a

complementary display of the incoherent events observed in principle component and semblance coherence volumes. Here it is possible to identify some SE-NW lineations, which form a conjugate system to the previously identified NE-SW lineations. There are some clear lineations oriented in the NS direction associated with acquisition footprints. On Figure 6.1d we display the North gradient of the eigenvector which enhances lateral resolution of features in the EW direction, showing the presence of faults running parallel to the main NS fault. The EW lineations are acquisition footprints.

In Figure 6.2, we display a time structure map of the Escandalosa horizon previously generated by colleagues at PDVSA-Intevep from a larger, conventional PP survey. Blue colors indicate shallow structure and red colors indicate deep structure. The NS reverse fault and NE-SW trend is clearly indicated on both the time structure map and the attribute volumes. However, the lineations running parallel to the main NS fault system have not been mapped on the time structure map in Figure 6.2.

6.3 Geometric attributes applied to the PS volumes

In this section we repeat the analysis done for the vertical component PP wave reflection volume to the radial component PS reflection volume. We will begin with a cube containing all azimuths and offsets. Later, we will limit ourselves to far offsets and a suite of azimuths. In Figure 6.3, we display horizon extractions along the Escandolosa Formation of the same attributes shown in Figure 6.1 generated from the radial component of the PS data volume for full azimuth and offset. When comparing Figure 6.3 to Figure 6.1 we observe that the PS reflections are able to identify parallel faults at the southern end of the main NS fault that were not imaged by PP reflections.

As we observed on the PP data, we also observe that the gradient of the eigenvector (Figures 6.3c and d) attribute gives a considerably more detailed image of the features than the coherence attributes. The reason for this is geological rather than

mathematical, the lateral variation in reflectivity gives rise to subtle changes in amplitude but little to no change in waveform.

While in general the PS attributes exhibit greater lateral resolution than the PP attributes, we have not illuminated the NE-SW trend seen on the PP data. The reason for this difference could be either differences in P and S wave reflectivity, or in the angles of illumination. We also note that the results obtained with the radial component seem to be less susceptible to acquisition footprint. Finally, we notice the presence of a NS lineation in the middle of the PS coherence attribute extractions (CDP 60) that is not present in the in the PP data.

Careful examination of Figure 7.6 shows that this lineation (Figure 6.3c) can be explained as a pinchout. We will discuss this feature in more detail in Chapter 7. Although in general, shear waves are attenuated faster than P waves, at Borburata, the highest frequency of the PS data is comparable to that of the PP. Given that the S wave velocity is roughly 1/2 that of the P wave data, we can conclude that our PS volume has higher vertical resolution than the corresponding PP volume, thereby allowing us to observe greater detail.

A difference in the bandwidth is another possible cause that generates converted waves to have better lateral resolution than compressional waves. Figure 6.4a shows a time window extracted from the vertical component before processing. We plot its frequency spectrum in Figure 6.4b. On the same receiver line, we selected a time window from the radial component (Figure 6.4c). We plot its frequency spectrum in Figure 6.4d. When analyzing the frequency spectrum the bandwidth for the vertical component is approximately 1.1 octaves and the bandwidth for the radial component is approximately 1.8 octaves. Hence the frequency bandwidth, and therefore time resolution, is greater for converted waves than for the PP waves. Figure 6.3 was generated from a PS volume containing all azimuths and offsets. We can also evaluate geometric attributes on azimuthally restricted volumes so that geologic features, especially those imaged with that particular azimuth, are more readily revealed.

Because the ray path of PS reflections is asymmetric, ray paths can image different areas in the subsurface when considering positive or negative offset (flipping source and receiver location). Therefore when stacking the traces for a given bin we could have imaged different points in the subsurface. This problem is not so severe in the area of work because it is quite flat. Nevertheless, to avoid any possible smearing of the data we decided to separate positive and negative offsets. The importance of sorting the data will be fully discussed in Chapter 7.

In Figures 6.5, 6.6 and 6.7, we display attributes corresponding to those displayed in Figure 6.3, generated from range and azimuth limited volumes. All three figures have azimuths limited between+15° to -15° measured from North. Figure 6.5 corresponds to a data volume containing both positive and negative far offsets, while Figures 6.6 and 6.7 correspond to data volumes containing only positive far offset and negative far offset respectively. The horizon slices through the positive offset attributes will have better coverage in the north area of the map while the horizon slices through the negative offset will have better coverage in the south area of the map. Thus, the vertical features at the north of Figure 6.7 should be interpreted as artifacts due to low fold). For this reason, we trust the image with positive offset, which shows the parallel faults in the North part of the Figure 6.6c. We do not have further information that can corroborate this result, but this can be interpreted as the previous existence of a NS fault that after the rise of the Andes, producing a NE-SW trend, parallel to the Andes, breaking the continuity of the NS fault and generating a set of parallel faults that can be seen in the north part of the maps. We also observe that the EW faults located at the east side of the main NS fault can be seen on the positive offset (Figure 6.6a) data while other features can be seen in the negative offset data (Figure 6.7a).

As a PS reflection workflow, we recommend restricting the data by different azimuths and for both positive and negative far offsets.

6.4 Conclusions

Geometric attributes such as coherence can be run on azimuthally and offset-restricted volumes to enhance the appearance of geologic features. Separately analyzing positive and negative offsets produces more detailed coherence images. The simplest explanation is that since the travel paths are asymmetric, our susceptibility to errors in velocity and subsequent smearing of the resulting images, is increased. In spite of the coarser bin size, PS reflections give improved lateral resolution in coherence images in comparison with PP-reflections. The reason for this is due to a surprisingly broader recorded bandwidth for the PS waves, coupled with the lower S velocities and shorter wavelengths at any given frequency. We interpret the set of NE-trending parallel faults observed in the PS coherence at the north end of the NS main fault to be a consequence of compressive stresses associated with the rising of the Andes.

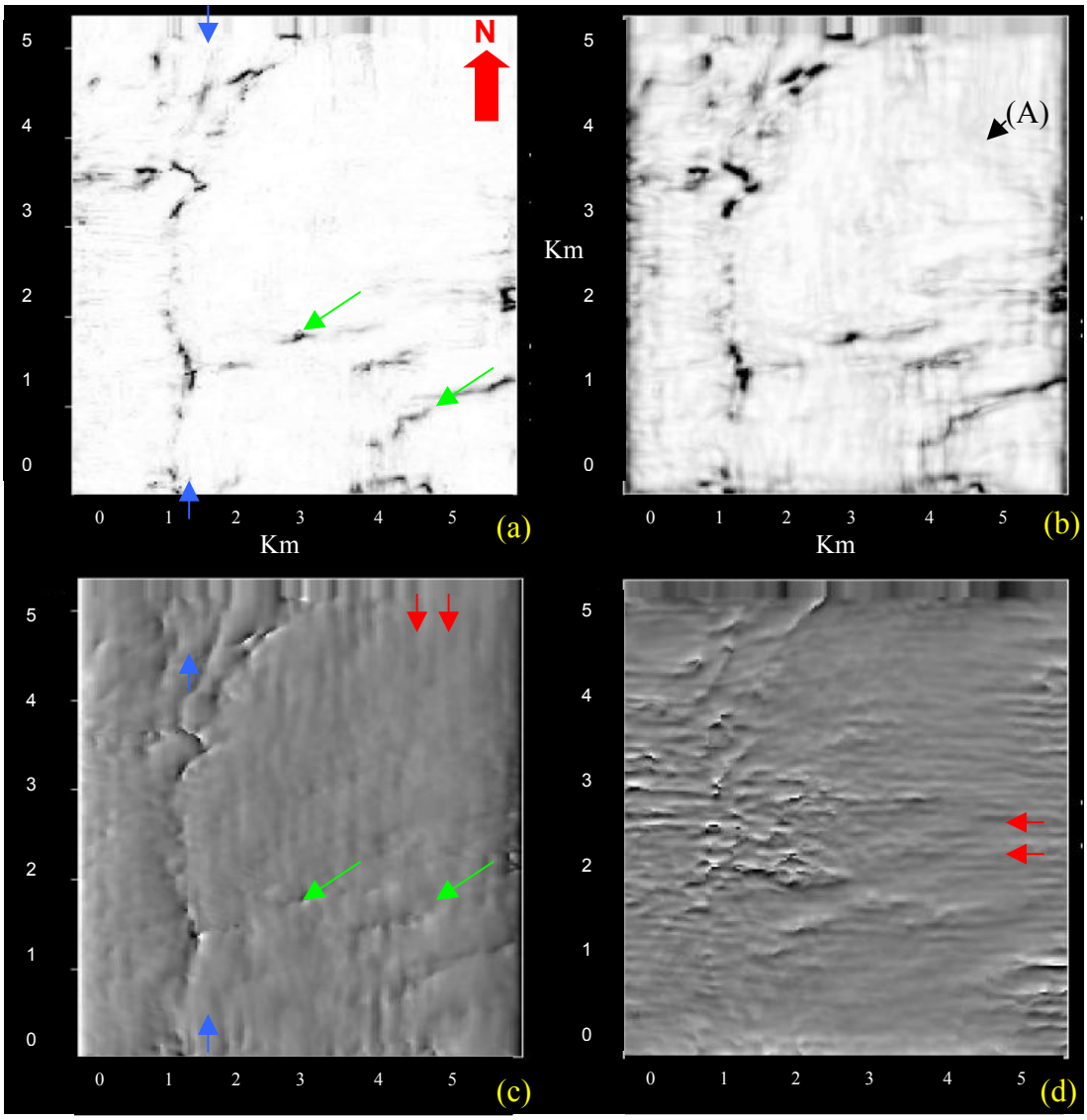

FIG. 6.1 Horizon slices of different attributes along the Escandalosa calculated from the PP (vertical component) data volume: (a) Principle Component Coherence. (b) Semblance Coherence (c) East gradient of the principle component eigenvector. (d) North gradient of principle component eigenvector. Red arrows indicate acquistion footprints. Blue arrows indicate the reverse fault shown in Figure 4.13.

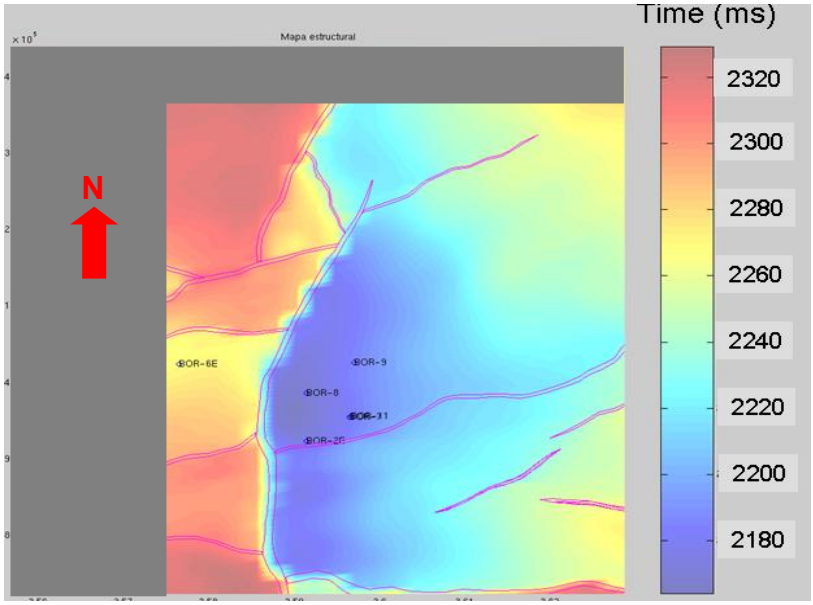

FIG. 6.2 Time/structure map of the top of the Escandalosa formation, showing an interpretation of the fault system done by PDVSA-Intevep from a larger, conventional 3-D survey.

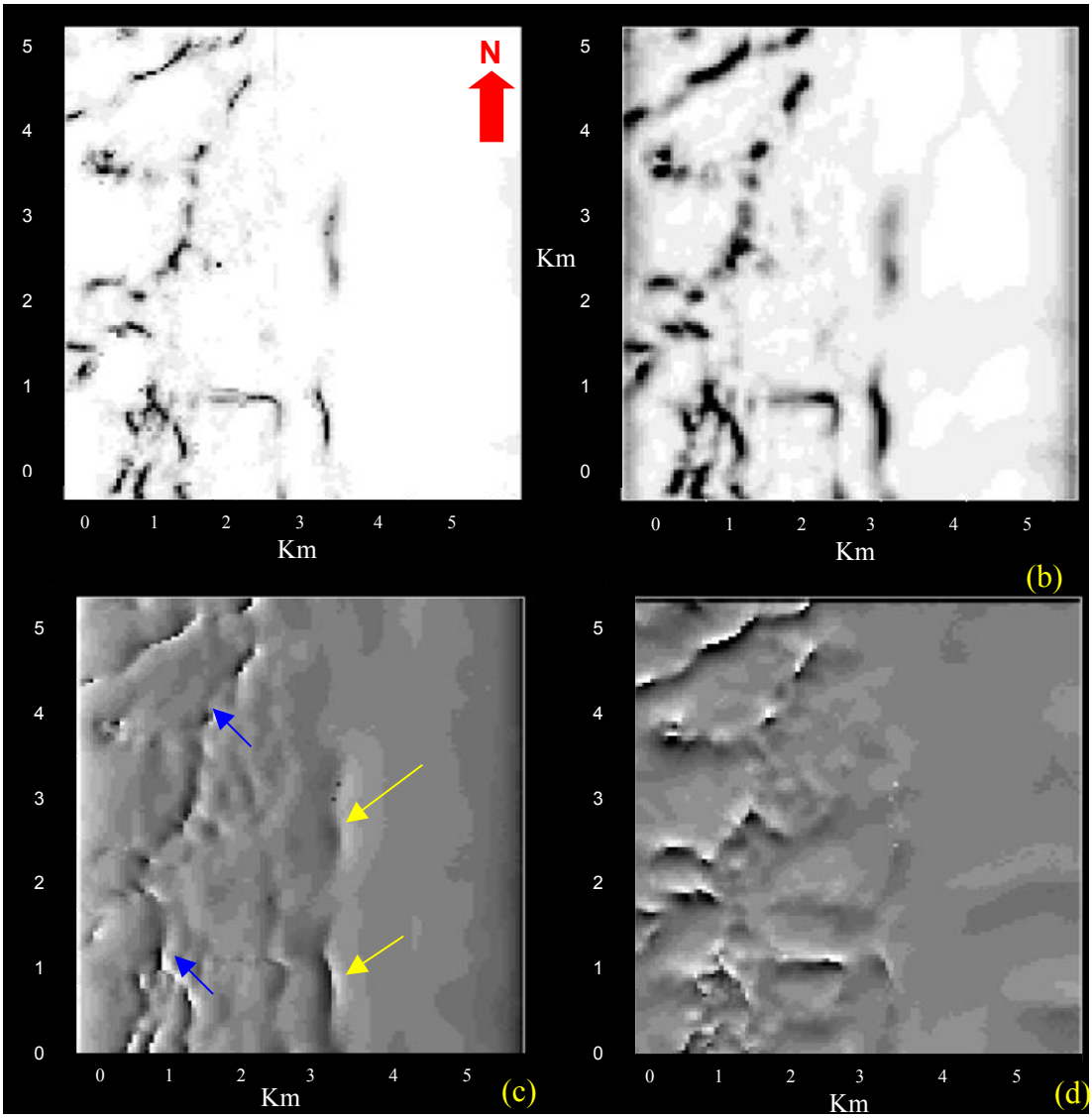

FIG. 6.3 Horizon slices of different attributes along the Escandalosa calculated from all azimuths and offsets of the PS (radial component) data volume: (a) Principle Component Coherence. (b) Semblance Coherence (c) East gradient of the principle component eigenvector. (d) North gradient of principle component eigenvector. Blue arrows indicate the reverse fault shown in Figure 4.12. Yellow arrows indicate the pinchout shown in Figure 7.7

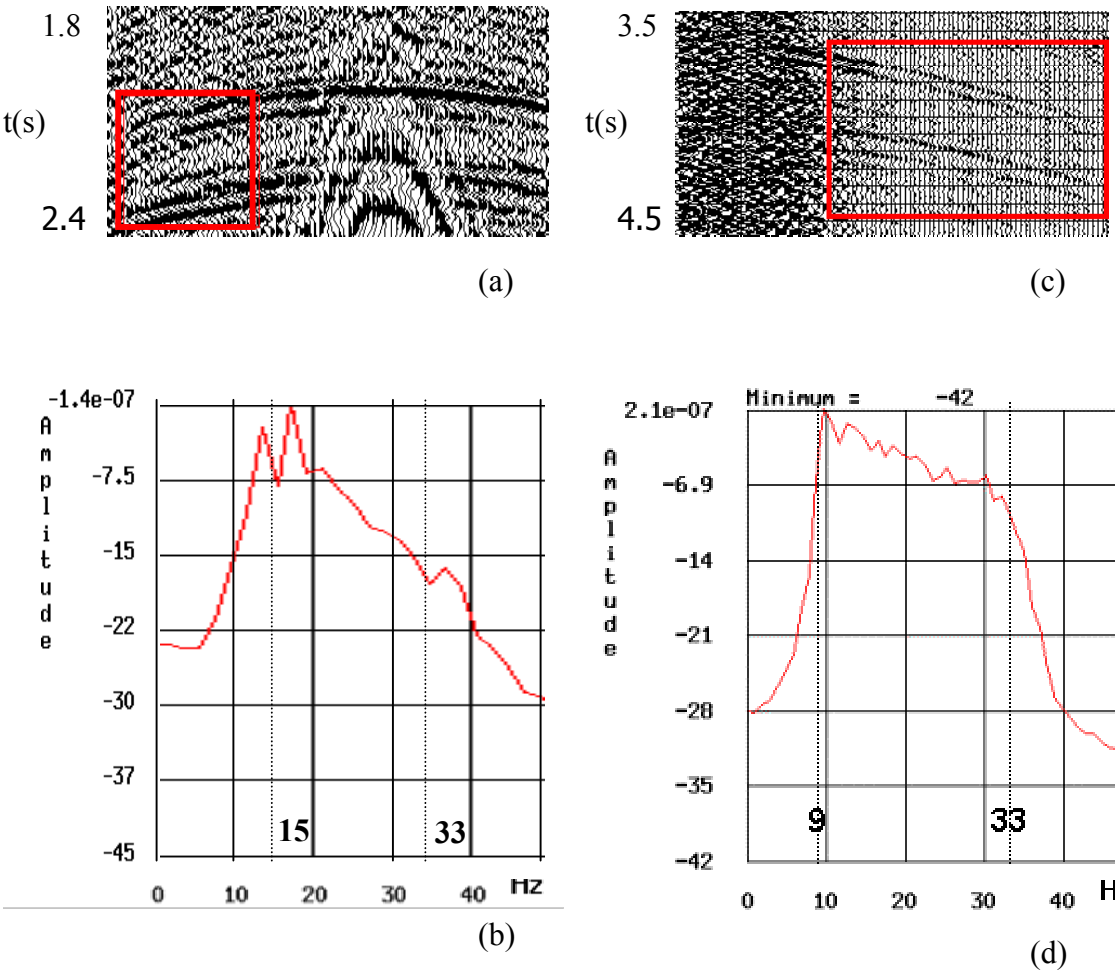

FIG. 6.4 Windows extracted from the same shot gather of PP and PS events. (a) Window of PP data extracted from the vertical component. (b) Window of PS data extracted from the radial component. (c) Average frequency spectrum of window a. (d) Average frequency spectrum of window b.

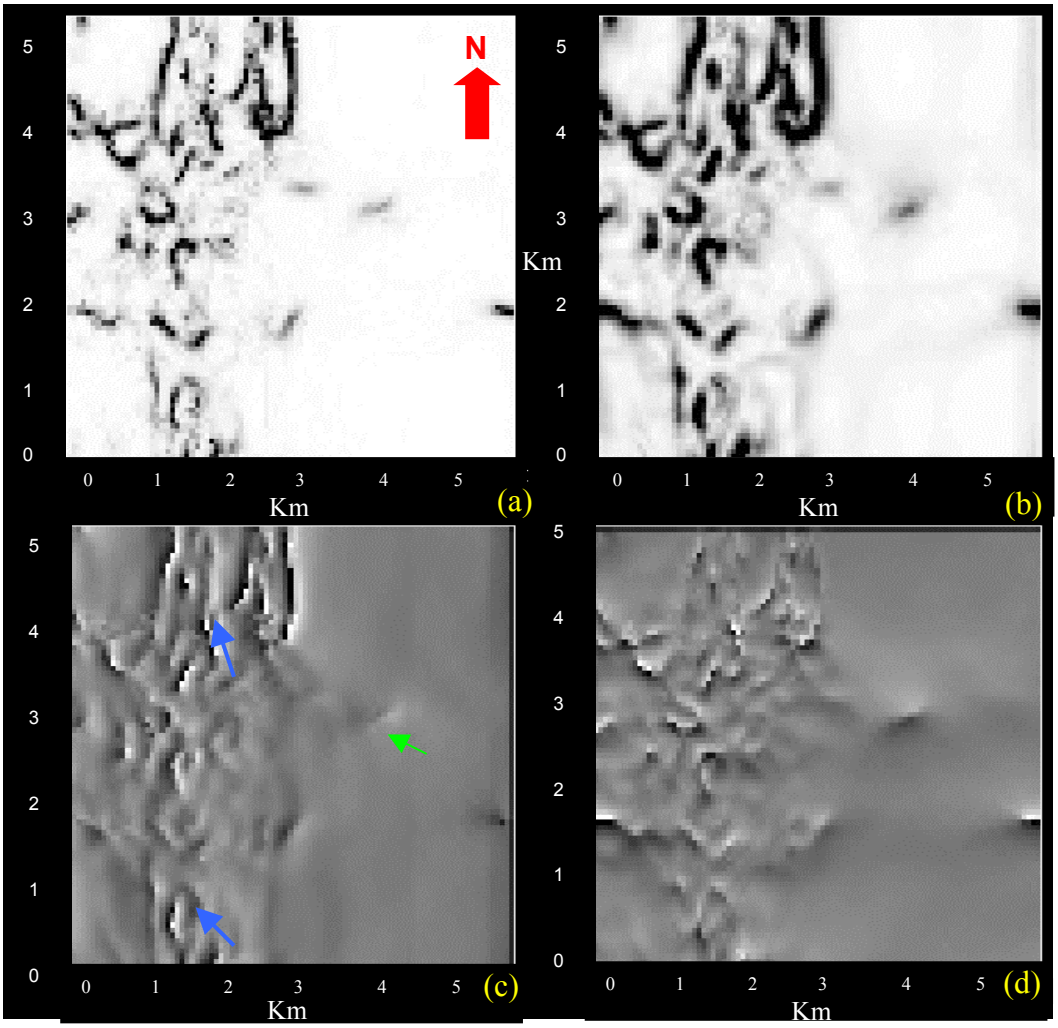

FIG. 6.5 . Horizon slices of different attributes along the Escandalosa calculated from the azimuth and offset limited PS (radial component) data volume: (a) Principle Component Coherence. (b) Semblance Coherence (c) East gradient of the principle component eigenvector. (d) North gradient of principle component eigenvector. Blue arrows indicate the reverse fault shown in Figure 4.12. and the green arrows indicate the NESW events. Azimuths range between +/-15 degrees. Both positive and negative offsets greater than 2000 m used.

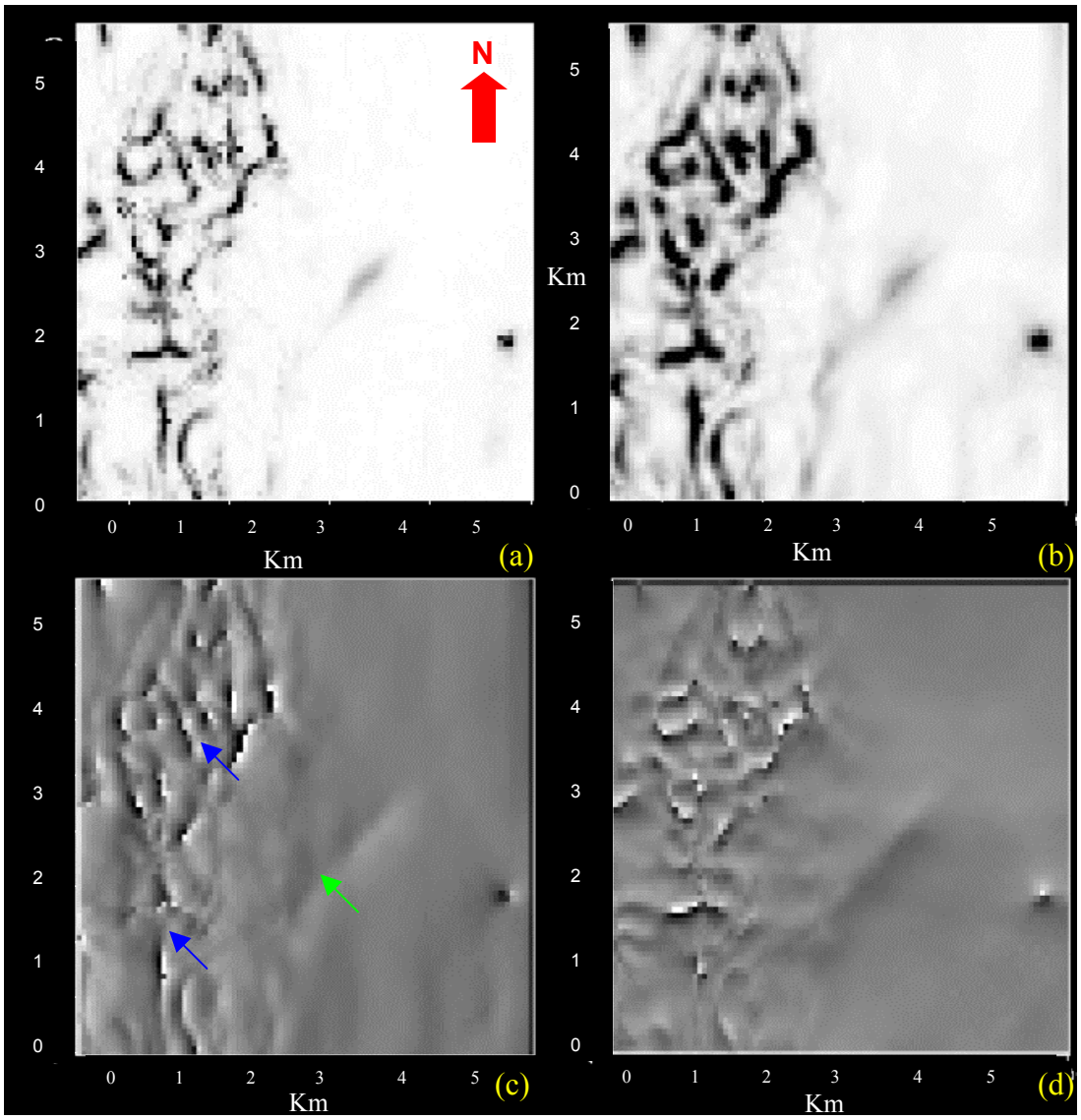

FIG. 6.6 . Horizon slices of different attributes along the Escandalosa calculated from the azimuth and offset limited PS (radial component) data volume: (a) Principle Component Coherence. (b) Semblance Coherence (c) East gradient of the principle component eigenvector. (d) North gradient of principle component eigenvector.. Blue arrows indicate the reverse fault shown in Figure 4.12. . and the green arrows indicate the NESW events. Azimuths range between +/-15 degrees. Only positive offsets greater than 2000 m used.

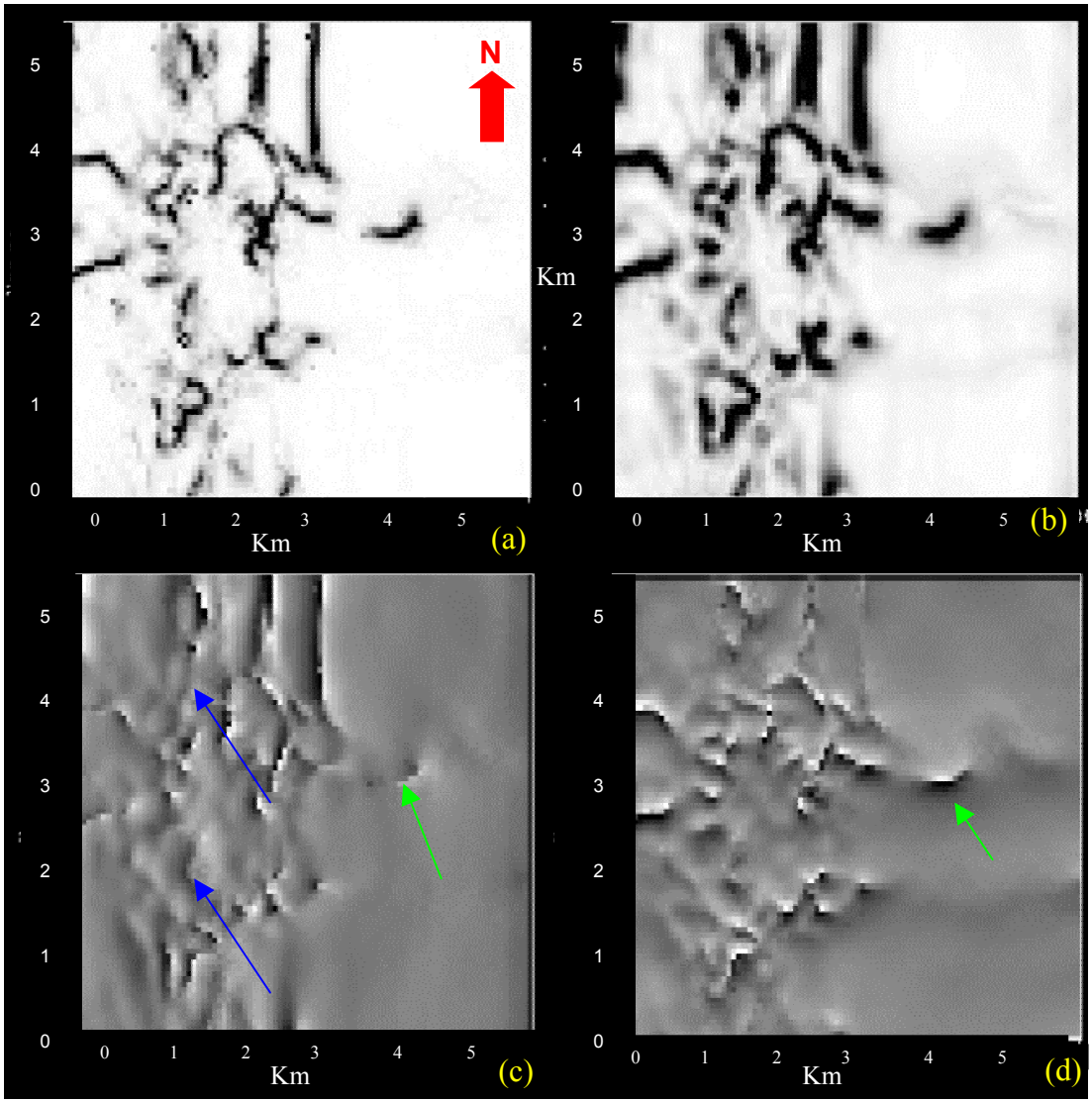

FIG. 6.7 Horizon slices of different attributes along the Escandalosa calculated from the azimuth and offset limited PS (radial component) data volume: (a) Principle Component Coherence. (b) Semblance Coherence (c) East gradient of the principle component eigenvector. (d) North gradient of principle component eigenvector. Red arrows indicate acquistion footprints. Blue arrows indicate the reverse fault shown in Figure 4.12. and the green arrows indicate the NESW events. Azimuths range between +/-15 degrees. Only negative offsets less than -2000 m used.

Chapter 7: Birefringence

It is well know that part of a P-wave's energy will be converted to shear wave energy upon incidence at a reflecting interface. If the medium above the reflector is azimuthally anisotropic, the converted shear wave will, in general, split into a fast and slow shear waves traveling back from the conversion point to the surface. We assume since the incident P-wave is longitudinally polarized, that the converted shear wave generated at a horizontal interface is radially polarized. As this radially polarized shear wave travels towards the surface, it splits at each interface into fast and slow components. By applying rotation to separate the fast and slow shear waves. We then use the rotation angle and time lag to delineate fractures.

7.1 Introduction

There are several methods used to perform birefringence analysis. Alford's (1986) rotation algorithm was designed for four component, multisource multireceiver data. (Thomsen, 1988) has shown that for data acquired with a single source polarization, such as in a converted wave wide azimuth 3-D surveys, Alford's rotation method requires modification. In conventional converted wave processing, it is common to have a wide variety of offsets and azimuths in any CCP bin. It is also common to project the horizontal components from each shot into its source receiver azimuth and to handle the resulting calculated radial data as scalar data by forming common azimuth converted point binned gathers of such traces. From this collection of traces with many offsets and azimuths, one can use least squares (or some other statistical procedure) to produce the azimuth of orientation of the principal coordinate system onto which this redundant data can best be projected (Thomsen, 1999). Alternative approaches are given by Garotta and Granger (1988) and Gaiser (1997).

Much work has been done using Hodogram analysis methods to study shear wave splitting (for example, Schulte and Edelmann, 1988). As discussed by Winterstein (1989), these methods require both very high signal to noise ratio and the presence of a single wavelet within the analysis window in order to be effective.

Alternative two component birefringence analysis schemes that do not involve hodograms have been based upon either the autocorrelation or crosscorrelation of rotated components (Narville, 1986; Peron, 1990). Harrison (1992) presented an algorithm using the autocorrelation and crosscorrelation of rotated radial and transverse components, which is particularly suitable for converted waves and is robust in the presence of noise.

Kangan (1998) developed a very simple but robust algorithm for birefringence analysis, called "parameter scanning Kangan's (1998) algorithm is more robust than Harrison's (1992) method, which fails in the presence of coherent noise. Additionally Kangan's (1998) method provides a rotation angle, which can be used to determine the fracture orientation and the time delay between fast and slow shear waves, thereby allowing me to map fracture density.

7.2 Kangan's parameter scanning method

Kangan (1998) views a single source multi receiver (or P-SV) acquisition can be viewed as a special case of multi source multi receiver acquisition. The radially polarized shear wave $S_r(t)$ produced by the conversion of a P-wave in a reflector will split into fast and slow shear waves, $S_1(t)$ and $S_2(t)$ polarized parallel and perpendicular to the fractures respectively, (Figure 2.3):

$$S_1(t) = S_r(t)\cos\theta, \qquad S_2(t) = -S_r(t-\Delta)\sin\theta, \tag{7.1}$$

where θ is the rotation angle and Δ is the time lag.

The wave field recorded by the radial and transverse receivers is given by:

$$V(t) = \begin{pmatrix} v_1(t) \\ v_2(t) \end{pmatrix} = \begin{pmatrix} \cos\theta & -\sin\theta \\ \sin\theta & \cos\theta \end{pmatrix} \begin{pmatrix} S_1(t) \\ S_2(t) \end{pmatrix}. \tag{7.2}$$

Therefore, substituting equations 7.1 into 7.2, we obtain:

$$v_1(t) = S_r(t)\cos^2\theta + S_r(t-\Delta)\sin^2\theta\,, \tag{7.3}$$

$$v_2(t) = S_r(t)\sin\theta\cos\theta - S_r(t-\Delta)\sin\theta\cos\theta\,. \tag{7.4}$$

Next transforming equations 7.3 and 7.4 into the frequency domain, we obtain:

$$v_1(\omega)/S_r(\omega) = \cos^2\theta + \sin^2\theta e^{-i\omega\Delta}\,, \tag{7.5}$$

$$v_2(\omega)/S_r(\omega) = \sin\theta\cos\theta - \sin\theta\cos\theta e^{-i\omega\Delta}\,. \tag{7.6}$$

From equation 7.6, the following identity can be deduced:

$$v_1(\omega)\left(1-e^{-i\omega\Delta}\right)\sin 2\theta = 2v_2(\omega)(\cos^2\theta + \sin^2\theta e^{-i\omega\Delta})\,, \tag{7.7}$$

this expression can be re-written in the time domain as:

$$E(\theta,\Delta,t) = [v_1(t)\sin 2\theta - 2v_2(t)\cos^2\theta] - [v_1(t-\Delta)\sin 2\theta + 2v_2(t-\Delta)\sin^2\theta] = 0\,. \tag{7.8}$$

Using equation 7.8 for a range of rotation angles, θ, and time lags, Δ, we compute the error norm:

$$\left\|E(\theta,\Delta,t)\right\|_p = \left(\sum_{k=0}^{N-1}\left|E(\theta,\Delta,t+k\Delta t)\right|^p\right)^{\frac{1}{p}}. \tag{7.9}$$

7.3 Harrison's method:

Harrison's (1992) rotation algorithm for single source multireceiver shear wave data is based on the forward modeling of crosscorelation between rotated radial and transverse components. If the autocorrelation of noise is zero or the S/N ratio is very high, Harrison (1992) found that the sum of the auto correlations of the rotated components should be equal or proportional to the auto correlation of the shear wave source wavelet.

Harrison (1992) shows that the crosscorrelation of the rotated components can be forwarded modeled by analytical equations computed directly from the rotated data. Therefore, the so-called normalized prediction error energy for total crosscorrelation, can be computed by integrating over the full range of trial rotation angle (-90º to 90º) for each pair of true rotation angles, θ, and time lag, Δ. Unfortunately, Harrison's (1992) assumption that the sum of the autocorrelation of the rotated components should be equal

or proportional to the auto correlation of the shear-wave source wavelet breaks down in the presence of coherent noise.

7.4 Synthetic data example

In Figure 7.1a-c, we display a simple wavelet, and then radial and transverse synthetic data generated for converted PS wave traveling through an anisotropic layer. The anisotropy axis is 30°, and gives rise to a time delay is of 40 ms between the fast and slow components.

In Figure 7.2 we show the result of Kangan's parameter scanning for anisotropy direction and time lag. We note a very localized, global minimum at 30° and 40 ms. Rotation using this azimuth and Kangan's (1998) algorithm produces the fully separated fast and slow waves shown in Figures 7.1d and e.

In Figure 7.3 we generate a similar synthetic but now with coherent noise whose amplitude is 0.5 times that of the signal Figure 7.4 shows the parameter scanning result is quite stable even in the presence of noise. Using this angle, the fast and slow waves are fully separated and displayed in Figure 7.3d and 7.3e.

7.5 Real data example

We sorted the Borburata Field data into six azimuth directions 30 degrees apart (Figure 7.5), and applied the final processing, stack and migration flow discussed in Chapter 5. The goal of such azimuthal sorting is to evaluate changes in waveform character (if any) that may be associated with anisotropy. In this way, it will be easier to identify the fast and slow polarization azimuth, important for the birefringence analysis. In addition to restricting the data by azimuth, we restrict it by offset. Clearly, converted PS waves will have very poor signal to noise at near offsets. Furthermore, the inside ground roll mute applied in Chapter 5 removed what little signal was left. For these reasons, we restricted our analysis to offsets greater than 2000 m.

Because of the asymmetry in the ray path between downgoing P and upgoing S waves at a given CCP point, the same image point may be mapped to slightly different times (Figure 7.6); we therefore separated the remaining data into negative offsets. Even though we do not measure significant lateral velocity variation, this asymmetry is a first order effect.

In Figure 7.7, we display line 60 for the six different azimuths containing both positive and negative offsets. The colored numbers in Figure 7.7 correspond to the azimuths sketched in Figure 7.5. We observe that azimuth 4, in the NS direction, better images the fault than azimuth 1, in the EW direction. We interpret this difference to be due to errors in both acquisition and moveout correction. The NS azimuth is parallel to the fault, such that this part of the acquisition is along a strike and such that we are able to image the upper and lower blocks on either side of the fault. In contrast, the EW azimuth is a dip line. Not only do rays coming from the lower block of the fault emerge beyond the end of the survey, but the assumptions of flat reflector converted wave velocity analysis and moveout are violated. Even though the structure is fairly simple, the diffracted energy from the thrust fault that does not allow us to identify a fast and slow direction in this azimuth gathers. We also note an interesting change in polarity and a bright spot on the radial component at azimuth 2. Given our lack of well control, a quantitative analysis of this amplitude vs azimuth feature is beyond the scope of this work, but could form the basis for a future study.

In Figure 7.8 we compare the radial and transverse component of line 60 of the migrated cube considering full far offset and NS azimuth (azimuth 4). We plot the radial component to the left and the transverse component to the right of CDP 70 (indicated by the red arrow) we observe that there is a shift and change of wavelet shape between both components from the top of the section down to the Escandalosa target at 3000 ms. Closer inspection of Figure 7.7 reveals a consistent waveform for azimuth 6 until we reach 4000 ms, where we note a small time shift associated with the fractured reservoir (Figure 7.9). With this result, we therefore conclude that there is shallow anisotropy at Borburata field, which seems to be in the direction of

azimuth 6. This shallow anisotropy can be due to azimuthally dependent statics or the distribution of conglomerates in the near surface which have been reported in the area. There is a different anisotropic effect due to the fractured reservoir around 4000 ms where the wavelets start to distort a bit. Therefore, at the reservoir level, we must first attempt to remove the effect of the overburden before estimating anisotropy in the fractured reservoir.

To corroborate the hypothesis above, we picked the top of the Escandalosa formation located near 3900 ms, and then we applied Kangan's (1998) rotation analysis algorithm. The results of this analysis show that there is a consistent SE-NW anisotropy axis. This direction is represented by azimuth 6, corroborating our visual observations in Figure 7.9.

On Figure 7.10, we window the radial and transverse component in the area of interest before and after the rotation analysis. We observe that when rotating the data, which originally was restricted in the NS azimuth (Figure 7.8 wich is equivalent to Figure 7.10a), using the angles obtained using equation 3.8, the strongest reflector at 3500 ms has the same wavelet shape in the radial and transverse component. Additionally there is a small time shift showing that they are the fast and slow components. The stripes seen in the rotated data (Figure 7.10b) are due to cycle skips or other errors in the algorithm Next, we built a shallow anisotropy map (Figure 7.11). The direction of the arrows indicates the direction of the shallow anisotropy while the length of the arrows is a measure of intensity. The colored map below is the time structural map of the area related to the strong event at 3900 ms, the picked event for the analysis. Hot colors are indicative of deeper areas and the cold colors are indicative of shallow. The shallow anisotropy is very uniform having a preferential direction on azimuth 6 (SE-NW), as displayed in the histogram shown in Figure 7.12. This direction is orthogonal to the Andes whose rise is the last compressive event in the area.

The stress map (Figure 7.13) displays the orientations of the maximum horizontal stress. The length of the stress symbols represents the data quality, with A

as the best quality category. A-quality data are believed to record the orientation of the horizonal tectonic stress field to within ±10°-15°, B-quality data to within ±15°-20° and C-quality data to within ±25°. D-quality data are considered to yield questionable tectonic stress orientations (Zoback, 1992). The tectonic regimes are: NF for normal faulting, SS for strike-slip faulting, TF for thrust faulting and U for an unknown regime. This map shows that the stress in the area of interest (red star) has an azimuth consistent with the observed SE-NW direction of shallow anisotropy.

To remove the shallow anisotropy effect from the data, we rotate the data sorted along azimuth 6 in order to align the radial component to the direction of main stress (Fast component). From these data, we picked the base of Escandalosa reservoir in order to measure in the rotation analysis the anisotropic effect due to the fractured reservoir. The rotation analysis was done in the same way as before when analyzing the regional stress. Figure 7.14 shows the fracture map obtained considering positive offset and the NS azimuth. In Figure 7.15, there is a histogram of the estimated angles. Therefore, the majority of the angles are around 250°, and there is a component in some areas at 200°, NS direction. These results show the main fracture direction in the area considering that there will be fractures of different age and different direction.

Figure 7.14 shows that in the area around the main NS fault, the majority of the fractures are oriented basically parallel to the fault as expected. On the other hand, due to the thrusting, the main system of fractures was expected in the EW direction as it is shown in the results. There is an anomaly in the NE corner of the map which can not be related to anything, and it is interesting to see that this anomaly can be related to the subtle feature (A) that is seen on Figure 6.1b, maybe it is a weak zone rather than a fault, maybe it is an error. There are two anomalies, A and B, (Figure 7.14) which can be attributed to changes of facies or porosity which make the zone more flexible, allowing this area to maintain the old NS fracture system previous to the rise of the Andes. Figure 7.16 shows the fracture map obtained using both positive and negative offset sorted along NS azimuth. We observe that this result is very similar to

the one obtained with just the positive offset. This is due to the fact that the rotation analysis depends on a correlation of the radial and transverse trace. Figure 7.17 shows the histogram, which says that the majority of the fractures are 240° (azimuth 2). Both maps show basically the same anomalous areas. The change in direction of fractures is related to anomalies in the area. Figure 7.18 superpose the fracture map obtained with positive offsets with the East gradient of principal component attribute map with positive offset. Notice that the anomalies A and B showed in Figure 7.14 are well correlated to features in the attribute map.

It is important to mention that the estimated fracture density and orientation maps shows the anisotropy behavior in the Escandalosa Formation, therefore they show the average or main fracture direction in the area. Image logs where not available to corroborate this result.

7.6 Conclusions

There is shallow anisotropy in Borburata Field, it is possibly related to static variations with azimuth, this study is proposed for a future work. Kangan's algorithm is robust for birefringence analysis. The map of fracture orientation is consistent with the coherence attribute maps. As a future work, it would be interesting to compare the attribute maps after their birefringence analysis to measure the impact of azimuthal anisotropy over the results.

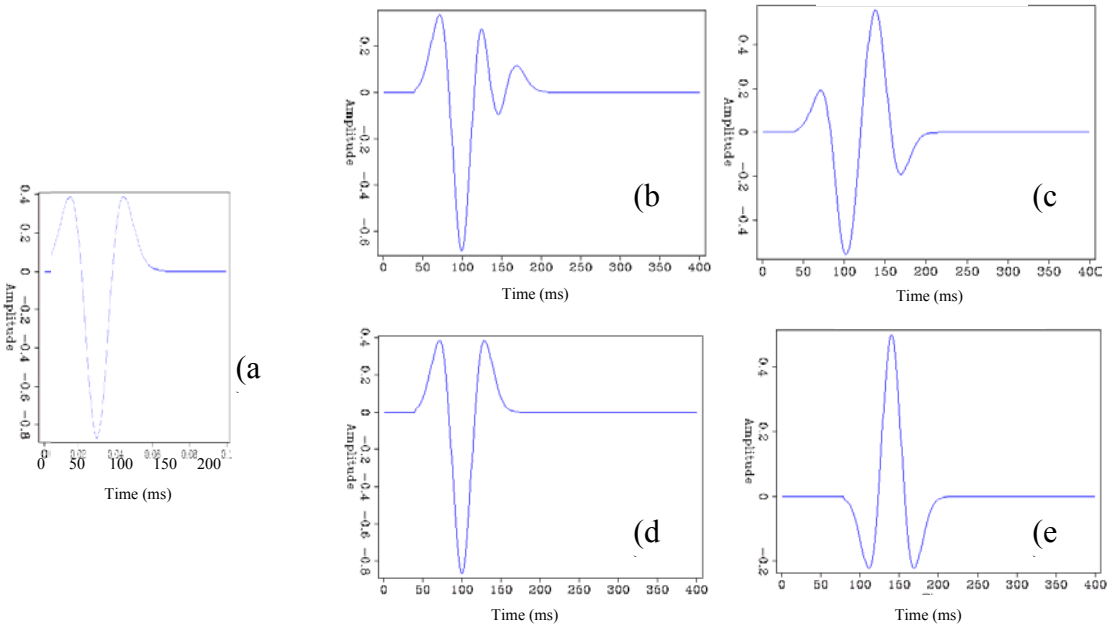

FIG. 7.1 (a) Seismic wavelet and (b) radial component, and (c) transverse component obtained for a time lag of 40 ms and axis of anisotropy of 30°. (d) Fast component, and (e) slow component.obtained after using the time delay and anisotropy angle found in Figure 7.2.

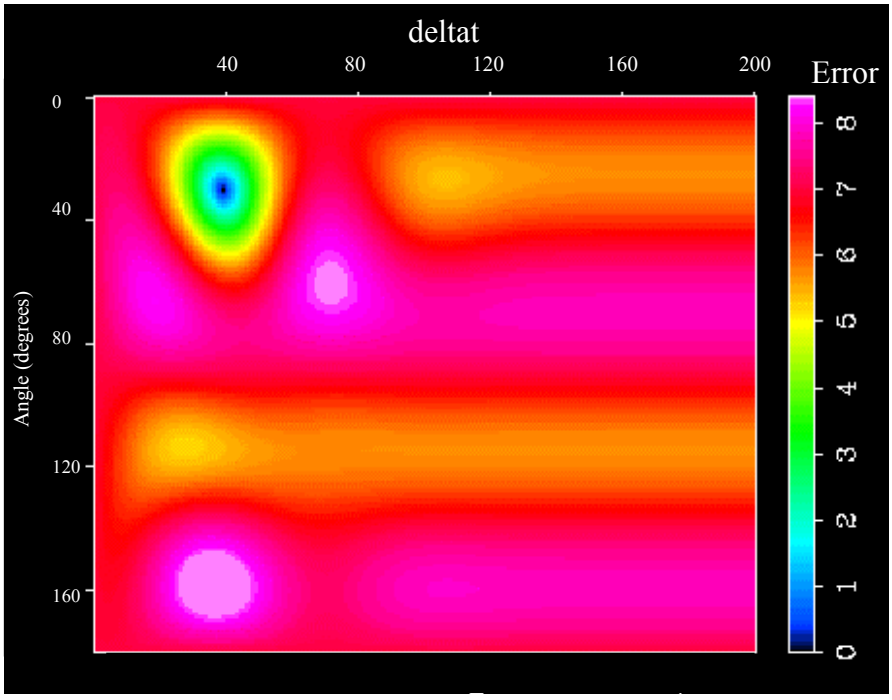

FIG. 7.2 Error function given by equation 6.8 as a function of delay time and anisotropy azimuth for the two traces shown in Figure 7.1b.

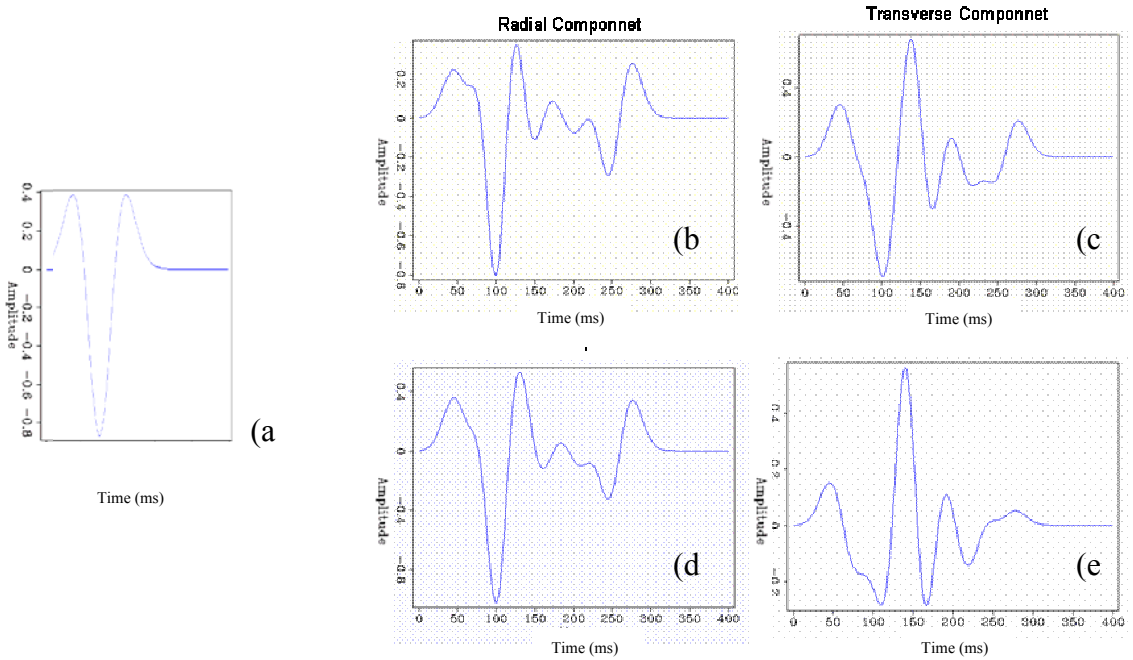

FIG. 7.3 Same model as shown in Figure 7.1, but with 50% coherent noise added to the input traces to produce contaminated (b) radial, and (c) transverse traces. Parameter analysis shown in Figure 7.4 produces estimates of (d) fast and (e) slow shear wave signals.

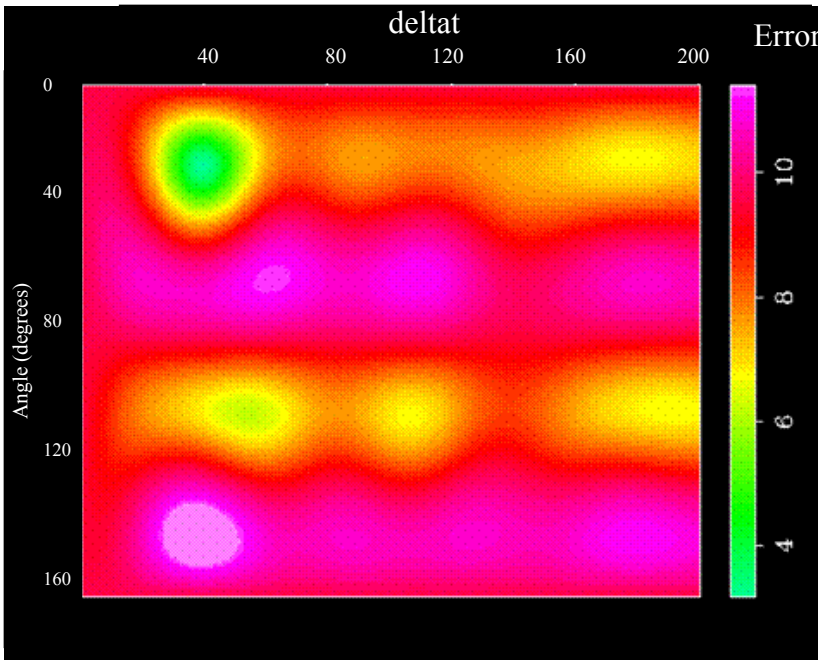

FIG. 7.4 Error function given by equation 6.8 as a function of delay time and anisotropy azimuth for the two traces shown in Figure 7.3.

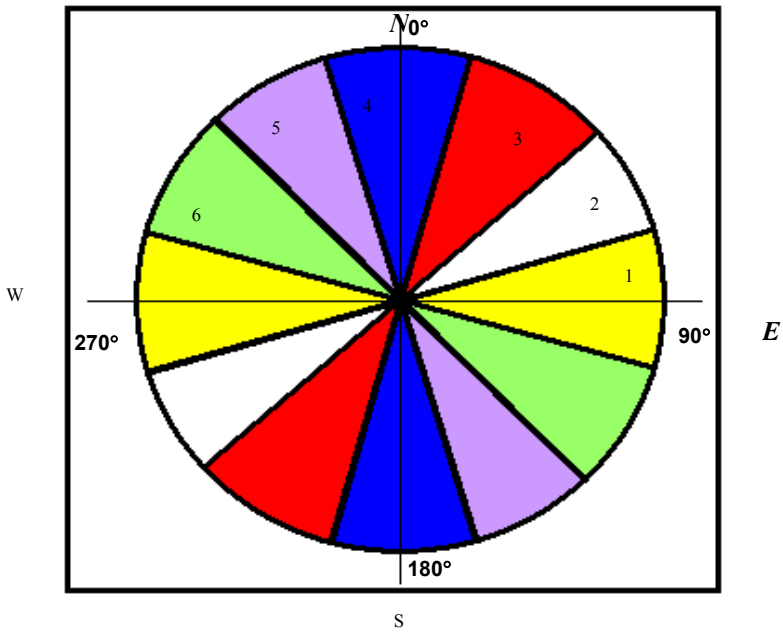

FIG. 7.5 Azimuthal bins used in the final processing, stack and migration of the Borburata 3D3C data.

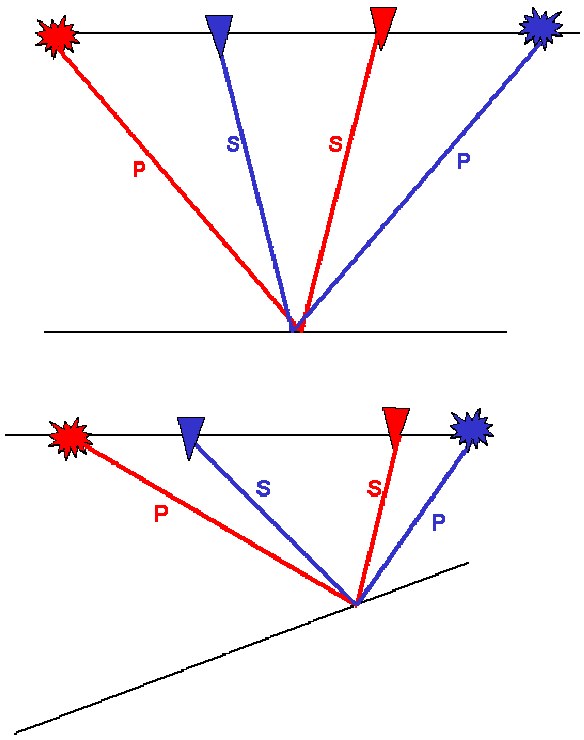

FIG. 7.6 Sketch of ray paths with positive and negative offset illuminating the same point. The recording time will be different due to the asymmetry in the travel path.

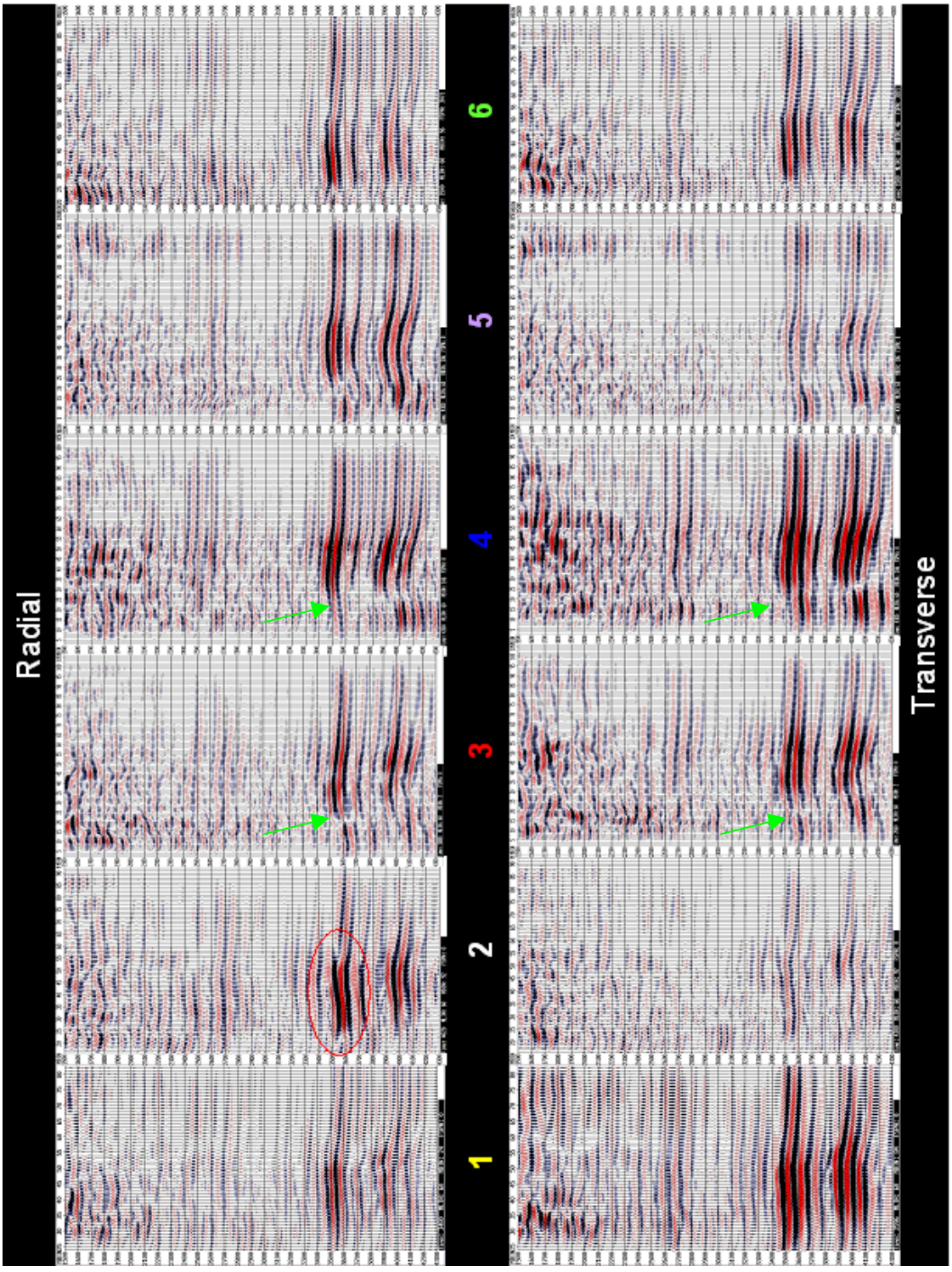

FIG. 7.7 Comparison of the radial and transverse components of azimuthally sorted and migrated data for EW crossline 60. Both positive and negative offsets greater than 2000 m were used in each image. The colored numbers indicate the common azimuth gathers shown in Figure 7.5. The NS azimuths 3 and 4 image the fault discontinuity (shown by arrows) best.

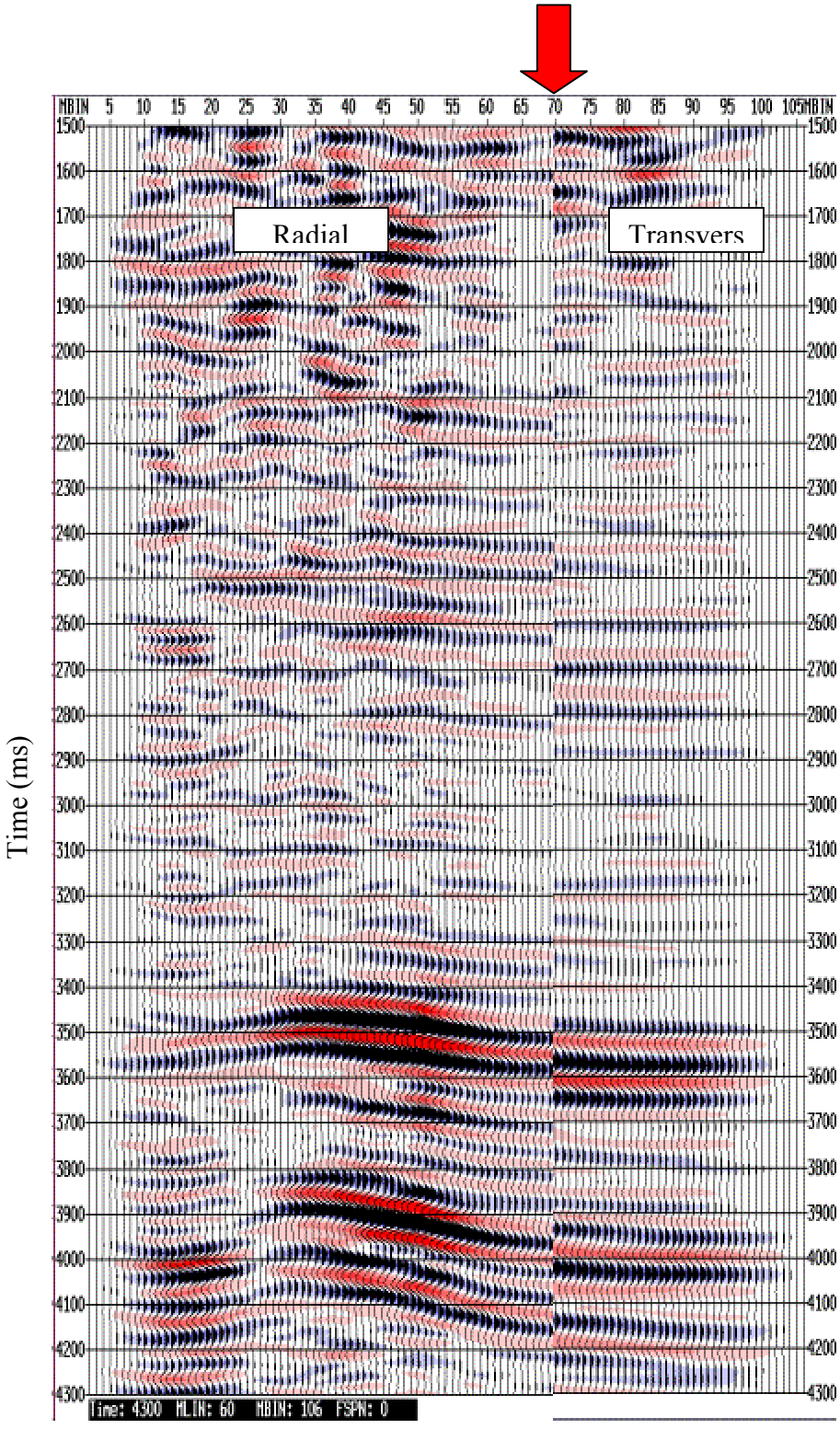

FIG. 7.8 Juxtaposition of the radial and transverse component for cross line 60 of the migrated cube for azimuth 4 (NS direction).

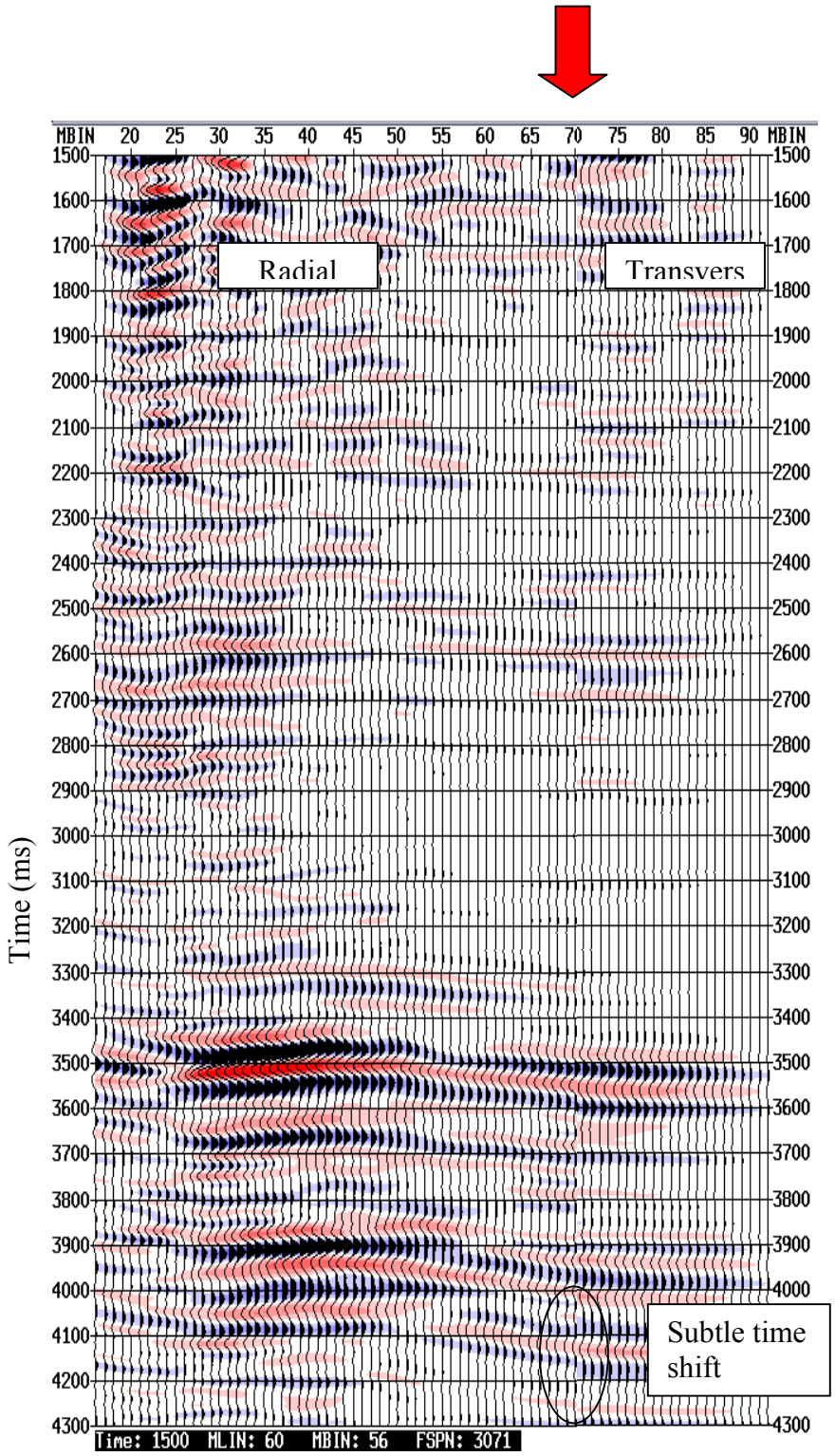

FIG. 7.9 Juxtaposition of radial and transverse components for cross line 60 of the migrated cube for azimuth 6.

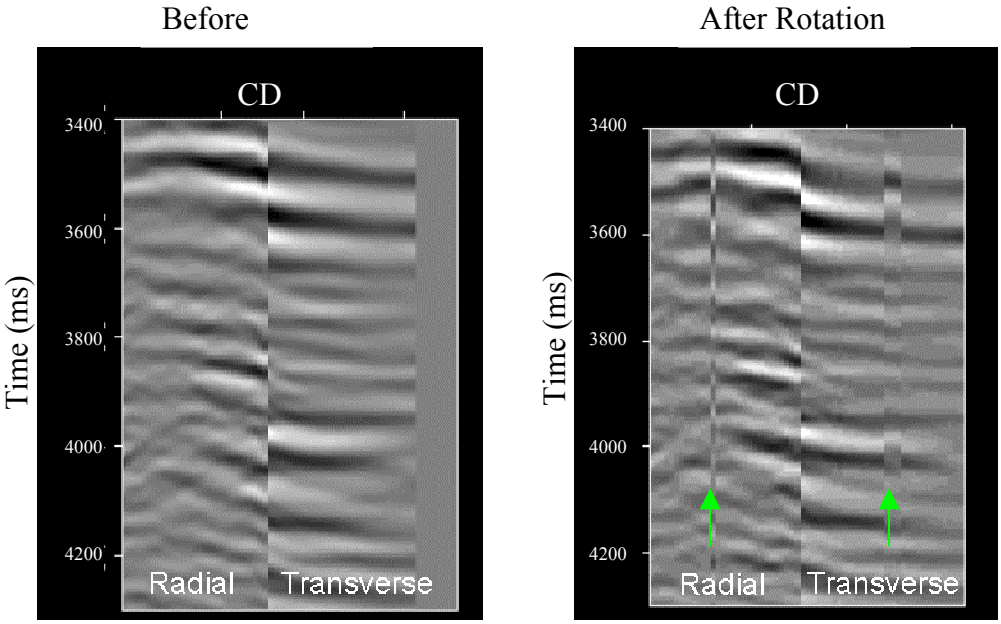

FIG. 7.10 Comparison of the rotation analysis over cross line 60 considering a common azimuth gather in the NS direction. (a) Before rotation analysis, (b) after rotation analysis. Note errors in rotation angle estimation on traces indicated by arrows.

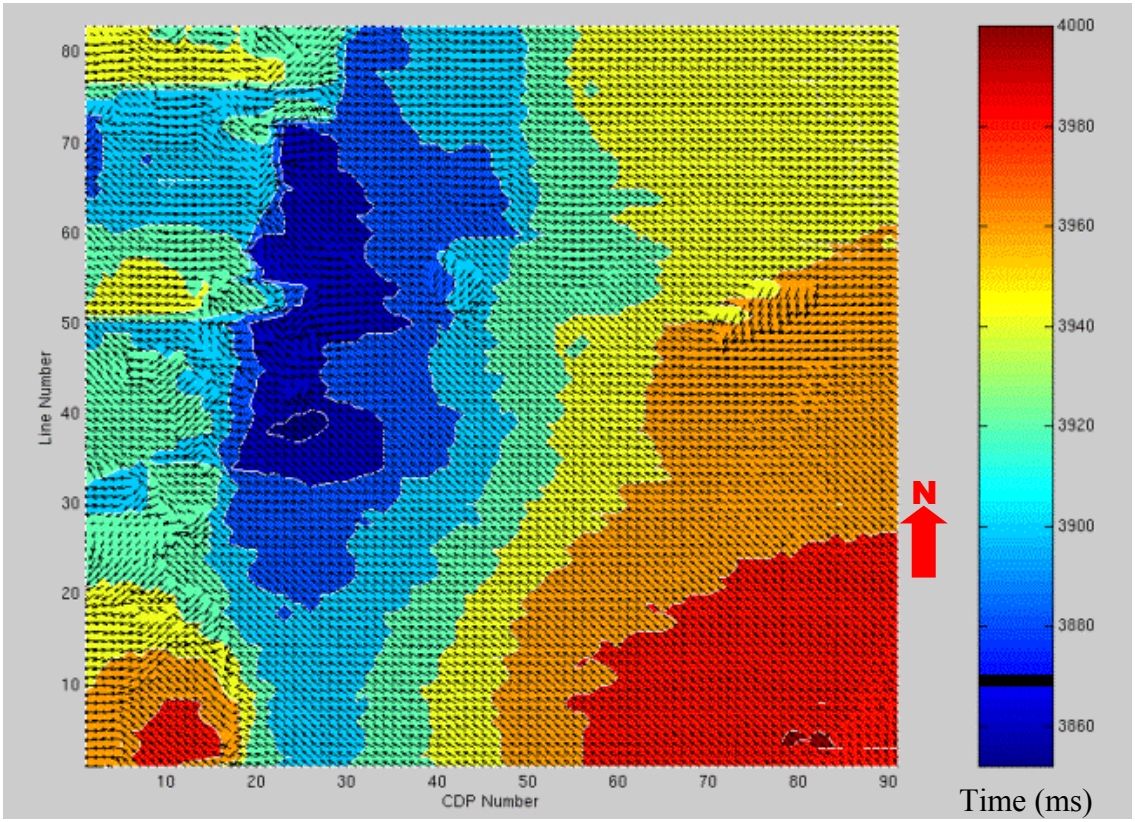

FIG. 7.11 Anisotropy measured above and diplayed on top of the Escandalosa time structure map. The azimuth and length of the arrows corresponds to the anisotropy azimuth and time delay.. Time delay is considered to be proportional to fracture density and layer thickness.

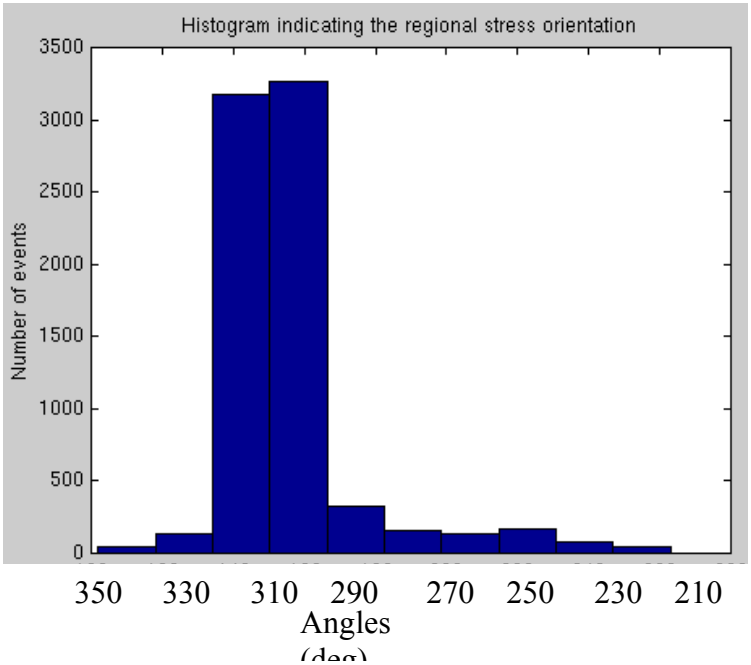

FIG. 7.12 Histogram of anisotropy azimuth shown in Figure 7.11, which is indicative of the direction of regional stress.

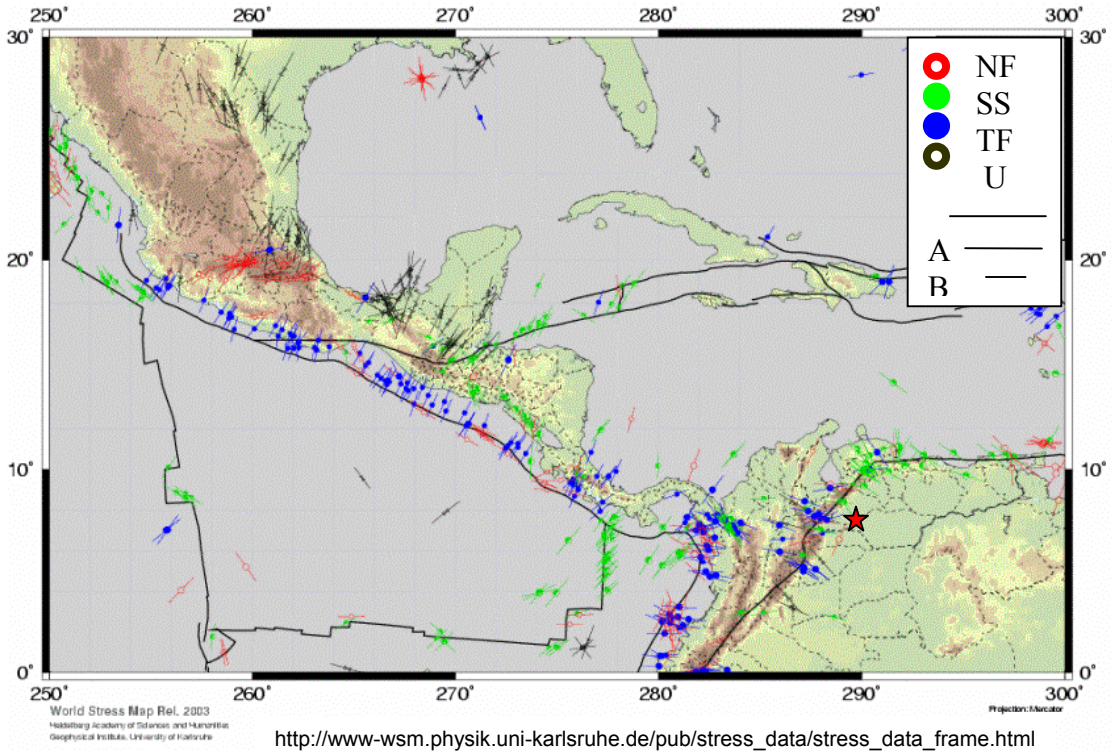

FIG. 7.13 of maximum horizontal stress SH. The length of the stress symbols represents the data quality, with A (the largest stress symbol) as the best quality category. A-quality data are believed to record the orientation of the horizonal tectonic stress field to within ±10°-15°, B-quality (medium stress symbol) data to within ±15°-20° and C-quality (smaller stress symbol) data to within ±25°. D-quality data are considered to yield questionable tectonic stress orientations (Zoback, 1992). The tectonic regimes are: NF for normal faulting, SS for strike-slip faulting, TF for thrust faulting and U for an unknown regime.

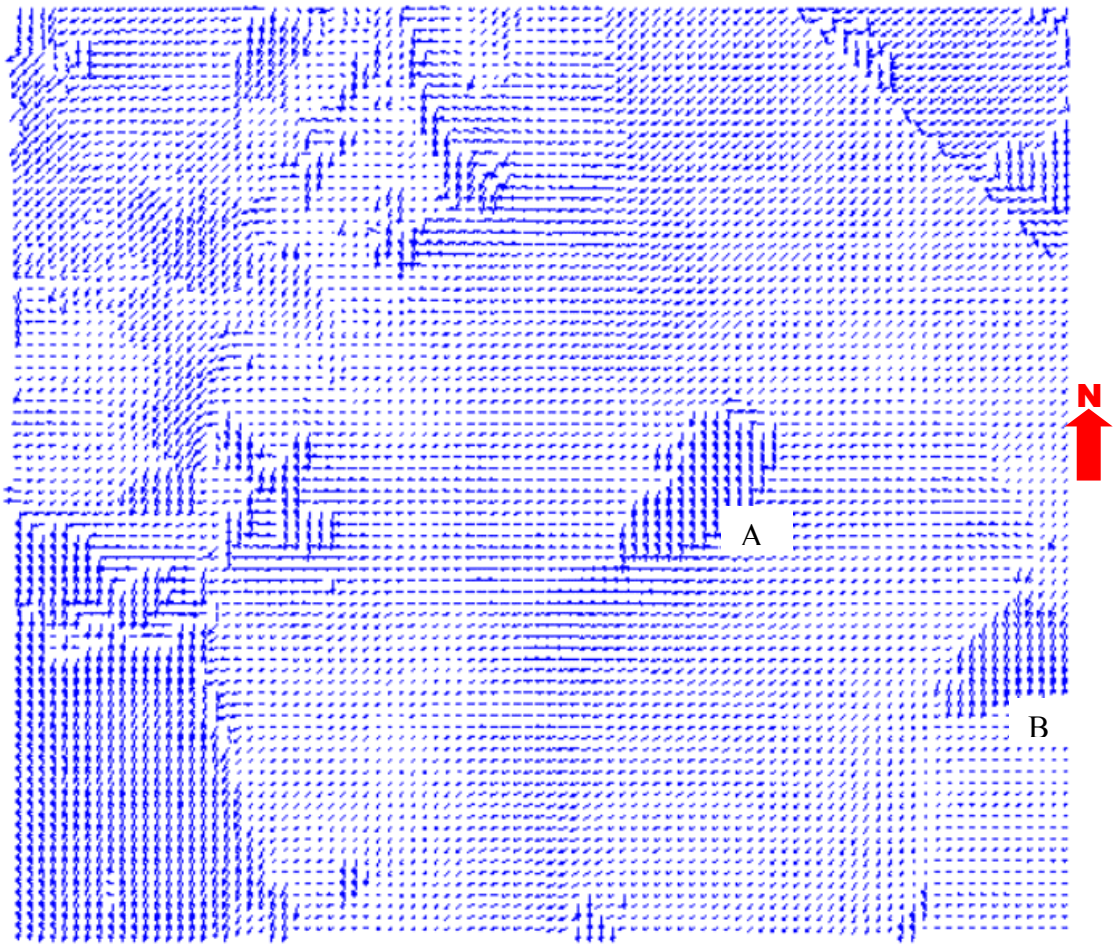

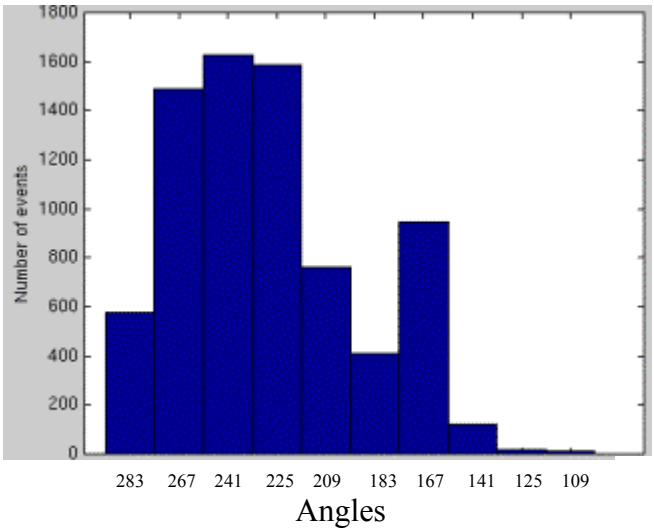

FIG. 7.15. Histogram of the obtain angles indicating the direction of fractures at Escandalosa formation.

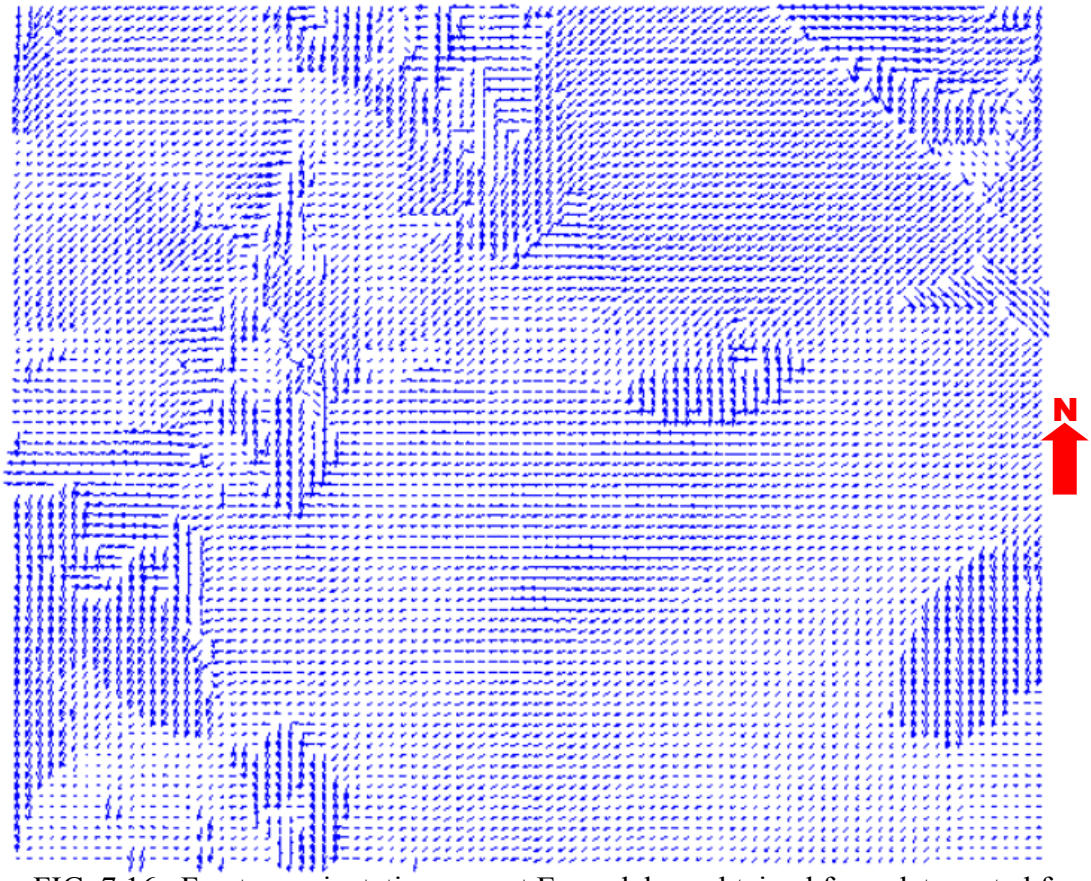

FIG. 7.16. Fracture orientation map at Escandalosa obtained from data sorted for positive and negative far offset and NS azimuth. We interpret the direction of the arrows to indicate the direction of the regional stress, while the length of the arrows is a measure of the intensity of stress.

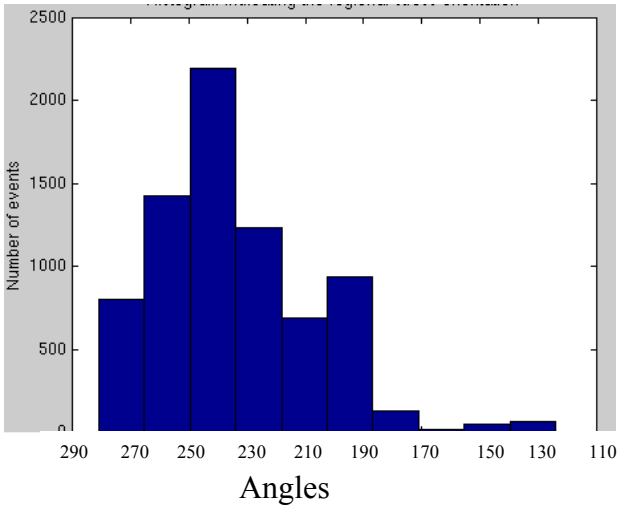

FIG. 7.17. Histogram of the obtain angles indicating the direction of fractures at Escandalosa formation.

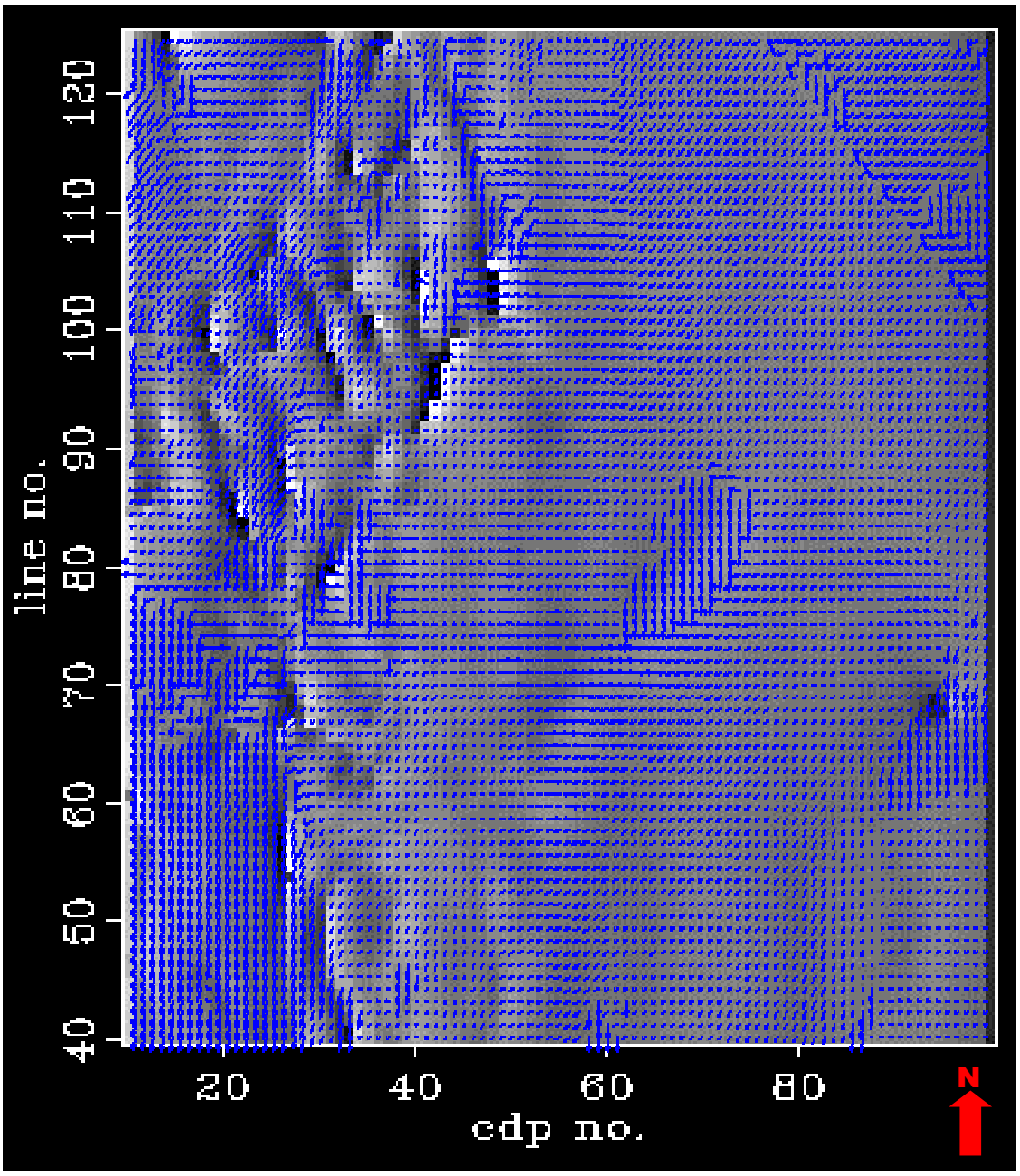

FIG. 7.18. Fracture orientation map at the base of the Escandalosa obtained from positive far offset and NS azimuth sorted data. We interpret the direction of the arrows indicate the direction of the regional stress, and the length is a measure of the intensity of stress. The background is the corresponding east gradient of principal component attribute map obtained from the same data subset.

Appendix 1: Migration velocity derivation

In this appendix, we review Harrison's (1992) work on velocity estimation to be used in post stack migration of PS-waves.

Consider a conversion from the point diffractor shown in Figure A1, which is at a distance x from a coincident source and receiver on the surface. Energy travels from the source to the diffractor point along n segments a_i with P-wave velocity, α_i, and back from the diffraction point along n different path segments, b_i, according to Snell's law, with S-wave velocity, β_i. The total travel time, t, is given by

$$t = \sum_{i=1}^{n} \frac{a_i}{\alpha_i} + \sum_{i=1}^{n} \frac{b_i}{\beta_i}. \tag{A1}$$

For this horizontally layered geometry path, the downward path, ray parameter is a constant p_1 while the upward ray parameters are a different constant p_2;

$$p_1 = \frac{\sin\theta_i}{\alpha_i} \quad \text{and} \quad p_2 = \frac{\sin\varphi_i}{\beta_i} \quad \text{for all } i. \tag{A2}$$

The total horizontal distance traveled along both up-going and down-going paths is equal to the offset x. In terms of the two ray parameters, equation (A1) can be rewritten as

$$t = \sum_{i=1}^{n} \frac{z_i}{\alpha_i \sqrt{1 - p_1^2 \alpha_i^2}} + \sum_{i=1}^{n} \frac{z_i}{\beta_i \sqrt{1 - p_2^2 \beta_i^2}}. \tag{A3}$$

To obtain an approximate solution for t, a Taylor's series expansion can be performed about $x=0$ (the small diffractor offset case):

$$t \cong t_o + x\left(\frac{dt}{dx}\right)_{x=0} + \frac{x^2}{2}\left(\frac{d^2t}{dx^2}\right)_{x=0} + \frac{x^3}{6}\left(\frac{d^3t}{dx^3}\right)_{x=0} + O(x^4), \tag{A4}$$

where O(x^4) represents terms of order x^4 and higher, and t_o is the two way vertical travel time:

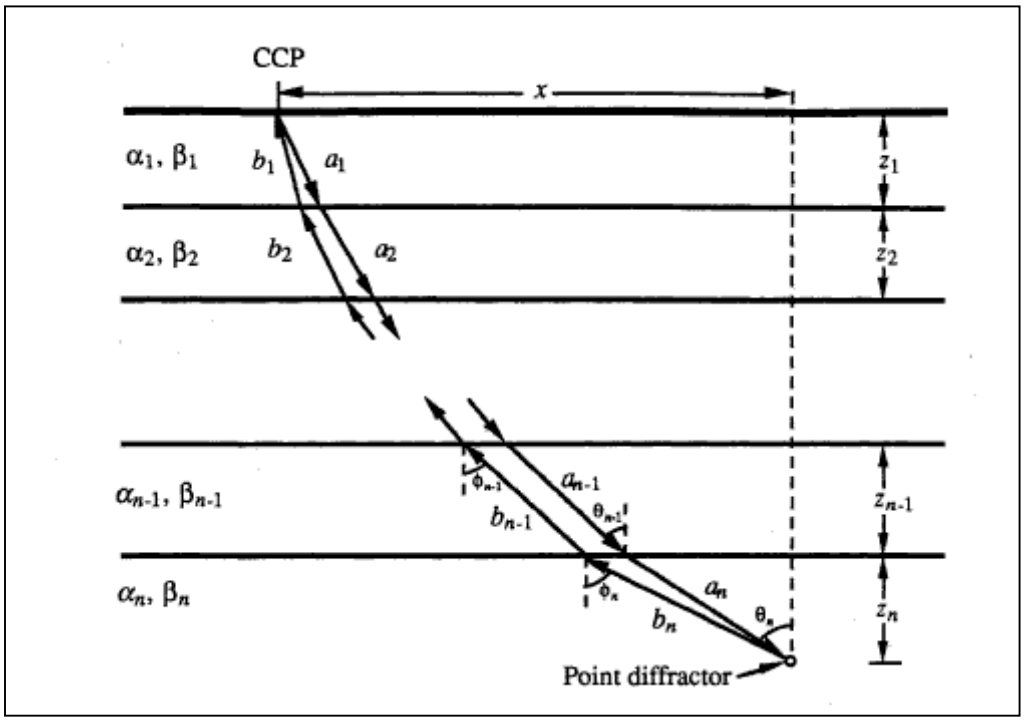

$$t_o = \sum_{i=1}^{n}\left(\frac{\alpha_i + \beta_i}{\alpha_i \beta_i}\right) z_i = \sum_{i=1}^{n} \tau_i \,, \tag{A5}$$

where τ_i is defined to be the two way travel time through the ith layer. The odd order terms in equation A4 must vanish because of cylindrical symmetry. Taking the derivatives of t from equation (A3) with respect to x and substituting them into equation (A4) we obtain:

$$t \cong t_o + \frac{x^2}{2}\left[\frac{\sum_{i=1}^{n} \alpha_i \beta_i \tau_i}{\left(\sum_{i=1}^{n} \frac{\alpha_i^2 \beta_i}{\alpha_i + \beta_i}\tau_i\right)\left(\sum_{i=1}^{n} \frac{\alpha_i \beta_i^2}{\alpha_i + \beta_i}\tau_i\right)}\right] + O(x^4). \tag{A6}$$

Squaring both sides of equation (A6) gives

$$t^2 = t_o^2 + \frac{4x^2}{V_{mig}^2}, \tag{A7}$$

where V_{mig} is the migration velocity, given by:

$$V_{mig} = 2\sqrt{\frac{\left(\sum_{i=1}^{n} \frac{\alpha_i^2 \beta_i}{\alpha_i + \beta_i} \tau_i\right)\left(\sum_{i=1}^{n} \frac{\alpha_i \beta_i^2}{\alpha_i + \beta_i} \tau_i\right)}{t_o \sum_{i=1}^{n} \alpha_i \beta_i \tau_i}}. \tag{A8}$$

For the single layer case, where n=1, equation (A8) reduces to

$$\frac{1}{V_{mig}} = \frac{1}{2}\left(\frac{1}{\alpha} + \frac{1}{\beta}\right). \tag{A9}$$

Equation (A9) is the same result given by Eaton *et al*. (1991).

References

Abdu-Jauwad, S. and Khene, F., 2000, Two-dimensional wavelet-based ground roll filtering, 70th Ann. Internat. Mtg: Soc. of Expl. Geophys., 2107-2110.

Alfaraj, M. N., 1993, Transformation to zero–offset for mode converted waves, Ph.D. Thesis, Colorado School of Mines.

Alford, R. M., 1986, Shear data in the presence of azimuthal anisotropy: Dilley, Texas: 56th Internat. Mtg., Soc. Expl. Geophys., Expanded Abstracts, Session:s9.6.

Al-Husseini M., Glover J. and Barley B., 1981, Dispersion patterns of the Ground Roll in eastern Saudi Arabia, Geophysics, **46**, 121-137.

Ata, E., and Michelena, R. J., 1995, Mapping distribution of fractures in a reservoir with P-S converted waves: The Leading Edge, **14**, 664-673.

Baculin, A., Grechka, V, and Tswankin, I., 2000, Estimation of fracture parameters from reflection seismic data. Part I: HTI model due to a single fracture set: Geophysics, 65, 1788-1802.

Bahorich, M. and Farmer, S., 1995, 3-D seismic discontinuity for faults and stratigraphic features: The coherence cube. The Leading Edge, 1053-1058.

Brown, A., 2001, Interpretation of three dimensional seismic data, 6th edition. AAPG.

Chenin, B. and B. Joyce, 1998. Formation azimuthal anisotropy, The Leading Edge, **18**, 216-221

Eaton, D. W.S., Stewart, R.R. and Harrison, M.P., 1991, The Fresnell zone for converted P-SV waves: Geophysics **56,** 360-364.

Engelder, T., 1987, Joints and shear fractures in rock: in Atkinson, B.K., editor, Fracture Mechanics of Rock, London, Academic Press, p. 27 - 69.

Gaiser, J., 1997, 3D converted shear wave rotation with layer striping : US Patent. 5 610 875.

Gaiser, J., Loinger, E., Lynn H. and Vetri, L., 2002, Birefringence analysis at Emilio Field for fracture characterization: First Break, **20**, 505-514.

Garotta, R., and Granger, P.Y., 1988, Acquisition and processing of 3C x 3D data using converted waves: 58th Ann. Internat. Mtg., Soc. Expl. Geophys., Expanded Abstract, 657-658.

Gersztenkorn, A. and Marfurt, K. J., 1999, Eigenstructure-based coherence computations as an aid to 3-D structural and stratigraphic mapping: Geophysics, **64,** 1468-1479.

Granli, J. R., Sollid, A., Hilde, E., and Arnsten, B., 1995, Imaging through gas-filled sediments with marine S-wave data: 65th Ann. Internat. Mtg., Soc. Expl. Geophys., 352-355.

Harrison, M.P., 1992, Processing of P-SV Surface-Seismic Data: Anisotropy Analysis, Dip Moveout, and Migration, PhD Thesis, University of Calgary.

Herrenschmidt, A., Granger, P., Audebert, F., Gerea, C.,Etienne, G., Stopin A., Alerini, M., Lebegat, S., Lambare, G., Bertht, P., Nebieridze, and Boelle, J., 2001, Comparison of different strategies for velocity model building and imaging of PP and PS data. The leading edge, **20**, 984-995.

Hou, A., and Marfurt, K. J., 2001, Multicomponent prestack depth migration by scalar wavefield extrapolation, 71st Ann. Internat. Mtg: Soc. of Expl. Geophys. Expanded Abstracts, 1073-1076.

James, K.H., 2000, The Venezuelan hydrocarbon habitat, Part 1: Tectonics, structure, palaeogeography and source rocks. Journal of Petroleum Geology, **23**, 5-53.

James, K.H., 2000, The Venezuelan hydrocarbon habitat, Part 2: Hydrocarbon occurrences and generated-accumulated volumes. Journal of Petroleum Geology, **23**, 133-164.

Kangan, F., 1998, Pseudo-Spectral Modelling of Cracked Anisotropic Media and Rotation of Multicomponent Shear-Wave data: MsC thesis, The University of Calgary, Alberta, Canada.

Kupecz, J., Sorondo, J., Rojas, L., Petito, M., Chang, R., Calderon, P., Solorzano, E., and Hernandez, E., 2000, Quantitative characterization of a mixed carbonate-siliciclastic interval for reservoir simulation: Escandalosa Formation, "O" Member, Barinas-Apure Basin, Venezuela: 2000 AAPG Annual Meeting.

Lacazzete, A., 2001, http://www.naturalfractures.com/. (entered 02/10/03)

Lefeuvre, F., 1994, Fracture related anisotropy detection, and analysis:"and if the P-waves were enough?" 64th Ann. Internat. Mtg., Soc. Expl. Geophys., Expanded Abstract. 942-945.

Li. X.y., 1997, Viability of azimuthal variation in P-wave moveout, for fracture detection: 67th Ann. Internat. Mtg., Soc. Expl. Geophys., Expanded Abstract., 1555-1558.

Liu, X, 1999, Ground roll suppression using the Karhunen-laeve transform: Geophysics, **64**, 564-566.

Lynn, H.B., Simonj, K.M., Bates, C.R., and Van Dok, R., 1996, Naturally fractured gas reservoir's seismic characterization: 66th Ann. Internat. Mtg., Soc. Expl. Geophys., Expanded Abstract., 1360-1363.

Lorenz, J.C., Farrell, H.E., Hanks, C.L., Rizer, W.D., and Sonnenfeld, M.D., Characteristics of natural fractures in Carbonate Strata. In : Palaz I and Marfurt, K., 1997, Carbonate Seismology, Geophysical developments N6, 179-201.

Marfurt, K. J., Kirlin, R. L., Farmer, S. L. and Bahorich, M. S., 1998, 3-D seismic attributes using a semblance-based coherency algorithm: Geophysics, **63,** 1150-1165.

McMechan, G., and Sun, R., 1991, Depth filtering of first breaks and ground roll: Geophysics, **56**, 390-396.

Miller, S. L. M., Harrison, M. P., Lawton, D.C., Stewart, R. R., Szata, K. T., 1995, Coupled P-P and P-SV seismic analysis of a carbonate reservoir, Alberta, Canada: 57th Mtg Eur Assoc Expl. Geophys. Session: A015.

Narville, C., 1986, Detection of anisotropy using shear-wave splitting in VSP surveys: requirements and applications: 56th Ann. Internat. Mtg. Soc. Expl. Geophys., Expanded Abstracts, 391-394.

Neves, F., Al-Marzoug, A., Kim, J., and Nebrija, E., 2003, Fracture characterization of deep tight gas sands using azimuthal velocity and AVO seismic data in Saudi Arabia. The Leading Edge, **22**, 469-475.

Nicoletis, L., Svay-Lucas, J., and Prigenth, H., 1998, True amplitude imaging of converted waves: 68th Ann. Internat. Mtg. Soc. Expl. Gephys.

Nicoletis, L., Svay-Lucas, J., Schaff, T., Clochard, V., 2000, 3D vectorial prestack migration of converted S-waves: Memorias X Congreso Venezolano de Geofisica.

Parnaud, F., Gou, I., Pascual, J.C., Capello, M., Truskowiski, I. and Passalacqua, H., 1995, Stratigraphic Synthesis of Western Venezuela, in A. J. Tankard, R. Suarez S., and H.J. Welsink, Petroleum basins of South America: AAPG Memoir **62**, 681-698.

Peron, J. 1990, Estimation of fracture directions from zero-offset VSP by two and four component rotation: 60th Ann. Internat. Mtg. Soc. Expl. Geophys., Expanded Abstracts, 1443-1446.

Perez, M.A., Gibson, R.L. and Toksöz, M.N.,1999, Detection of fracture orientatiopn using azimuthal variation of P-wave AVO responses: Geophysics, **64**, 1253-1265.

Ronald, A.N, 2001, Geologic analysis of naturally fractured reservoirs. Gulf Profetional publishing, 2nd edition.

Sayers. C.M., and Ebrom, D. A., 1997, Seismic traveltimes analysis for azimuthally anisotropic media: Theory and experiment: Geophysics, **62**, 1570-1582.

Sena, A.G., 1991, Seismic traveltime equations for azimuthally anisotropic and isotropic media: Estimation of elastic properties: Geophysics, **56**, 2090-2101.

Shulte, L., and Edelmann, H.A.K., 1988, Azimuthal anisotropy proven to be useful approach for multiciomponent shear wave data processing: 58th Internat. Mtg., Soc. Expl. Geophys., Expanded abstracts, 1156-1158.

Talukdar, S., 1992, Hydrocarbon habitats of the Venezuelan basin. DGSI report, Houston, Texas.

Taner, M.T., 2000, Attributes revisited, Technical publication, Rock Solid Images Inc., Houston, Texas, URL: http://www.rocksolidimages.com/pdf/attrib_revisited.htm.

Thomsen, L., 1988, Reflection seismology in azimuthal anisotropic media: Geophysics, **53**, 304-313.

Thomsen, L., 1999, Converted wave reflection seismology over inhomogeneous, anisotropic media: Gephysics, **64**, 678-690.

Tsvankin, I., 2001, Seismic signatures and analysis of reflection data in anisotropic media. Handbook of geophysical exploration, **29**.

Tsvankin, I., 1997, Reflection moveout and parameter estimation for horizontal transverse isotropy: geophysics, 62, 614-629.

Twiss, R. and Moores, E.M., 2001, Structural Geology. Freeman and company.

Winterstein, D., 1989, Discussion on 'Shear-wave splitting in cross-hole surveys: Modeling', by E. Liu, S. Crampin, and D. C. Booth, (GEO-54-1-57-65) with reply by authors: Geophysics, Soc. of Expl. Geophys., **54,** 1503-1504.

Young, G. A., 1998. La tectónica de la Cuenca Barinas-Apure, Venezuela, interpretación magnética detallada. III simposio Bolivariano, Exploracion petrolera en las cuencas Subandinas, Caracas, Memoria, 962-984.

Zoback, M. L., 1992, First- and Second-order Patterns of Stress in the Litosphere: the World Stress Map Project; Journal of Geophysical Research, **97**, p. 11703-11728.